中央大学博士論文

# Development of nanoparticle detection system using the micro vibration-induced flow
## マイクロ振動誘起流れを用いた ナノ粒子検出システムの開発研究

Kanji Kaneko

金子　完治

博士（工学）

中 央 大 学 大 学 院
理 工 学 研 究 科
精密工学専攻

令和５年度
２０２４年３月

# TABLE OF CONTENTS

## LIST OF ABBREVIATIONS AND SYMBOLS

| Symbol | Description | unit |
|--------|-------------|------|
| CPs | Capture particles | - |
| NPs | Nanoparticles | - |
| EVs | Extracellular vesicles | - |
| LOD | Limit of detection | /mL |
| VIF | Vibration-induced flow | - |
| CPs | Capture microparticles | - |
| | | |
| $D$ | Diameter of micropillar | μm |
| $h$ | Height of pillar | μm |
| $S$ | Distance between the center of the pillar | μm |
| $f$ | Vibration frequency | Hz or 1/s |
| $A$ | Vibration amplitude | μm |
| $r$ | Distance from the pillar center | μm |
| $K_d$ | dissociation constant | M |
| $Th_{agg}$ | Binarization thresholds for the intensity of all aggregates | - |
| $Th_{pillar}$ | Binarization thresholds for the intensity of pillars | - |
| $I_{agg-max}$ | Max binarization thresholds for the size of aggregates | - |
| $I_{agg-min}$ | Minimum binarization thresholds for the size of aggregates | - |
| $I_{pillar-min}$ | Minimum binarization thresholds for the size of pillars | - |
| $D_{dif}$ | Diffusion coefficient | m/s |
| $k_B$ | Boltzmann's constant | |
| $T$ | Absolute temperature | K |
| | Time period | |
| $\mu$ | Viscosity of fluid | mPa × s |
| | | |
| $\delta_s$ | Stokes boundary layer thickness | |
| $\nu$ | Kinematic Viscosity of fluid | m²/s |
| $\omega$ | Angular frequency | |
| $\delta$ | Half-height of the computational domain | μm |
| $D_{MP}$ | Diameter of target microparticle | μm |
| $D_{NP}$ | Diameter of capture nanoparticle | μm |

| | | |
|---|---|---|
| $P$ | Capture distance | μm |
| $\phi_0$ | Level-set function | - |
| $\phi$ | Phase-identification function | - |
| $\tau$ | Shear stress | mPa |

This thesis is based on:

Kanji Kaneko, Zhitai Huang, Taku Sato, Naoto Ujikawa, Takeshi Hayakawa, Yosuke Hasegawa, Hiroaki Suzuki, Investigation of the vibration-induced local flow around a micro-pillar under various vibration conditions, *Mechanical Engineering Journal*, 2023, Volume 10, Issue 1, Pages 22-00223

Kanji Kaneko, Mamiko Tsugane, Taku Sato, Takeshi Hayakawa, Yosuke Hasegawa, Hiroaki Suzuki, Vibration Induced Flow Facilitating Affinity-Based Aggregation for Rapid Detection and Quantification of Nanoparticles", (under review at *Scientific Reports*).

# Chapter 1.

# Introduction



- **Chapter 1**: Introduction
- **Chapter 2**: Flow field measurement of the VIF (vibration-induced flow)
- **Chapter 3**: Detection of nanoparticles using the VIF-induced aggregation
  - Effectiveness of VIF system on the aggregate formation
  - Effect of vibration conditions/pillar arrangement
  - Quantification of NP concentration
- **Chapter 4**: 3D numerical simulation of VIF

Validation of numerical simulation

Particle capture simulation

- **Chapter 5**: Detection of exosomes for practical application
- **Chapter 6**: Conclusion

## 1.1.  Detection of bioactive nanoparticles (NPs) in the life sciences

Identification of target substances using ligand molecules has been extensively utilized for disease diagnosis and monitoring (Fan and Poetsch 2023)(Yoshioka et al. 2014)(Boriachek et al. 2018)(Shen et al. 2018), basic research on infectious diseases (Zhu et al. 2020)(Huang et al. 2020), and environmental pollutant detection (Justino et al. 2017). There is a pressing need for detection methods that are both fast, sensitive, and cost-effective to enable early diagnosis and routine monitoring (Contreras-Naranjo et al. 2017)(Yu et al. 2018)(Bu et al. 2019). Immunoaffinity chromatography, a commonly used diagnostic tool, can rapidly detect antigens (in less than 10 min), but it suffers from low detection performance (approximately $10 \times 10^{11}$ /mL), and achieving quantitative measurement is challenging (Fig. 1-1 (a)) (Huang et al. 2015)(Fuchiwaki et al. 2018). In situations demanding more sensitive and quantitative detection, enzyme-linked immunosorbent assay (ELISA) is often the preferred method. While ELISA exhibits greater detection performance than immunoaffinity chromatography (approximately $10 \times 10^{8}$ /mL), it necessitates intricate multistep preparation and a relatively prolonged incubation time for antibody binding and enzymatic reactions (He et al. 2014). Alternative highly sensitive detection methods allow the direct identification of captured antigens on an antibody-coated solid substrate. For instance, identifying antigens adsorbed on affinity microbeads can be achieved through fluorescence-based flow cytometry (FCM) after fluorescence labeling (Hoen et al. 2012)(van der Vlist et al. 2012). Detection of antigen adsorption without labeling is also feasible using mass-based methods such as quartz crystal microbalance (QCM) and surface plasmon resonance (SPR) (Suthar et al. 2020)(Suthar et al. 2022)(Chen et al. 2021). However, these sophisticated apparatuses are typically limited to well-funded central laboratories. There is an ongoing need to develop a straightforward, rapid, and sensitive technique for detecting target antigens, especially for point-of-care (PoC) applications in common medical facilities and laboratories.
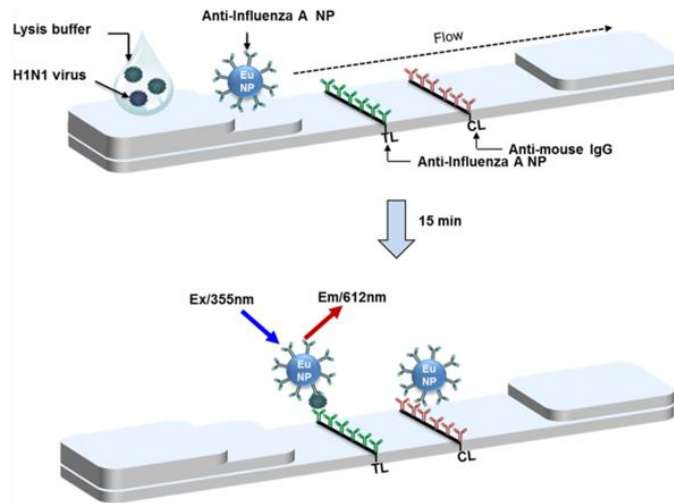
Fig. 1-1 (a) Detection of target substances using immobilized antibodies (immunochromatographic test) (Yu et al. 2018).

In the various immunoassays discussed earlier, relatively large targets such as extracellular vesicles (EVs) (Fig. 1-2), viruses, and bacteria are frequently the focus of attention (Boriachek et al. 2018)(Fong and Lipp 2005)(Harper-Owen et al. 1999). Due to the low diffusivity of these nanoparticles (NPs) compared to small molecules (e.g., proteins), it is essential to enhance the complex formation of NPs and immobilized antibodies to achieve rapid and sensitive detection (Ng et al. 2010). The employment of microbeads offers the benefit of an expanded surface area coated with antibodies to enhance effective adsorption (Sato et al. 2000)(Andersson et al. 2000)(Kuramitz 2009). The adsorption of antigens is additionally facilitated by actively mixing the beads and sample fluid; nonetheless, traditional bulk mixing methods (e.g., rotational agitation) are ineffective at scales below 100 μL. To achieve compact, rapid, and sensitive tools for NPs detection, diverse microfluidic systems have been developed (Contreras-Naranjo et al. 2017)(Ibsen et al. 2015)(Salafi et al. 2017)(Ibsen et al. 2017). In addition to simply minimizing the sample volume, these approaches offer the advantage of enhancing mixing by reducing the diffusion length. For instance, He et al. (He et al. 2014)(Zhao et al. 2016) developed a device for detecting EVs, crucial biological NPs in disease diagnostics, by blending the sample and affinity magnetic capture beads in a serpentine channel. While this method achieved on-chip EVs detection with high detection performance (limit of detection (LOD) $\sim 10 \times 10^5$ /mL), it necessitated fluorescence labeling and a highly sensitive imaging device. Xu et al. (Xu et al. 2018a) utilized a flow channel featuring Y-shaped micropillars to enhance the mixing of a flowing sample containing target EVs and affinity magnetic capture beads. They successfully detected tumor-derived EVs in a sample with high detection performance (LOD $\sim 10 \times 10^3$ /mL) using an electrochemical method (differential pulse voltammetry) downstream. PCR-based detection of EVs after capturing and

3

lysis in microfluidic devices has also been implemented (Shao et al. 2015a)(Lien et al. 2007)(Zhang et al. 2011)(Wang et al. 2011). In these instances, the processes of target capturing/enrichment and detection are separated and need to be sequentially performed in pre-existing systems. Additionally, achieving high detection performance requires either an expensive detection system or amplification machinery.
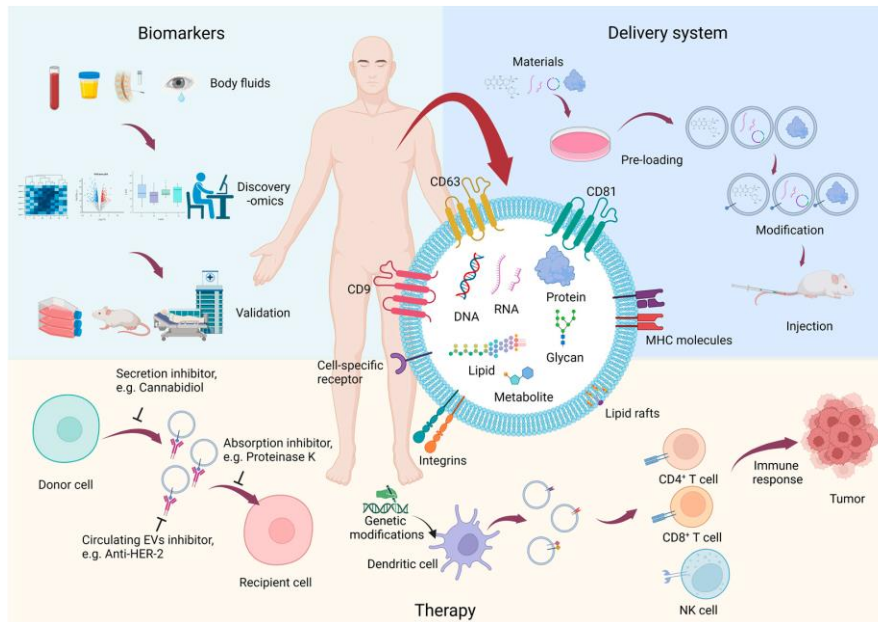


Fig. 1-2 Various applications of extracellular vesicles (EVs). (Fan and Poetsch 2023)

## 1.2. Immunoagglutination-based detection of biological substances

As a method for detecting target molecules without amplification or labeling, researchers have employed immunoagglutination assays (Molina‐Bolívar and Galisteo‐González 2005)(Fig. 1-3). In this method, the specific adsorption of target substances induces the aggregation of affinity capture particles (CPs), which is then detected through microscope observation or light scattering. This approach integrates the capturing of targets (adsorption to affinity CPs) and the detection process (optical detection of aggregate formation) to create a simple and cost-effective system. Nevertheless, the formation of aggregates with affinity CPs tends to be a gradual process, primarily attributed to the low diffusivity of CPs. In the 1990s, ultrasound was employed to accelerate aggregate formation, causing CPs to accumulate at the nodes of sound waves (Thomas and Coakley 1996). Microfluidic systems are anticipated to be a suitable platform for immunoagglutination assays (Wiklund et al. 2013). For instance, Han et al. (Han et al. 2007a) used a Y-junction microfluidic device to detect immunoglobulin G (IgG). Gupta et al. (Gupta et al. 2012) demonstrated that integrating

electrochemical impedance spectroscopy into a microdevice greatly improved the detection performance and detection time of IgG in the sample (Fig. 1-4). In these instances, the physical process of aggregate formation was not taken into account. To enhance the formation of aggregates, Castro et al. (Castro et al. 2018) encapsulated the immuno-CPs and the sample within a water-in-oil plug (droplet) propagating in a tube. The use of recirculating flow in a plug minimized the detection time. While this method and other micromixers hold promise for achieving rapid and reproducible aggregate formation, continuous flow-based systems often have larger dimensions and create non-negligible dead volume. The implementation of a straightforward and well-controlled active mixing method suitable for small sample volumes is expected to enhance the speed, efficiency, and reproducibility of detecting target substances with low diffusivity.
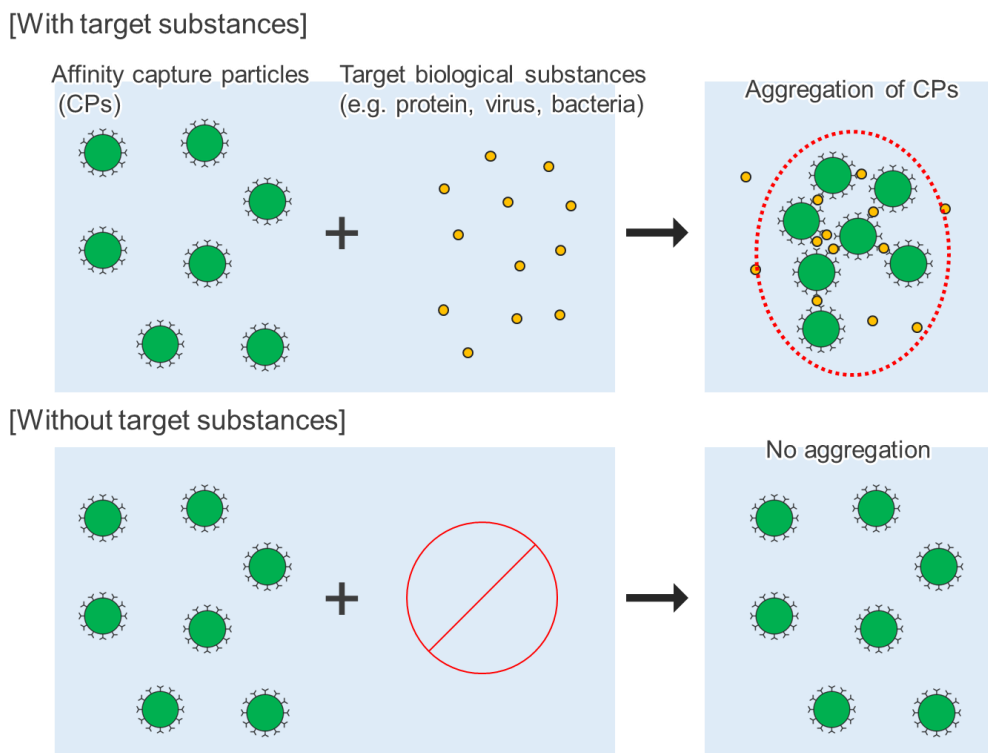


Fig. 1-3 Conceptual illustration of the immunoagglutination-based particle detection.
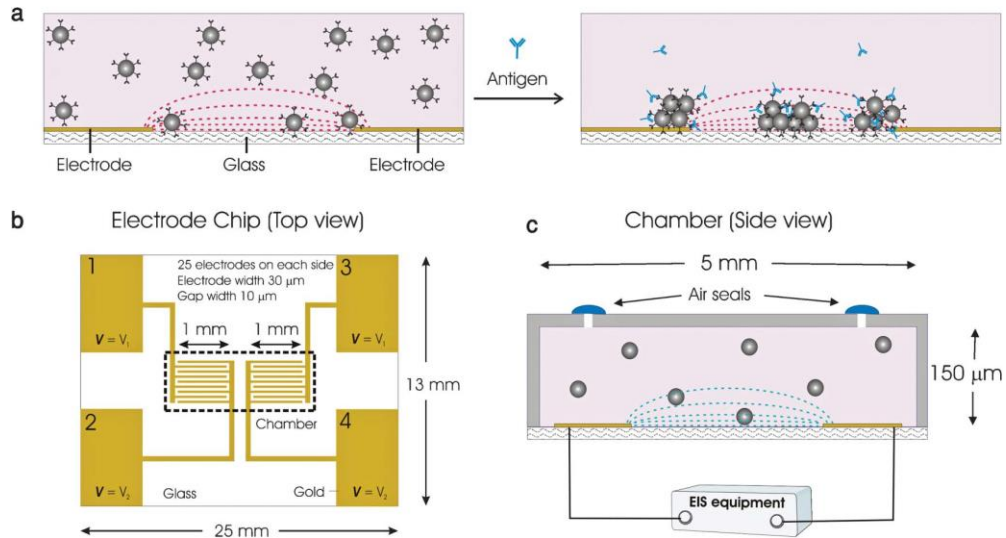
Fig. 1-4 A microfluidic system for immunoagglutination-based particle detection with electrochemical impedance spectroscopy. (Gupta et al. 2012)

## 1.3.  Micro vibration-induced flow (VIF) for active fluid control

In recent decades, microfluidics has offered diverse means of controlling fluids and micro/nanoparticles for biomedical analysis. Currently, the majority of microfluidic devices rely on external pumps (such as peristaltic, syringe, and pressure pumps), but these apparatuses inevitably contribute to the bulkiness of the system. The phenomenon of steady streaming (SS), capable of generating a net flow around a structure through zero-mean vibration, has been explored as a pump-free fluid control method. Among these, the acoustic streaming method has been extensively investigated to induce local flow around microstructures by applying acoustic waves above 1 kHz to the entire substrate emitted from a transducer attached simply to the microfluidic device. In addition, it is recognized that SS also occurs in an incompressible fluid subject to vibrations at a frequency as low as 1 kHz or even lower (Lutz et al. 2005; Lieu et al. 2012; House et al. 2014). This operational domain is frequently distinguished from acoustic streaming and is referred to as vibration-induced flow (VIF) (Hayakawa et al. 2014, 2015; Zhou et al. 2020a, b) (Fig. 1-5). Within this frequency range, precisely defined vibrations with relatively large amplitudes can be applied using laminated piezoelectric actuators. This method allows us to modulate vibration patterns to achieve advanced control of fluids and particles in a microfluidic chip. Earlier studies utilized VIF, including acoustic streaming flow, to improve the micromixing of two co-flowing fluids by inducing a local flow around

6

a sharp-edge (Huang et al. 2013; Nama et al. 2014, 2016) (Fig. 1-6). However, it still relies on a flow-based system.
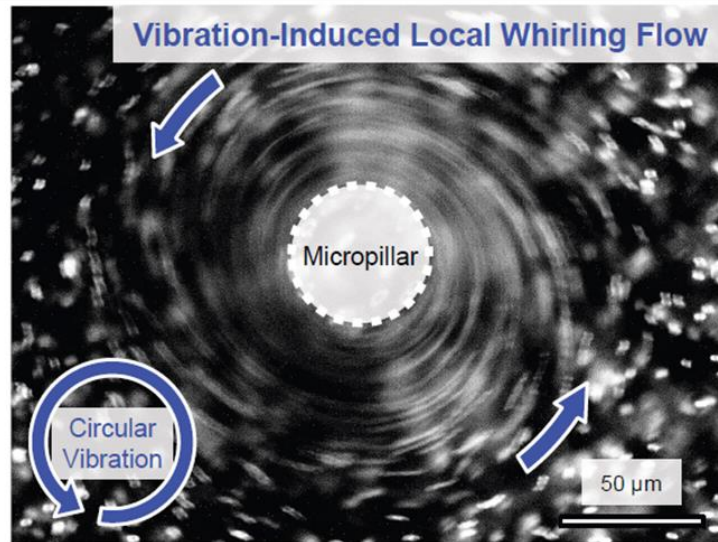


Fig. 1-5 Visualization of localized flow around microstructure with periodic vibration (Hayakawa et al. 2014).
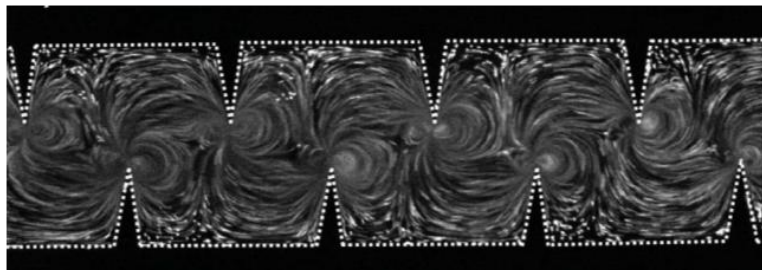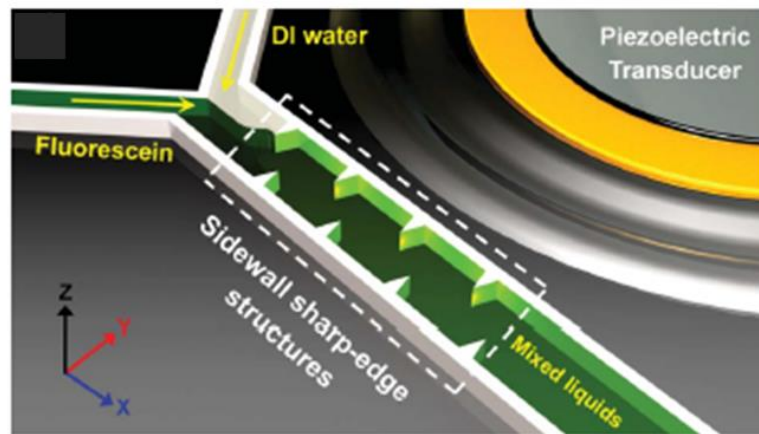
Fig. 1-6 (top) Schematic of the sharp-edge-based acoustofluidic mixing device. (bottom) Characterization of the flow pattern with acoustic streaming (Huang et al. 2013).

## 1.4. Numerical/theoretical approach for VIF system design

In the application of steady streaming (SS), theoretical analysis is often employed to predict flow and optimize the system. However, the complexity of sound wave propagation can vary depending on the channel structure in acoustic streaming, posing challenges for theoretical and numerical analyses. Several attempts have been made to theoretically reproduce acoustic streaming flows. In two-dimensional (2D) flow scenarios, theoretical analyses considered fluid compressibility to describe particle behavior in the fluid (Huang et al. 2013; Nama et al. 2014, 2016). For three-dimensional (3D) flow around structures with simple geometry, some studies utilized perturbation theory under the assumption of incompressible flow (Rallabandi et al. 2015; Volk et al. 2020). Nonetheless, the suitability of these approaches is constrained to situations where the vibration amplitude is notably smaller than the typical length scale of the structure.

Similarly, numerical predictions for the VIF system pose significant challenges. The system involves unsteady flow with moving boundaries, incurring a large computational cost for direct computation. Consequently, numerical simulations have been conducted under certain constraints. Various analyses have employed the stream function, assuming small perturbations, to obtain 2D flow fields induced around simple microstructures (Lutz et al. 2006; Hayakawa et al. 2018). Although these reports accurately predict streamlines, aligning well with experimental results regarding the locations of particle traps at stagnation points, they commonly assume a small vibration amplitude concerning the typical length scale of the structure. This limitation results in inaccurate predictions of velocity distribution for a finite vibration amplitude. Amit et al. performed direct calculations of the 3D flow around a periodically vibrating object using the finite element method with moving boundaries (Amit et al. 2016); nevertheless, this was limited to a simple cantilever. Zhou et al. calculated the SS flow field around a microstructure with a complex shape using a commercial solver (COMSOL Multiphysics), intending to drive micromotors through system vibration (Zhou et al. 2020b). Nevertheless, this method was confined to 2D analysis, mainly because it is challenging to apply appropriate boundary conditions at the fluid-solid interface of complex geometries. Certainly, in the practical implementation of VIFs in fluidic and particle manipulation systems, intricate geometries are frequently utilized in fluid conduits to achieve efficient three-dimensional (3D) manipulation, transport, and separation of cells (Hayakawa et al. 2015; Hayakawa and Arai 2017).

Therefore, the construction of a numerical model capable of solving 3D VIF under various conditions is anticipated to be applicable in predicting particle behavior during stirring for particle detection.
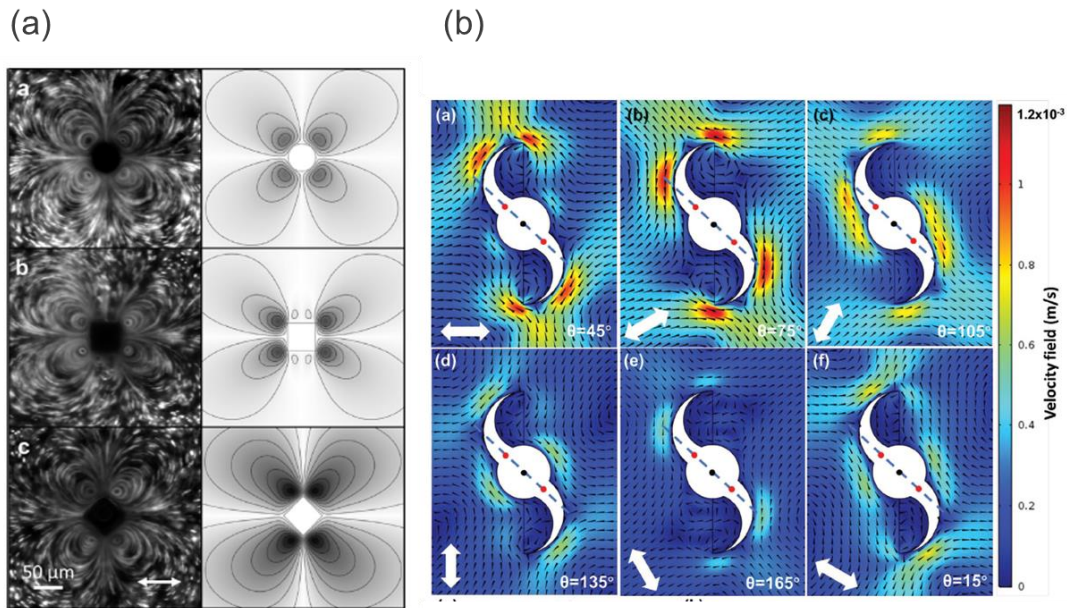
Fig. 1-7 2D theoretical analysis of vibration-induced flow. (a) Particle imaging experiments (left column) are compared to the computed Lagrangian streamlines (right column) for channel obstruction geometries (Lieu et al. 2012). (b) Numerical simulation of the fluid flow velocity profile around 2-arm microrotor under various stage vibration directions (Zhou et al. 2020b)

## 1.5.    Motivation for this work

In the aforementioned background, the immunoagglutination method, while providing a convenient means to detect biological substances, often utilizes CPs and target substances of nanometer-scale size, leading to the necessity of external equipment, such as spectrophotometers for accurate detection. On the other hand, in detection employing relatively larger capture particles (hereafter referred to as CPs) of few micrometer-scale size, observable CP aggregates in the bright field in a standard microscope view enable the detection of target substances. However, the particle collision required to induce aggregation depends on particle diffusion and is time-consuming. Consequently, the lack of actively induced particle collisions leads to low detection performance, posing a challenge in terms of detection performance compared to conventional methods like ELISA.

In this thesis, we adopted a fluid-control technique based on vibration-induced flow (VIF) for immunoagglutination-based NP detection (Fig. 1-8). The rationale behind selecting the VIF technique is as follows: firstly, the collision of NPs/CPs can be enhanced through stirring induced by reproducible local flows around the microstructure. Previously, VIF (including acoustic streaming flow) was applied to enhance micromixing (Huang et al. 2013; Nama et al. 2016; Rallabandi et al.

2017). Secondly, the precise control of flow patterns is achieved by adjusting such as pillar geometry and vibration parameters. Finally, the use of a VIF system eliminates the need for external pumps, enabling the handling of small sample volumes on the order of a few microliters. By combining VIF and immunoagglutination-based NP detection, our objective is to realize a system for on-the-fly NP detection in a minute sample (down to 5 µL), integrating sample mixing and NP quantification into a single step.

As a guideline for the system design, we constructed a three-dimensional numerical simulation tool for predicting the VIF under various vibration conditions. The obtained simulation results are validated through comparison with the PIV measurement results. Furthermore, we conducted a numerical simulation of particle capture by using the developed numerical tool to model the initial stage of aggregation with CP and target NP.

Finally, we demonstrated that the EV concentration can be evaluated using T-cell immunoglobulin and mucin domain-containing protein 4 (Tim-4)-conjugated magnetic CPs (Miyanishi et al. 2007; Nakai et al. 2016) to validate the usefulness of the system for diagnostic applications.
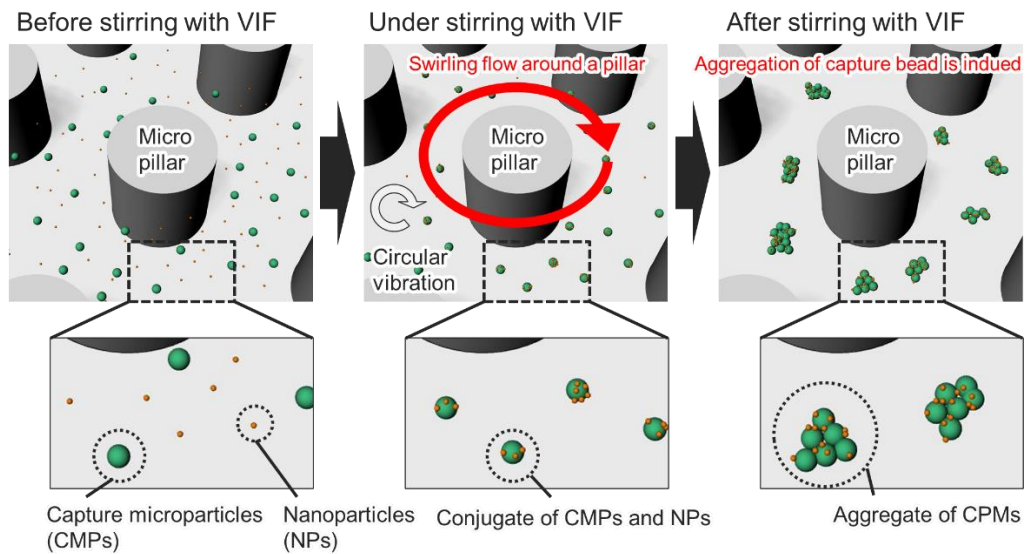
Fig. 1-8 Schematic of NPs detection based on the aggregation of affinity CPs induced by vibration-induced flow (VIF).

## 1.6. Plan of this thesis

This thesis is structured into six chapters: In Chapter 2, we introduce the fabrication process of the micropillar substrate and the experimental setup. Using the fabricated substrate, we investigated

the flow fields around the micropillar using micro-PIV. In Chapter 3, we explore the applicability of the vibration-induced flow technique for immunoagglutination-based NPs detection. We describe the relationship between flow fields under various vibration conditions and NPs detection. In Chapter 4, we construct a numerical simulation tool for predicting the 3D flow field around micropillars. We also perform particle capture simulations during the initial stages of aggregate formation using this developed numerical simulation tool. In Chapter 5, we conducted an experiment for detecting exosomes, verifying the practical application of our system for the detection of bioactive NPs. Finally, Chapter 6 provides a summary of the thesis.

# Chapter 2.

# Flow field measurement of the VIF
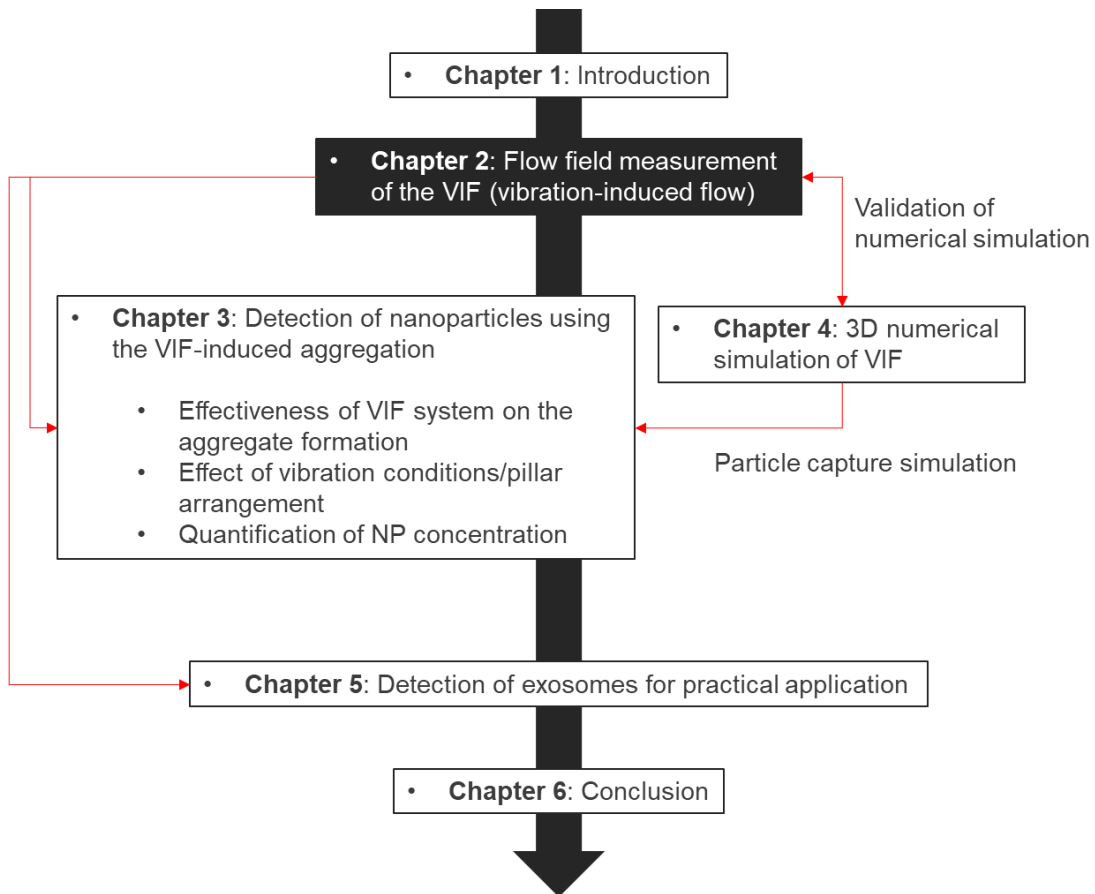
## 2.1. Overview

In this chapter, we conducted measurements of the local flow field around the oscillating micropillar before applying VIF to the aggregate formation of affinity CPs through the stirring of target NPs and CPs. There has been scarce research examining the relationship between the flow field and aggregation formation. By measuring the flow field around pillars, the effect of flow field characteristics on aggregation formation can be investigated, leading to an appropriate VIF system design for detecting NPs.

We first fabricated a micropillar substrate. Specifically, a Si master mold of a micropillar substrate was fabricated using standard photolithography and deep reactive ion etching (DRIE) processes. Subsequently, PDMS pillar substrates were created through replica molding. In the VIF field, it is known that various flow patterns can occur under different vibration conditions such as vibration frequency/amplitude, vibration direction, and geometry of micropillar (Hayakawa et al. 2015; Hayakawa and Arai 2017; Zhou et al. 2020b). However, there is limited study that precisely measures and compares the characteristics of these diverse flow fields. We employed micro-PIV (particle image velocimetry) to measure the unsteady flow field in VIF. The influence of vibration conditions, including vibration frequency and amplitude, as well as pillar shape, arrangement, and height on the flow field, was investigated. Some of the flow fields obtained in this chapter are then compared with those obtained in the numerical simulation of VIF in Chapter 4 to validate the numerical simulation results.

## 2.2. Experimental procedures

### 2.2.1. Fabrication of micropillar substrate

First, we fabricated a micropillar substrate. Here, mold fabrication via the deep reactive ion etching (DRIE) process and subsequent replica molding was performed to create pillar substrates. Fig. 2-1 shows a representative 2D CAD image of a micropillar substrate. Cylindrical micropillars with 100 μm diameter were arranged in a 35 × 35 square array. We choose a simple cylindrical pillar shape to make the fabrication process easy. Square and rectangular structures were arranged near the sides of the substrate as spacers to determine the height of the fluid volume. Pillar heights were set to $h =$ 50 and 100 μm through the DRIE process. Fig. 2-2 depicts the dimensions of the micropillar substrate. We set pillar separation (center-to-center intervals) as $S = 200, 400,$ and 600 μm (Fig. 2-2 (a-c)) in a square array. A hexagonal-type array was fabricated for the $S = 400$ μm case (Fig. 2-2 (d)).

The selection of the specific pillar height is based on a thorough consideration of the fluid dynamics surrounding the pillar. In a case where the pillar height is too short, typically within the

range of several μm, flow induction around the pillar may not manifest within several hundred Hz due to the drag effect from both the top and bottom walls (This drag effect arises from the development of the stokes boundary layer on both substrates.). In situations where pillars are longer, extending over several hundred μm, there is no specific optimal value, but excessively long pillars can complicate fluid handling and microscopic observation. Additionally, limitations in the fabrication process using DRIE can arise. Hence, we adopted pillar heights of 50 and 100 μm. Regarding the pillar diameter, our earlier work (Hayakawa et al. 2015) found that the diameter of the pillar did not significantly impact induced velocity. For this study, a diameter of 100 μm was selected to maintain a moderate aspect ratio of height to diameter, simplifying the fabrication process. Additionally, we explored the influence of various pillar geometric conditions by varying the separation and arrangement of pillars.
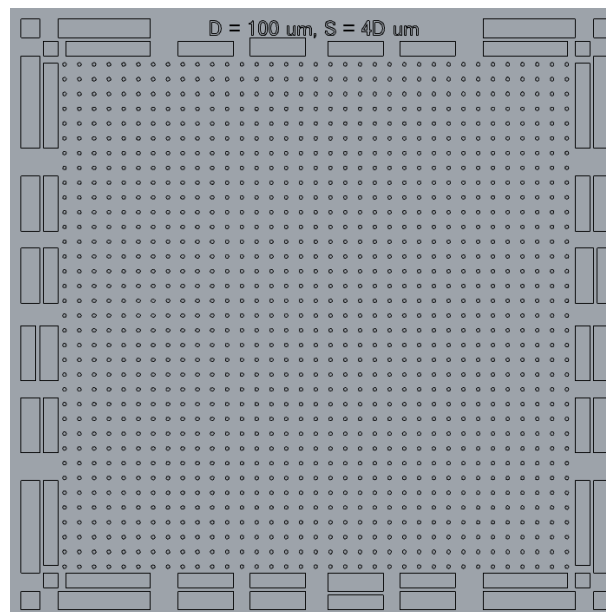


Fig. 2-1 Design of micro-pillar substrate illustrated with CAD software.
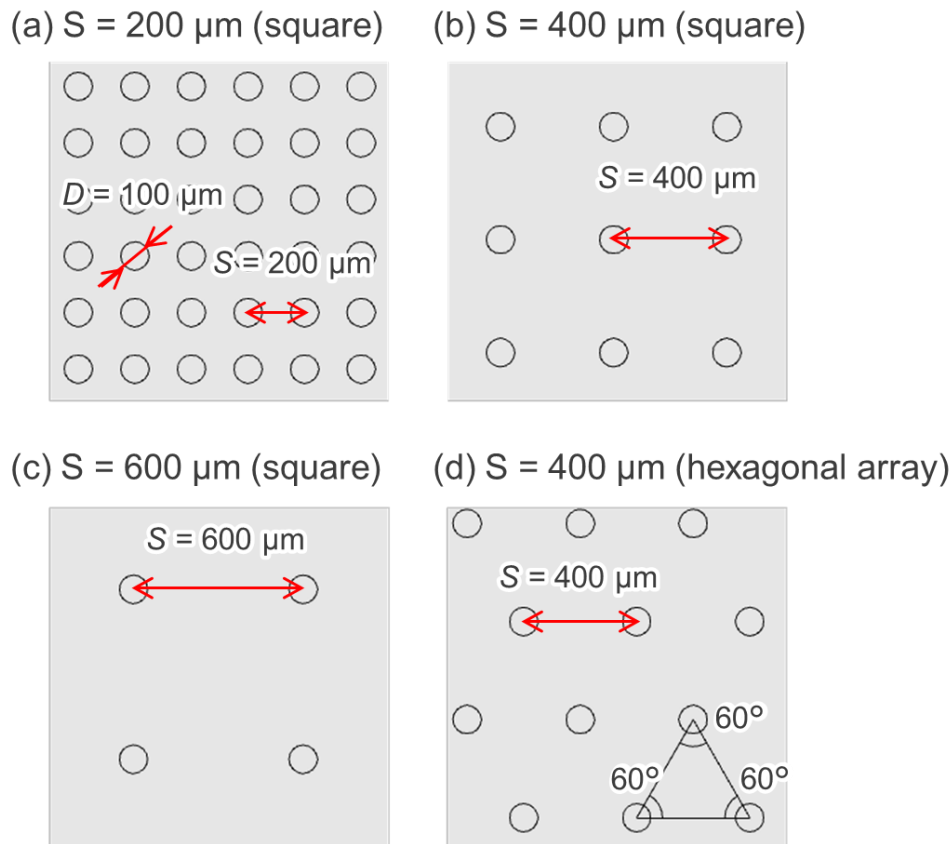
Fig. 2-2 Design parameters of the micropillar array with $S =$ (a) 200 μm, 400 μm, and 600 μm in square type array, and (d) $S =$ 400 μm in hexagonal type array.

The created CAD design was drawn onto a photo mask blank via UV exposure using a maskless exposure apparatus. Subsequently, the pattern was developed for approximately 35 seconds using the NMD developer solution. Following this process, chromium etching was carried out for around 80 seconds using a chromium etchant. After the completion of the etching process, the mask was immersed in acetone and the resist was cautiously removed while stirring for more than a minute. The photoresist residues were completely removed with plasma ashing treatment using a compact etcher for 5 min (O2 flow rate: 20 mL/min, 75 W) (FA-1, Samco Inc., Kyoto, Japan). Fabricated photomask is shown in Fig. 2-3.

Fig. 2-3 The photomask after development.

Next, we fabricated a master mold of micropillar substrate via DRIE. The series of processes is depicted in Fig. 2-4 (a). A silicon wafer was dehydrated by baking on a 150 ℃ hot plate for 15 min. After the baking, the surface of the Si wafer was made hydrophobic to enhance the adhesion b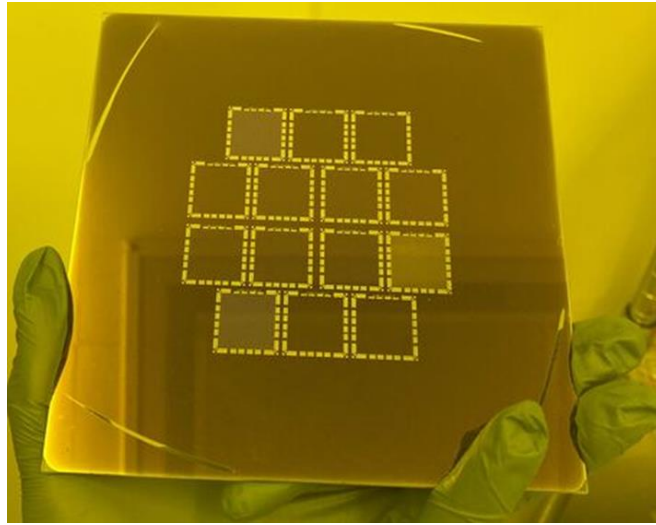etween the photoresist and the wafer. In practice, the wafer was positioned in the same container with a few drops of Hexamethyldisilazane (HMDS) for 10 min. Subsequently, AZ P4620 positive photoresist (AZ Electronic Materials) was spin-coated at 3000 rpm for 30 s on the surface of the wafer. The wafer was baked for 1 min at 110 ℃, and exposed and developed using standard (exposure time was set to 10 s using a mask aligner). The wafer was meticulously developed by immersing it in an NMD developer.

The BOSCH process was conducted using a deep reactive-ion etching (DRIE) apparatus (RIE-400iPB, Samco, Kyoto, Japan). The BOSCH process is an etching technique that achieves rapid and high aspect ratio silicon etching by alternately repeating two steps: isotropic etching and deposition of a protective layer. During the etching process, isotropic etching with $SF_6$ is performed, while the protective film formation process uses $C_4F_8$ to safeguard the sidewalls and suppress lateral etching. In this instance, the processing program was set to Recipe No. 4, carrying out 255 cycles of processing. Once the silicon wafer underwent the etching process, it was subjected to acetone cleaning, completely removing the resist. The manufactured silicon wafer mold is presented in Fig. 2-4 (b).
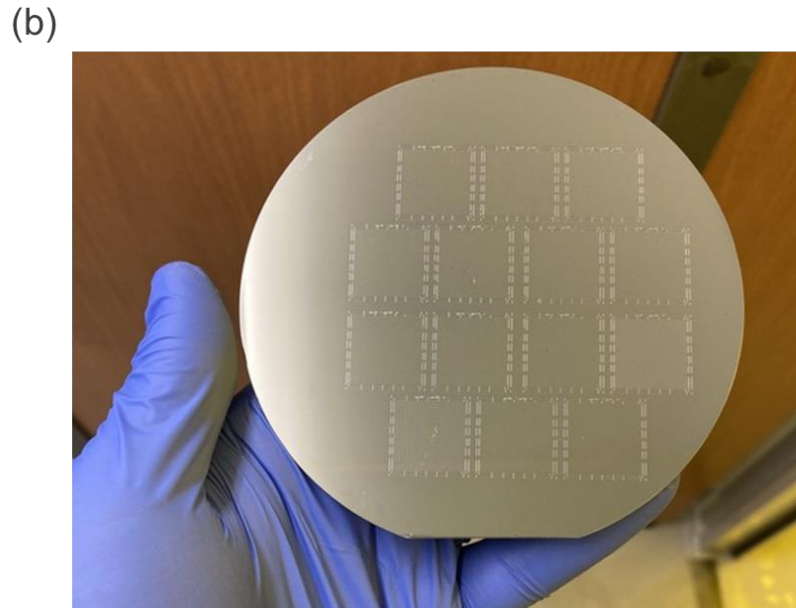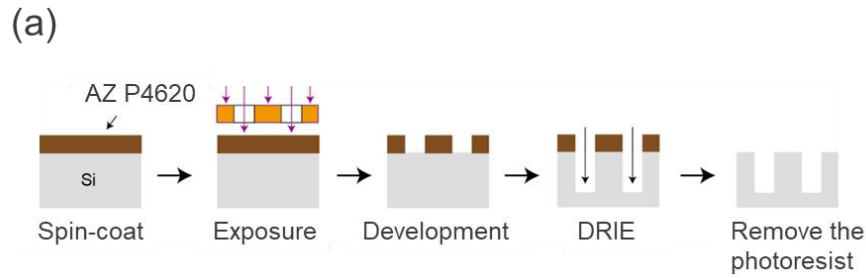
Fig. 2-4 (a) Fabricating process of micro s pillar substrate with DRIE. (b) Silicon master mold fabricated with DRIE process.

Subsequently, the replication process involved molding from the master Si wafer mold using polydimethylsiloxane (PDMS). To prevent PDMS adhesion to the etched master mold, a releasing agent (FLUOROSURF FG-5084, FluoroTechnology Co., Ltd., Japan) was applied to the silicon mold and dried on a hotplate at 120 °C for 20 min. A PDMS mixture (SILPOT 184 W/C, Dow Corning Inc., USA) was prepared by combining the resin with its curing agent at a weight ratio of 10:1, and the resulting mixture was poured into the master mold. Following curing at 80 °C for 180 minutes, the PDMS substrate was obtained by carefully removing the mold (Fig. 2-5 (a)). Fig. 2-5 (b) and Fig. 2-6 display an SEM image of the fabricated PDMS micropillar.
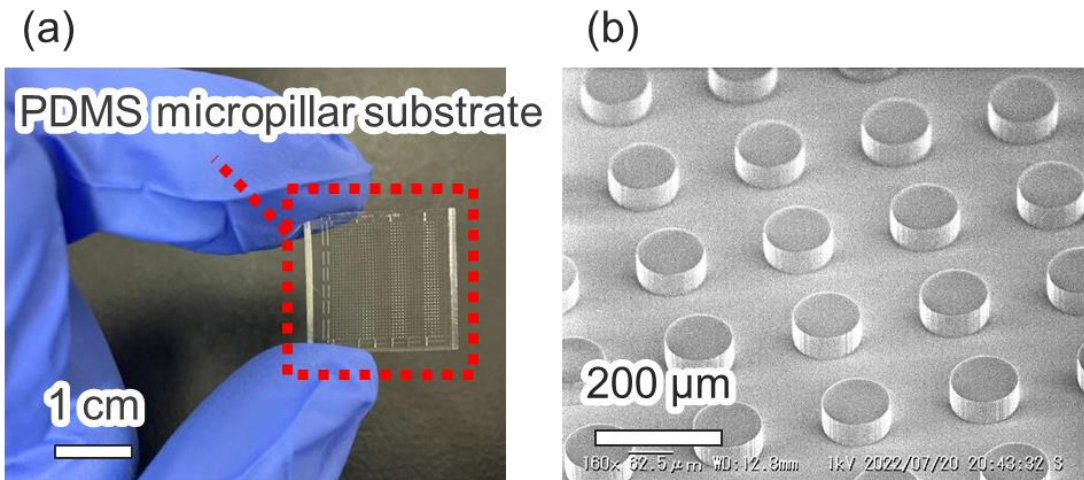
Fig. 2-5 (a) PDMS substrate with the micropillars in the actual image. (b) SEM images of micropillar with a geometric condition of $h = 50$ μm and $S = 200$ μm.
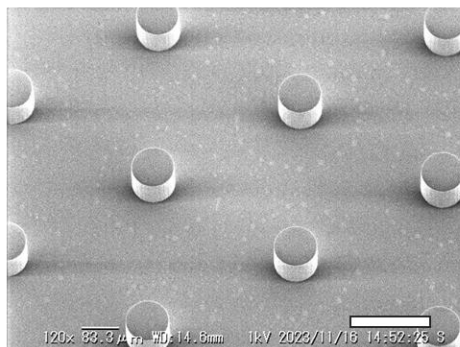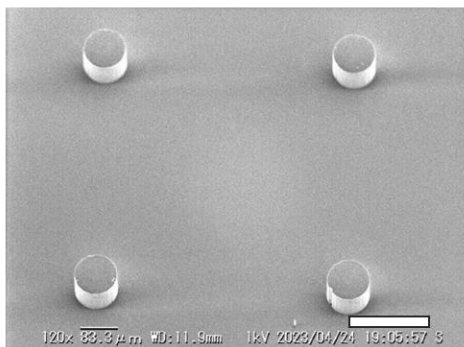


Fig. 2-6 SEM image of PDMS substrate with a height of 100 μm in different arrangements. $S =$ (a) 200 μm, (b) 400 μm, and (c) 600 μm in a square array, and (d) $S = 400$ μm in a hexagonal array.

### 2.2.2. Experimental setups

The experimental configuration is depicted in Fig. 2-7. To render the substrate hydrophilic and prevent air bubble entrapment around the pil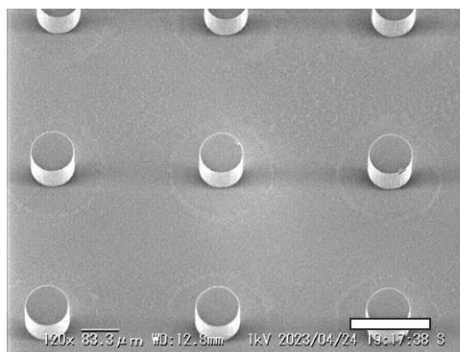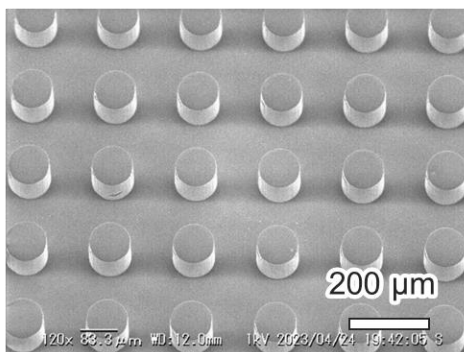lars, a 3 min oxygen plasma treatment (PDC-32G, Harrick Plasma, USA) was applied. Following this treatment, 8 μL of deionized (DI) water containing 1 μm yellow-green fluorescent beads (17154-10, Polysciences, Inc., USA) as a tracer was carefully dispensed onto the center of the substrate (Fig. 2-7 (a)). The substrate was then covered with a glass cover. This assembly was securely affixed to the XY piezo-drive stage (ML-20XYL, MESS-TEK, Japan) using small pieces of double-sided tape (Fig. 2-7 (b)). For vibration conditions utilized in the aggregation test, PDMS surface treatment with a BSA solution, as outlined in Chapter 3, was performed.
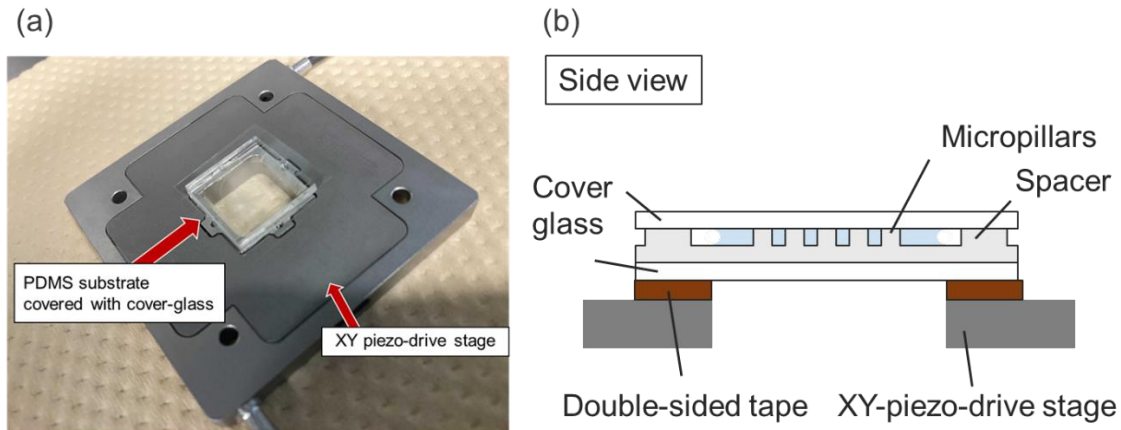


Fig. 2-7 (a) Schematic and (b) actual image of the assembled micro-pillar substrate fixed on the piezo-drive stage.

Fig. 2-8 provides an overview of the VIF system. Circular vibration was induced by applying two sinusoidal wave signals with a 90° phase offset to the piezo stage using a waveform generator (AG 1022F, OWON, China) via the amplifier (M 2501-1, MESS-TEK, Japan). In the case of rectilinear vibration, a single sinusoidal wave signal was applied to the piezo stage.

For the measurement of the flow field, a high-speed camera (DFK33UX174, The Imaging Source, Inc, Germany) was employed to capture the motion of particles at a rate of 100 fps with an exposure time of 1/5000 s (200 μs). In situations where the camera could not adequately resolve the flow field, another high-speed camera (TMX 6410, Phantom, USA) was utilized at a frame rate of 100 fps with an exposure time of 1/50000 s (20 μs). These were achieved using a high numerical aperture objective lens (UCPlanFLN 20x/0.70, Olympus, Inc, Japan). For observation of a wider range of flow

fields, a low magnification lens was used to capture a multitude of pillars within the imaging field (A-Plan 10x Objective Lens, ZEISS, Germany).
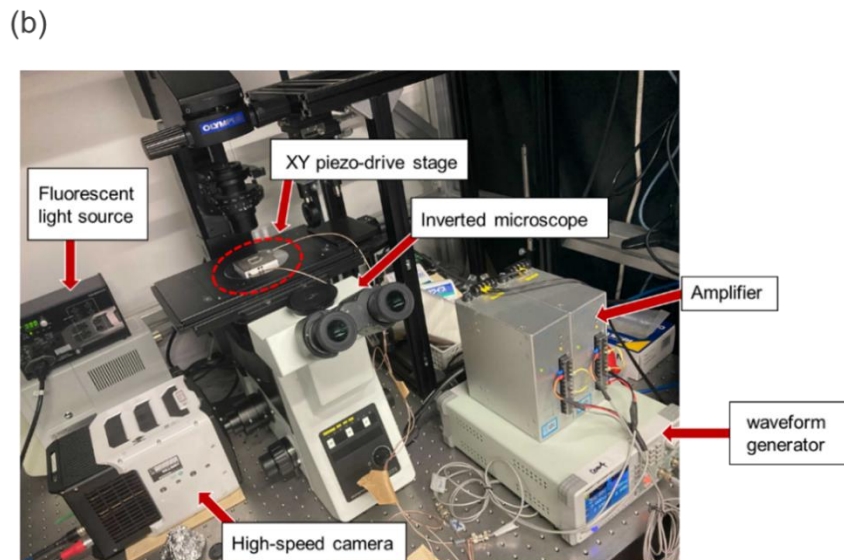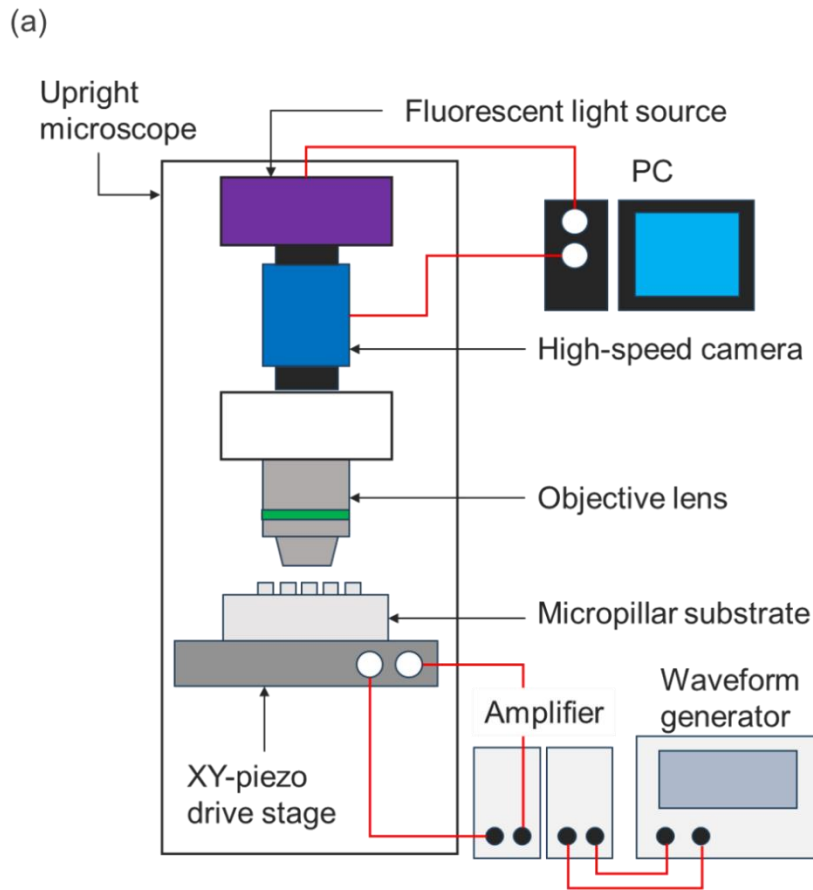


Fig. 2-8 (a) Schematic and (b) actual image of an overview of the VIF system.

### 2.2.3. Measurement of amplitude of vibrating pillar

A piezoelectric actuator converts electrical energy into mechanical energy such as displacement and force. The piezoelectric actuator (MESS-TEK, ML-20XYL) used in this study operates similarly, with the displacement determined based on the magnitude of the input voltage. We investigated the relationship between input voltage, frequency, and output displacement. In practice, images of pillars in a vibrating state under applied voltage were captured in a bright field image. The amplitude was determined by comparing the pillar diameter in the static state and the vibrating state using image analysis software (Image J).

In our system, the input voltage sent from the signal generator (Function generator) was amplified 30 times before being applied to the piezo stage. The voltage values shown in Fig. 2-12 (unit: Vpp) represent the post-amplified values.

### 2.2.4. Visualization of streamline

To visualize streamlines around micropillars, the trajectory of 1 μm diameter fluorescent tracer particles was overlaid using an objective lens with a 1s exposure time.

### 2.2.5. PIV measurement

We employed the micro-PIV (Particle Image Velocimetry) technique for measuring the flow field surrounding micropillars (Fig. 2-9). Utilizing this approach, sequential images of tracer particles are captured with a high-speed camera which can resolve the motion of the particle. Here, particles around the oscillating micropillar exhibit a net/mean motion attributable to their rotational motion which follows the trajectory of oscillation (Fig. 2-10). During this motion, the particle trajectories synchronize with the oscillation frequency. In PIV measurements, the presence of the effect of actual oscillation of particles when taking mean flow images may cause measurement errors. Therefore, it is essential to capture the net motion of the particles, so frame rate and shutter speed (exposure time) should be selected appropriately. For selecting them, it is necessary to capture the particles at an identical phase in the rotational motion. For shutter speed, a smaller shutter speed reduces particle blur. With the shutter speed described earlier, relatively clean particle images can be obtained with minimal blurring. A shutter speed should be set carefully as it has an impact on brightness.

Using the obtained images, we calculated the time-averaged Lagrangian velocity field through the correlation of particle images obtained at nearly identical phases in the periodic motion employing PIV software (Flow Expert, KATO Koken, Japan). The velocity was obtained employing a direction cross-correlation method. The interrogation window size was set at 16 pixels × 16 pixels

(14 μm × 14 μm in the physical dimension, 0.9 μm/pixel) in the cylindrical pillars subjected to the circular vibration.
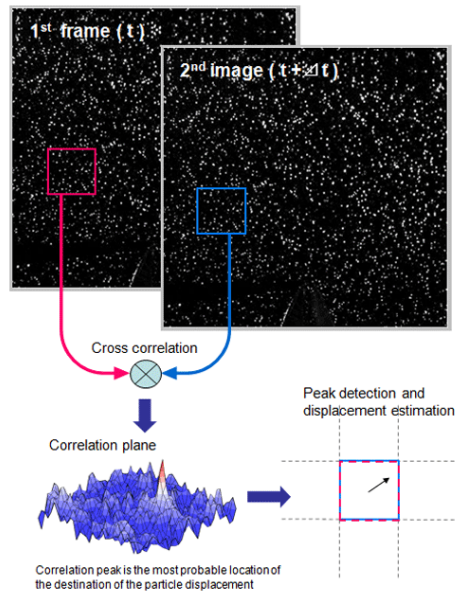


Fig. 2-9 Schematics of measurement algorithm of PIV (Particle Image Velocimetry).

https://www.seika-di.com/en/measurement/principle_of_piv/piv_system.html
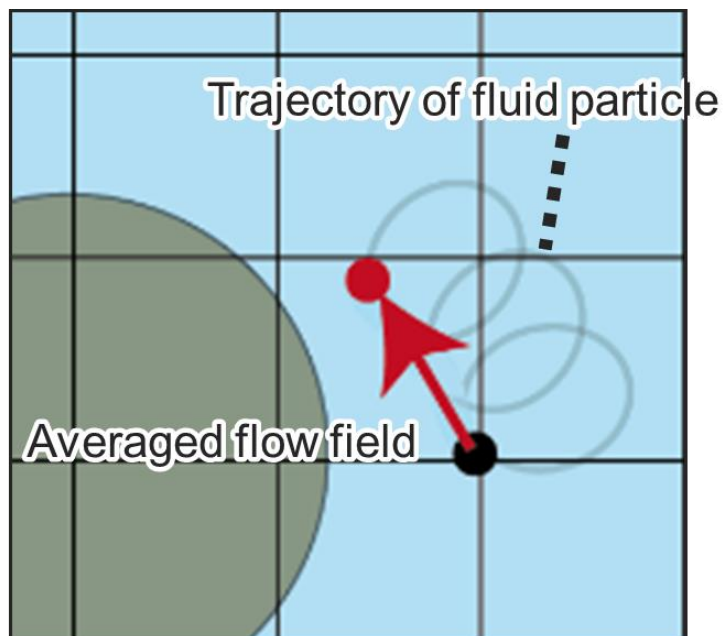


Fig. 2-10 A 2D trajectory of a particle following a local oscillation.

## 2.3. Visualization and PIV analysis of VIF

### 2.3.1. Relationship between applied voltage and pillar amplitude

First, the relationship between applied voltage and displacement of micropillar was examined. Fig. 2-11 (a) shows a bright field image of a pillar without vibration. Upon circular vibration being applied, the pillar oscillates with circular motion (Fig. 2-11 (b)). The amplitudes obtained at different frequencies and input voltages are presented in Fig. 2-12. When the vibration frequency was constant, the amplitude of the pillar was increased as the applied voltage increased.

(a)                                                    (b)
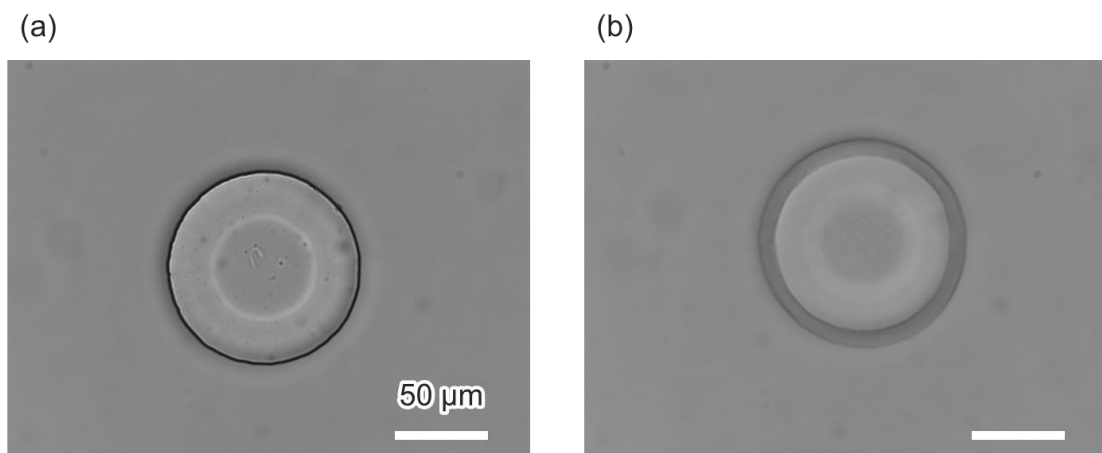


Fig. 2-11 Raw image of a pillar in (a) stationary and (b) vibrating state at a condition of $f = 800$ Hz and $V = 60$ Vpp.
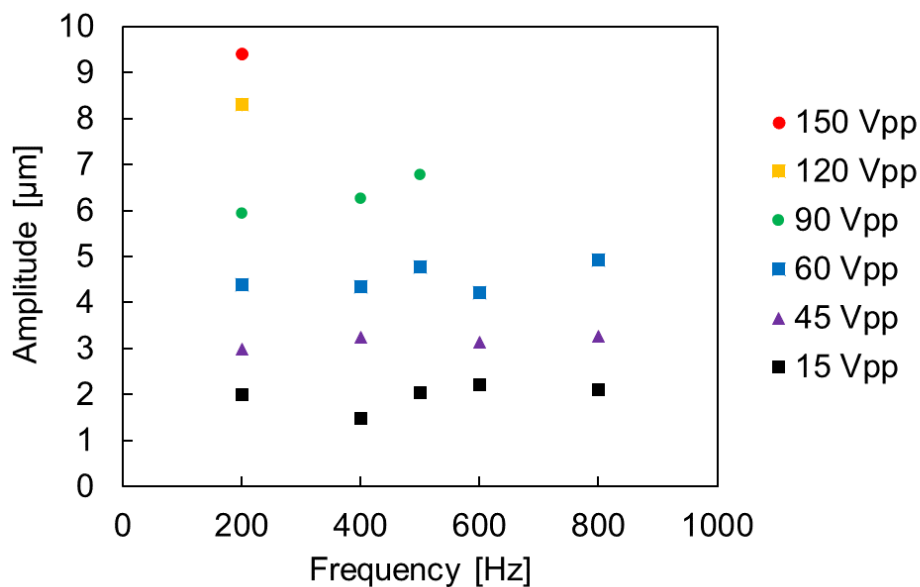


Fig. 2-12 Relationship between applied voltage from a function generator and the amplitude of pillar.

## 2.3.2. Effect of the vibration frequency and amplitude

In the initial step, we conducted flow field measurements under the geometric conditions of $S = 200$ µm and $h = 50$ µm. As illustrated in Fig. 2-13, the flow field at the middle plane of the pillar height ($y = 25$ µm) was examined under the vibration conditions of $f = 500$ Hz, and $A = 3.3$ µm. Fig. 2-13 (a) shows 2D streamlines. Although tracer beads moved along the rotating trajectory following the rotational vibration, the net displacement was swirling along the pillar sidewall can be seen. The corresponding 2D vector plots, obtained through PIV analysis in a series of images, are presented in Fig. 2-13 (b), revealing swirling flow patterns around the pillar. The velocity magnitude was approximately 160 µm/s, with slight reductions at the top, bottom, left, and right sides of the pillar. This deceleration is attributed to interference with neighboring pillars spaced at center-to-center intervals of $S = 200$ µm. Fig. 2-13 (c) displays radial profiles of the azimuthal velocity, with the peak position situated around $r = 63$ µm, 13 µm away from the pillar sidewall. The profile decayed radially as the distance from the pillar sidewall increased.
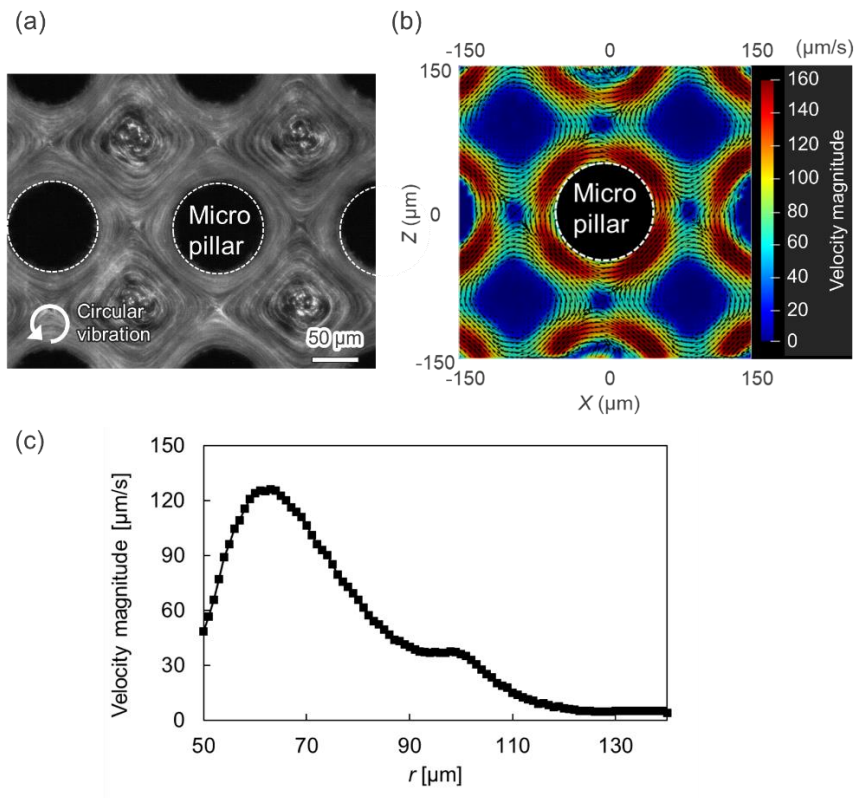


Fig. 2-13 (a) Streamlines of the velocity field around the cylindrical micropillar. (b) 2D vector plot of the net velocity around a pillar obtained with PIV measurement. (c) Azimuthal velocity profiles as a function of the distance from the pillar center ($r$).

In the VIF field, parameters related to vibration, such as frequency and amplitude, exert significant influence on the localized flow field dynamics (Hayakawa et al. 2015). Here, we varied the vibration frequency ($f$) and the amplitude ($A$). Fig. 2-14 shows the relationship between the peak velocity magnitude and the vibration parameters frequency and amplitude. Velocity magnitude represents a peak value of the azimuthal velocity profile. The induced velocities exhibited a positive correlation with increasing vibration frequency and amplitude, implying the feasibility of fine-tuning induced velocities using these parameters.
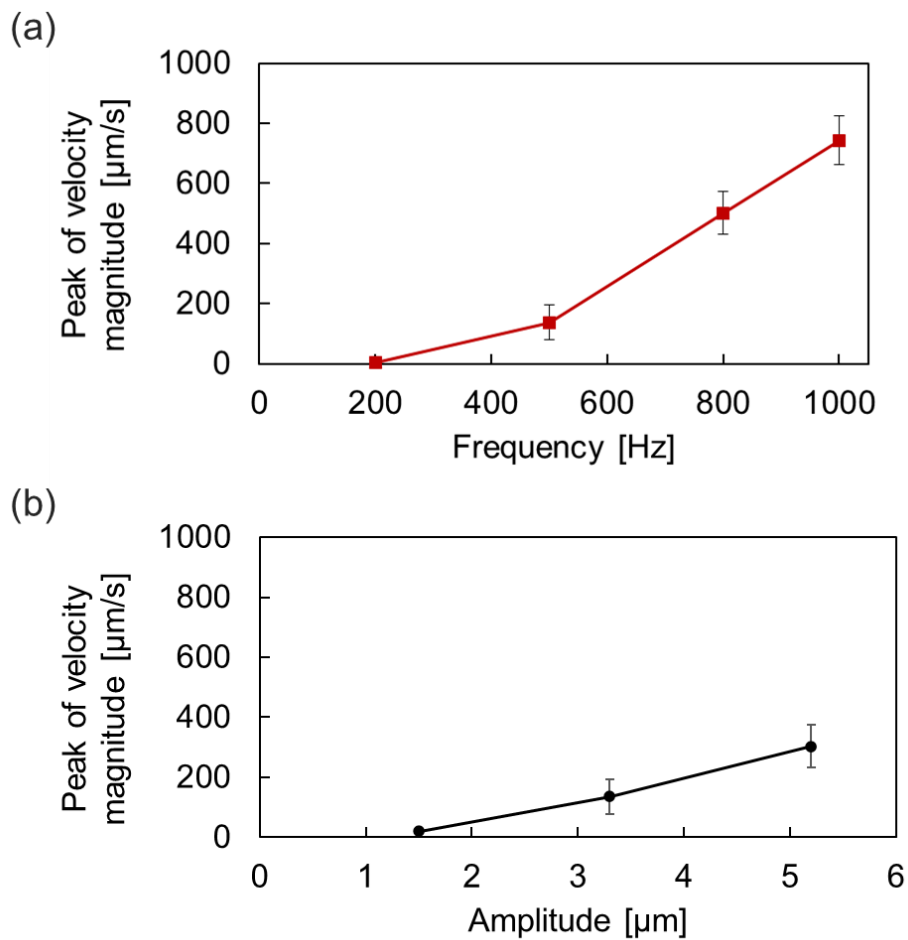


Fig. 2-14 Relationship between the peak velocity magnitude and the vibration parameters of (a) frequency and (b) amplitude, respectively. Error bars indicate the standard deviation from triplicate experiments.

### 2.3.3.    Effect of pillar height

Next, we investigated the effect of pillar height on flow fields. Two kinks of pillar height $h$ = 50 μm and $h$ = 100 μm for $S$ = 400 μm were tested. Fig. 2-15 illustrates a two-dimensional (2D) vector plot of the net flow velocity at the central plane of the pillar. The vibration condition was set to $f$ = 600 Hz, $A$ = 2 μm. For lower case ($h$ = 50 μm), swirling flow is induced with approximately 100 μm/s. On the other hand, for higher case ($h$ = 100 μm), a higher velocity magnitude with 250 μm/s was generated.
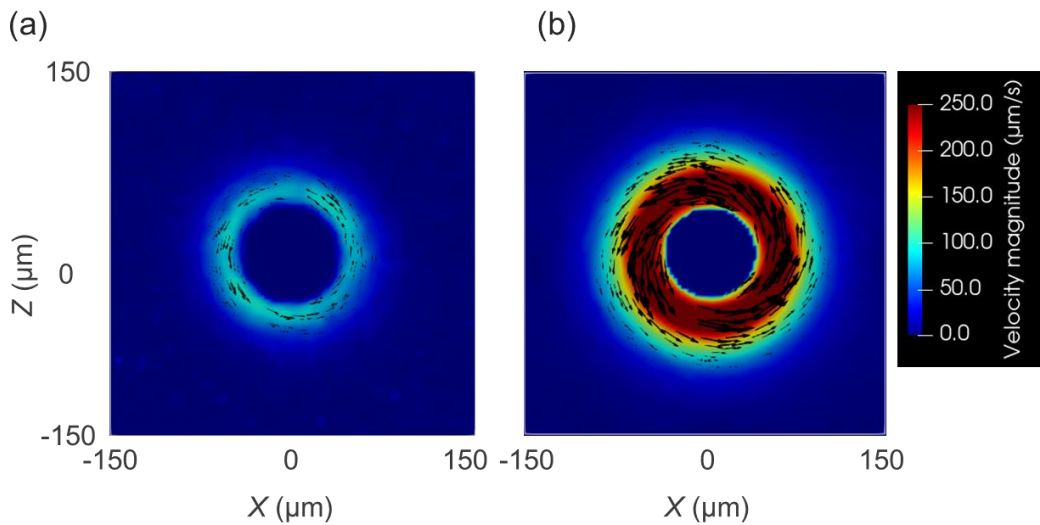


Fig. 2-15 2D vector plots of the average velocity around a pillar obtained via PIV measurements. The geometric condition is set to (a) $h$ = 50 μm and (b) $h$ = 100 μm for $S$ = 400 μm. The vibration conditions were $f$ = 600 Hz and $A$ = 2 μm.

Fig. 2-16 represents the peak velocity magnitude for various vibration frequencies and amplitudes in pillar height of $h$ = 50 and 100 μm. For the frequency dependence with constant $A$ = 2 μm (Fig. 2-16 (a)), velocity magnitude increased as vibration frequency increased almost linearly. Higher pillar height generated higher velocity magnitude in the same vibration condition, the velocity doubled at a frequency of 800 Hz. For the amplitude dependence with constant $f$ = 200 Hz (Fig. 2-16 (b)), velocity magnitude increased as amplitude increased similarly to frequency dependence. The increase in velocity with amplitude dependence was greater for the $h$ = 100 μm condition compared to the $h$ = 50 μm condition, the velocity of the $h$ = 100 μm condition was six times greater than that of the $h$ = 50 μm condition at an $A$ = 9 μm. These results indicate that the pillar height (i.e., height of the region) significantly influences the flow field.
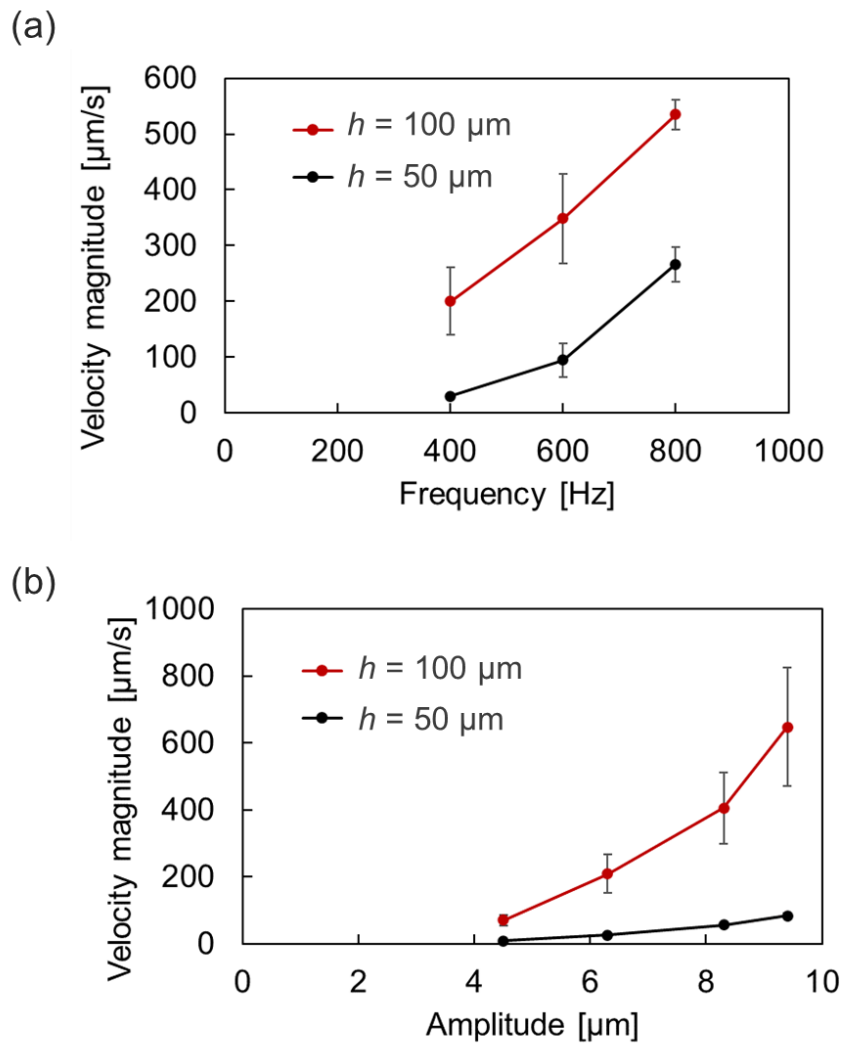
Fig. 2-16 Peak velocity magnitude around the cylindrical pillar (a) frequency dependence with constant $A = 2$ µm and (b) amplitude dependence with constant $f = 200$ Hz. Error bars indicate the standard deviation from triplicate experiments.

### 2.3.4. Effect of the pillar arrangement

Next, we investigated the effect of pillar arrangement including pillar separation and array type. Specifically, we used a square array for separation $S$ =200, 400, 600 μm and a hexagonal array for $S$ = 400 μm. Pillar height was set to $h$ = 100 μm. Fig. 2-17 shows 2D streamline and vector plots of the velocity around a pillar in different pillar distance cases. The vibration condition was set to $f$ = 600 Hz, $A$ = 2 μm. For streamline in $S$ = 200 μm condition (left panel of Fig. 2-15 (a)), small vortices appeared at the centers of four pillars in association with the flow revolving around each pillar. Similarly, in the vector plots (right panel of Fig. 2-15 (a)), flow circulating the pillars was observed, with the shape being close to a square. Additionally, regions of reduced velocity were observed at the top, bottom, left, and right sides, which is believed to be the result of interference with adjacent pillars. In the case of $S$ = 400 μm (Fig. 2-15 (b)), the flow circulating the pillars occurred. In the vector plots, low-velocity regions with velocities close to 0 μm/s were observed outside the localized rotational flow around the pillars. Under $S$ = 600 μm (Fig. 2-15 (c)), a local flow with no interference was observed. The interference with adjacent pillars decreased further, and the low-velocity regions expanded compared to the $S$ = 400 μm condition. In the hexagonal array condition under $S$ = 400 μm (Fig. 2-15 (d)), circular flow was induced around the pillar, and localized vortices were generated at spaces between adjacent three pillars. Similarly to square array $S$ = 400 μm condition for vector plots, low-velocity is induced at space between adjacent pillars.

Fig. 2-18 shows the peak velocity magnitude in various pillar separations. We found that the velocity slightly increased as the spacing between the pillars got wider. In both square and hexagonal array cases, no considerable difference in velocity was observed under identical vibration and separation conditions.

28
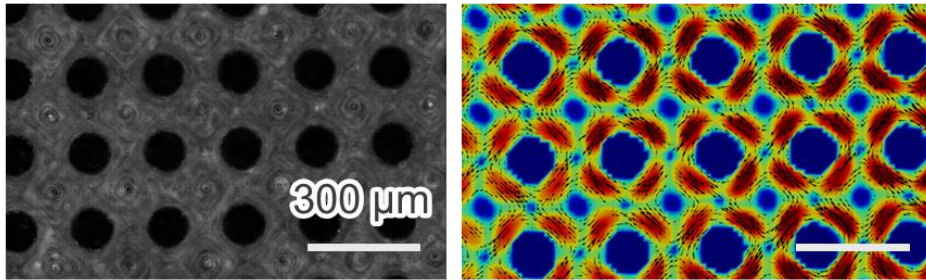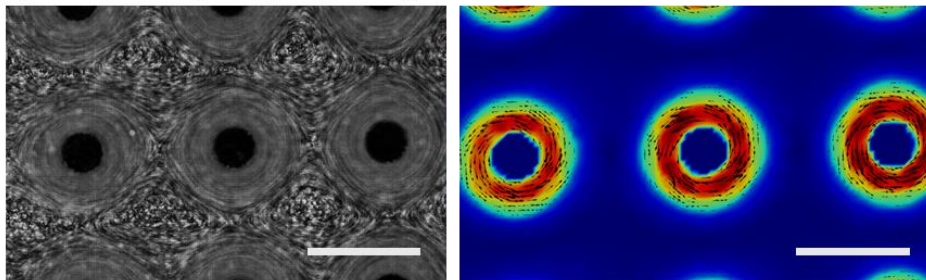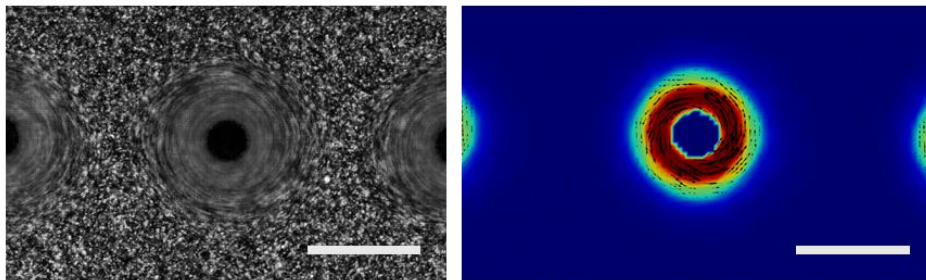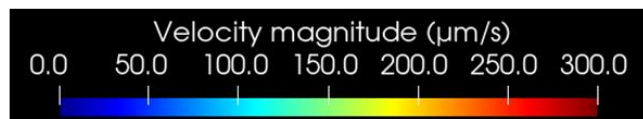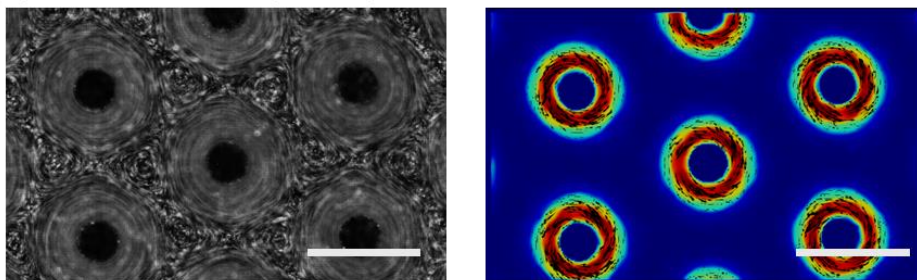
Fig. 2-17 Flow field around the cylindrical pillar with $S =$ (a) 200 μm, (b) 400 μm, and (c) 600 μm for square array, and (d) $S =$ 400 μm for hexagonal array. (left side) Streamlines of the velocity field around the cylindrical micropillar. (right side) 2D vector plot of the velocity around a pillar obtained with PIV measurement.
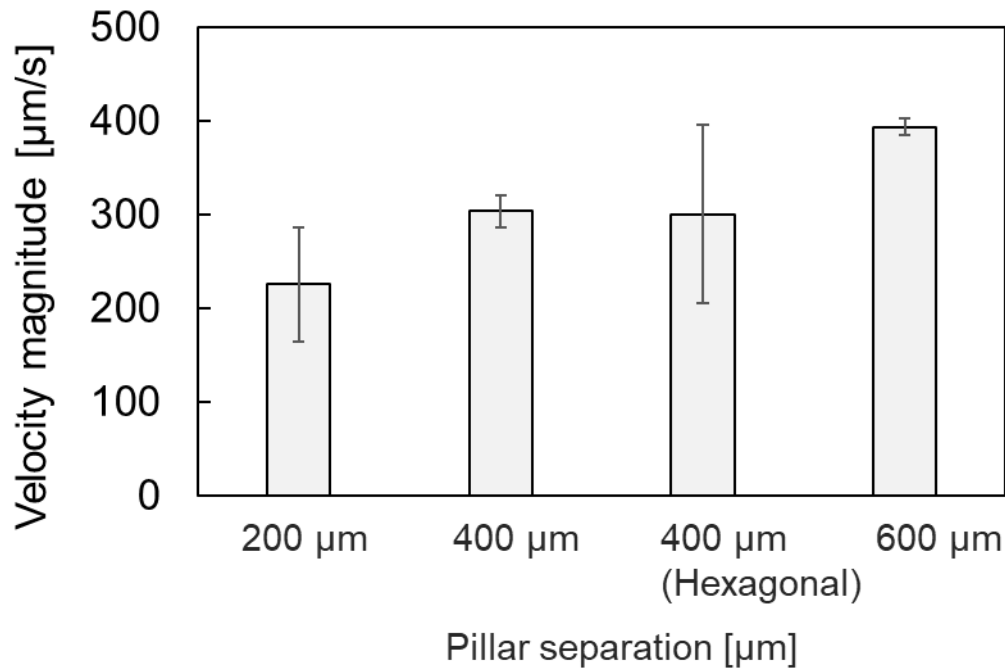
Fig. 2-18 Peak velocity magnitudes around the cylindrical pillar at various pillar separations. Error bars indicate the standard deviation from triplicate experiments. The vibration condition was set to $f$ = 600 Hz and $A$ = 2 μm.

### 2.3.5. Flow field with rectilinear vibration

Next, we investigated flow fields around the pillar subjected to rectilinear vibration which is traditionally investigated (Lutz et al. 2005, 2006; House et al. 2014; Hayakawa et al. 2018). The vibration condition was set to $S$ = 400 μm, $h$ = 100 μm, $f$ = 600 Hz, and $A$ = 3.3 μm.

For streamline (Fig. 2-19 (a)), four vortices manifested themselves around the pillar at a 45-degree offset from the vibration axis under the rectilinear vibration along the $x$-axis, mirroring findings from prior investigations. Moreover, influx and ejection flows were induced in the horizontal and vertical directions relative to the vibration axis, respectively. Within the high-velocity region, the velocity magnitude measures approximately 100 μm/s, which is eight times smaller than that of circular vibration in identical vibration condition. This result indicates that the circular vibration is more efficient in terms of inducing a net flow with a smaller vibration amplitude. Finally, we investigated the dependence of vibration frequency and amplitude on velocity magnitude subjected to rectilinear vibration. Similarly to the cylindrical case, velocity magnitude increased as frequency and amplitude increased.

(a) Streamline
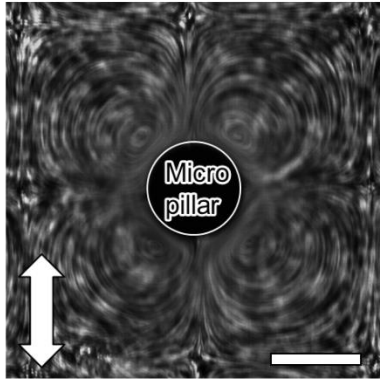
(b) PIV measurement

Scale bar = 100 μm
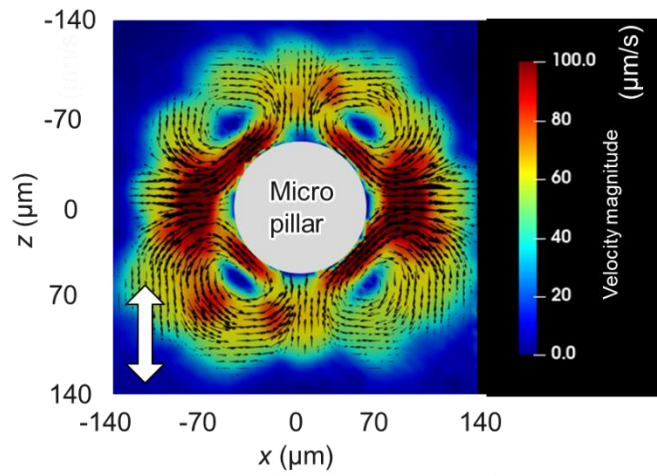
(c)
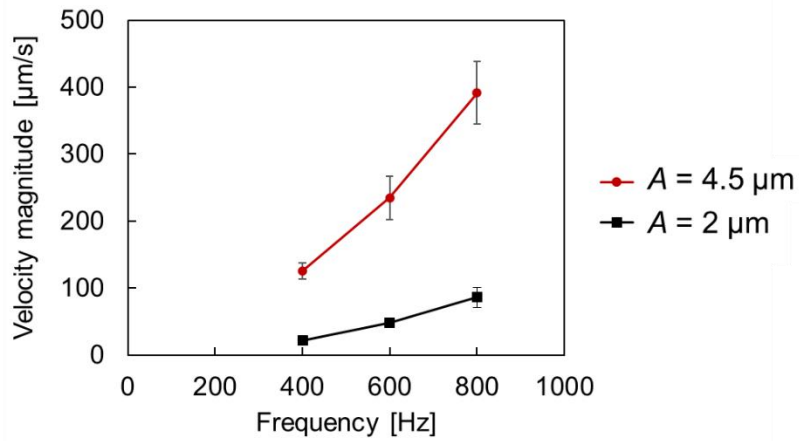
Fig. 2-19 Flow field around the cylindrical pillar subjected to rectilinear vibration in (a) the streamline and (b) the PIV measurement. (c) the peak velocity magnitude around the pillar. Error bars indicate the standard deviation from triplicate experiments.

## 2.4. Effect of stokes layer thickness

From the above measurement results, we observed that both pillar height and separation influenced the flow field. The characteristics of the flow field around the oscillating microstructure can be elucidated by the theory of the stokes layer thickness, which is formed by the oscillating wall. In general, there is a viscosity-related influence near the solid plate on the net motion of particles. This influence diminishes as the distance from the plate increases (Fig. 2-20 (a)). Consequently, the influence of viscosity is more pronounced near the pillar sidewall and the top/bottom plate, making it challenging for a net particle motion to occur in those regions. Conversely, particle motion becomes more active as the distance from the plate increases.

For our system, we observed that under conditions with higher pillar height (fluid layer thickness), higher velocities were induced (Fig. 2-15). The increase in velocity with higher pillars is attributed to the reduced influence of viscosity from the top and bottom walls, leading to a more pronounced net particle motion (Fig. 2-21 (a)). Regarding the effect of the stokes layer in the horizontal direction from the pillar sidewall, the peak position is located approximately 13 μm away from the pillar sidewall in the radial profiles of the azimuthal velocity, and the distribution subsequently decays (Fig. 2-13 (c)). This is believed to be due to the influence of viscosity from the pillar sidewall (Fig. 2-21 (b)). Near the sidewalls of the pillars, the viscous effects of pillars exhibiting periodic oscillations lead to a small net particle motion. As particles move away from the walls, an increased net particle motion and a higher peak velocity are induced. However, at positions further away, it is presumed that the velocity distribution attenuates due to the reduced influence of pillar oscillation effects. From these results, it is inferred that parameters such as pillar shape and pillar height affect the flow field.
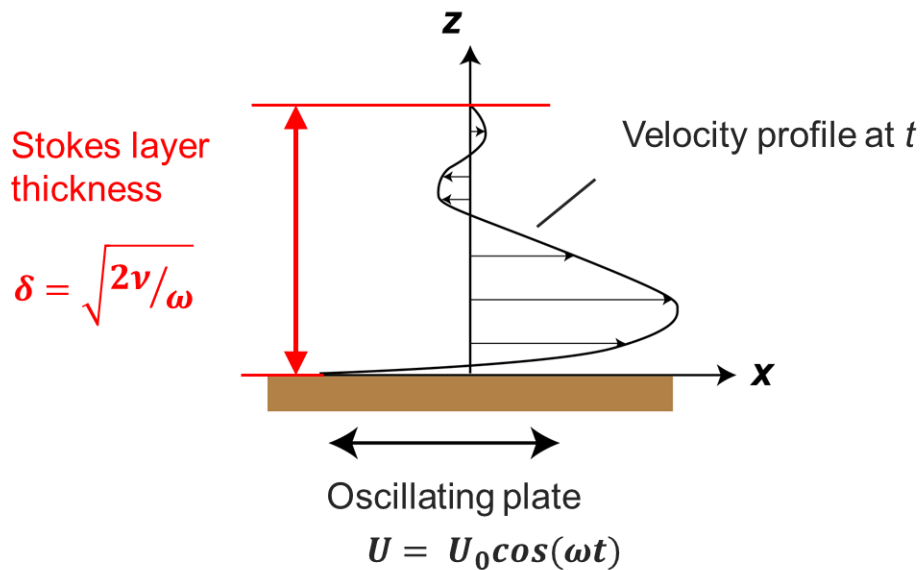


Fig. 2-20 (a) Schematics of velocity distribution on an oscillating plate.
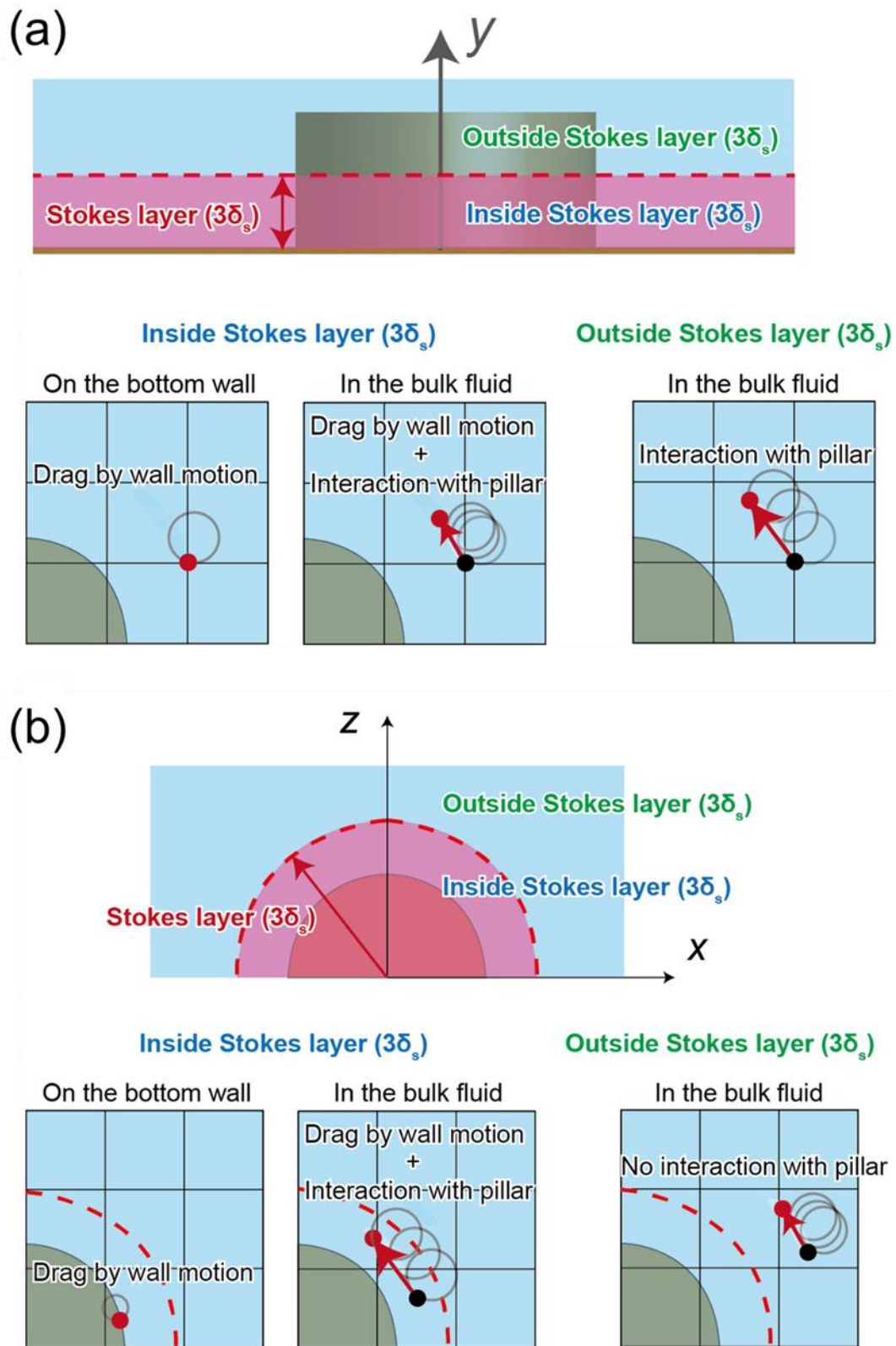
Fig. 2-21 Formation of stokes layer from oscillating bottom substrate. (b) Formation of stokes layer from a side wall of oscillating cylindrical pillar.

## 2.5. Summary of Chapter 2

In this chapter, we conducted an initial exploration of the flow fields induced around the pillar subjected to vibration before proceeding with NP detection experiments. Initially, we fabricated a micropillar substrate with a micro-fabrication process. Cylindrical pillar patterns with varying arrangements and heights were readily created via the DRIE technique. Flow fields under various vibration conditions were measured using the PIV technique.

Upon applying circular vibration, we observed a rotational flow around the cylindrical pillar. In addition, the induced velocity varied with the frequency and amplitude of the vibration. For pillar separation, the interference between adjacent pillars changed according to the separation between pillars. When the pillar height got higher, the induced velocity also increased. The characteristics of the velocity profile and the flow fields related to pillar height can be explained by the theory of the stokes layer. For vibration patterns, we investigated the flow field induced with rectilinear vibration. Similarly to previous studies, four vortices were formed around the pillar in the case of single-axis oscillation (Lutz et al. 2005, 2006; House et al. 2014; Hayakawa et al. 2018). Tuning vibration conditions within the range of circular vibration did not alter the overall flow field so much. However, merely changing the vibration direction led to a drastic alteration of the flow around the cylindrical pillar. Even under the same vibration conditions, the induced velocity was smaller in circular vibration compared to rectilinear vibration. This suggests that circular oscillation is more suitable for generating higher velocities.

The results of this chapter experimentally demonstrate that flow fields can be readily controlled by tuning conditions related to pillar geometry and vibration pattern.

# Chapter 3.

# Detection of nanoparticles using the VIF-induced aggregation
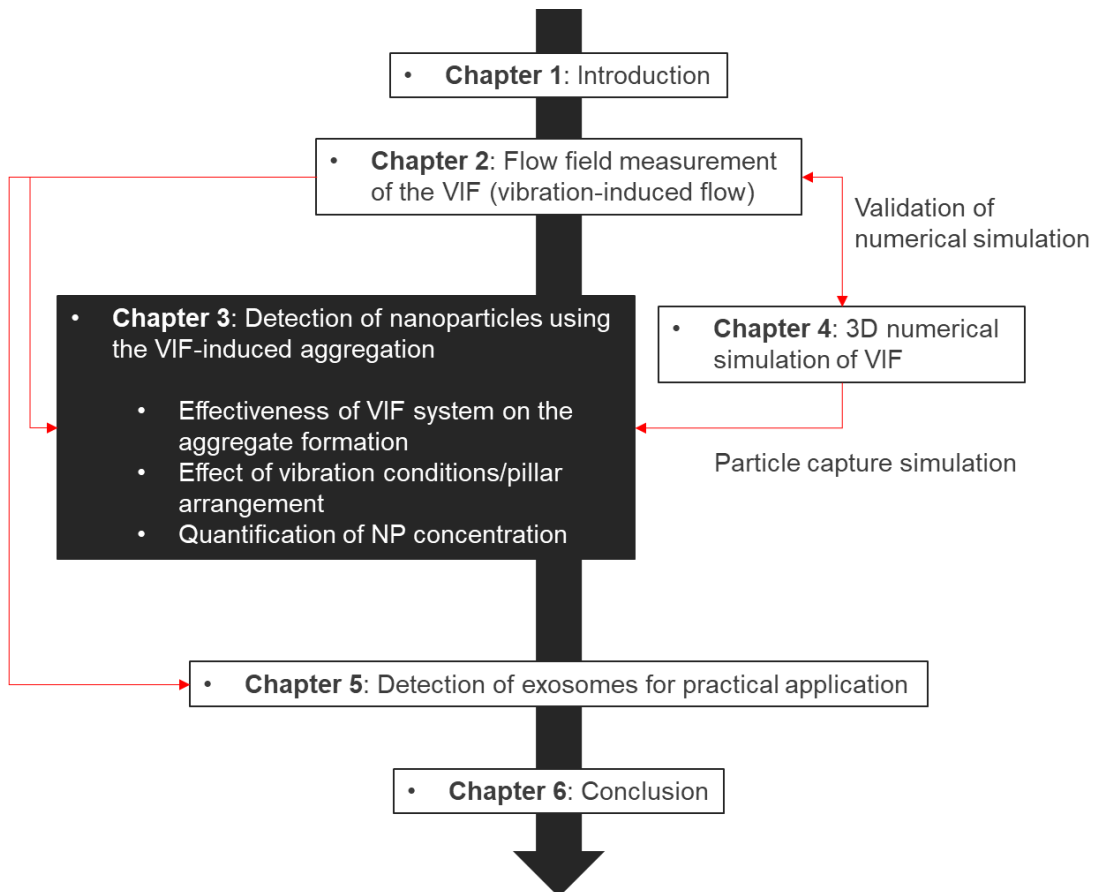
## 3.1. Overview

In this chapter, we employed the VIF to agitate the sample fluid containing the target NPs and selectively CPs with specific affinity. The conceptual diagram is presented in Fig. 1-8. In the initial stage, both particles are dispersed within the microfluidic space. Employing circular vibrations across the entire substrate induces a localized swirling flow around the pillars, effectively stirring the NPs and CPs. Throughout this process, the NPs adhere to the surface of the CPs with high affinity. As the adsorption of NPs advances, the CPs aggregate upon collision, with the NPs serving as binding agents. The concentration of NPs in the sample can be estimated by assessing the extent of aggregation of the CPs. To simplify NPs detection, we quantitatively evaluated the aggregation area through the analysis of bright field images captured using a standard microscope. In practice, we adopted the avidin-biotin interaction with specific affinity as a model-capturing system to induce aggregation of polystyrene CPs. Micrometer-sized CPs used in our study are relatively larger than the latex particles commonly used in immunoagglutination, making aggregation by diffusion impractical. Therefore, we aimed to investigate the effect of VIF stirring on CPs aggregate.

In the previous chapter (chapter 2), we investigated the characteristics of VIF through flow field measurements using micro-PIV. We observed that the flow field depended on parameters such as vibration frequency/amplitude and pillar geometry. In this chapter, we examined the effects of such parameters on aggregate formation. This demonstration allowed us to assess how the physical parameters of vibration influence the detection of NPs. For the pillar geometric arrangement parameter, we considered both smaller ($h$ = 50 μm/$S$ = 200 μm) and larger cases ($h$ = 100 μm/$S$ = 400 μm), respectively. Regarding vibration patterns, we adopted circular vibration, characterized by a lower number of vortices induced around the pillar, making the flow pattern manageable.

## 3.2. Experimental procedures

### 3.2.1. Aggregation test with model capturing system of NPs and capture particles (CPs)

We introduced avidin-biotin pair affinity interaction as a model of NPs capture system. Avidin has a very high specific affinity for up to four biotin molecules ($K_d$ < $10^{-15}$ M) and is stable and functional over a wide range of pH and temperature. In practice, commercial avidin-coated polystyrene microparticles (Spherotech Inc., VP-30-5, diameter: 3 μm) and biotin-coated nanoparticles (Spherotech Inc., TFP-00852-5, diameter: 0.15 μm) (diameter measured using an imaging analyzer was 152 ± 55 nm; Fig. 3-1) were employed as representative models for capture beads and target NPs, respectively.
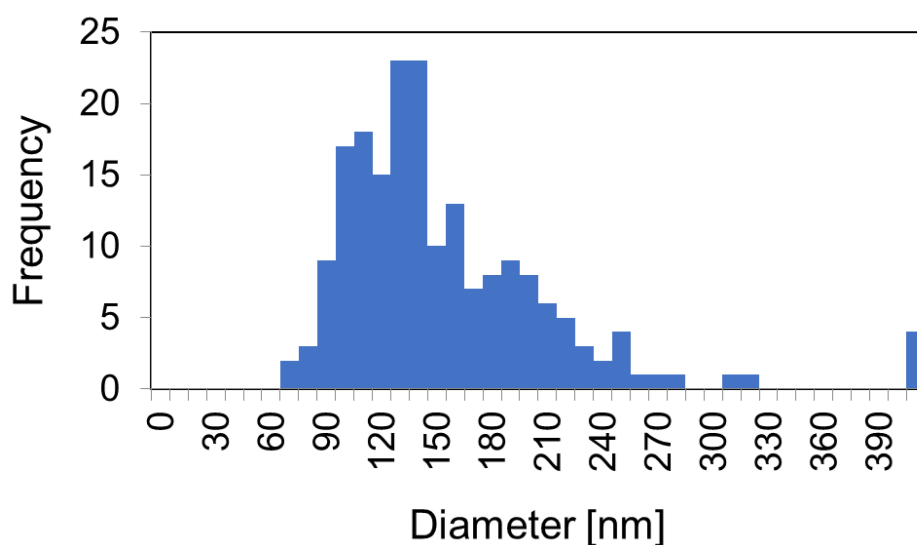
Fig. 3-1 Size distribution of biotin-coated nanoparticles measured using an imaging analyzer.

### 3.2.2. Experimental procedures

Both surfaces of the PDMS substrate and cover glass were treated with a blocking buffer (5% BSA w/w in 1× PBS) to prevent nonspecific adsorption of particles and entrapment of air bubbles in the application of this mixture. After the coated incubation for 15 min, the surfaces were dried. The mixture containing NPs and CPs was gently pipetted 10 times to ensure uniform dispersion within the microtube. Subsequently, five microliters of this mixture were applied to the center of the substrate and covered with a cover glass (Fig. 3 2).
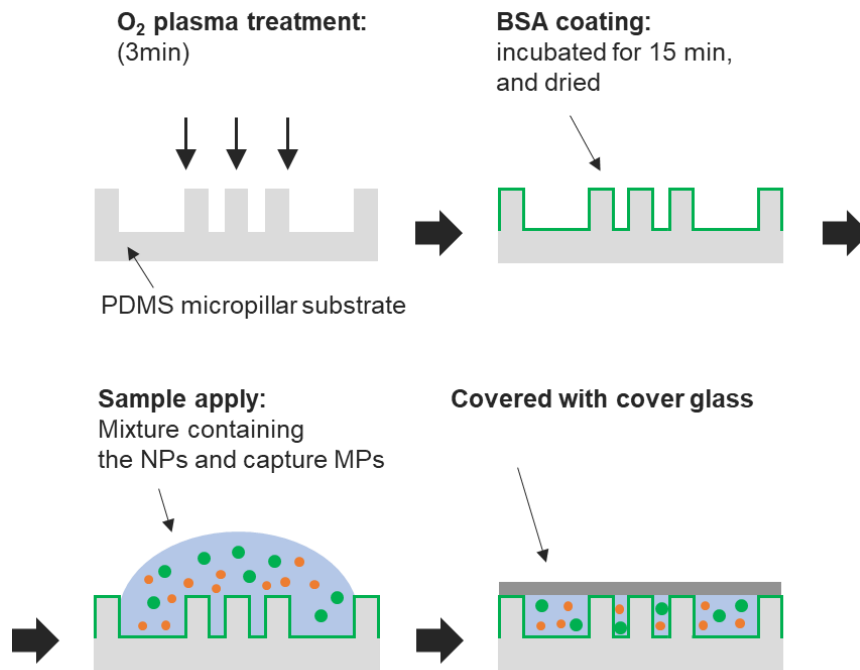
Fig. 3-2 Schematic illustration of application of sample including NPs and CPs to the substrate.

The assembly of PDMS substrate and cover glass including the mixture was fixed to an XY piezo-drive stage using small pieces of double-sided tape. To generate circular vibration, sinusoidal wave signals with a 90° phase offset were applied to the piezo stage through a waveform generator connected to an amplifier. For capturing the images in a bright field, a digital microscope camera (Axiocam 503 mono, ZEISS, Germany) was employed in conjunction with an upright microscope (Axio Scope A1, ZEISS, Germany). For the observation, two types of objective lenses were used, a high-magnification lens (A-Plan 10x Objective Lens, ZEISS, Germany) and a low-magnification lens (A-Plan 5x Objective Lens, ZEISS, Germany), to cover a wide range with the microscope. Spatial resolutions for these two lenses were determined as 0.52 and 2 µm², calculated using conversion factors of 0.72 and 1.44 µm/pix, respectively.

### 3.2.3. Image analysis of the CPs aggregates

The extent of CPs aggregation was assessed by analyzing the average areas of CPs aggregates. For the simplicity of the detection system, only bright-field images were acquired using a basic optical microscope. After capturing the image, analysis was performed using ImageJ software through image binarization and standard particle analysis (Fig. 3-3). In practice, several parameters were configured for image analysis, including the binarization thresholds of intensity for all aggregates

($Th_{agg}$) and pillars ($Th_{pillar}$). Additionally, binarization thresholds for the size of aggregates ($I_{agg-max}$ and $I_{agg-min}$) and pillars ($I_{pillar-min}$) were set.

In this image analysis, the areas where the pillars existed were excluded from the image analysis after the masking process of binarized images. Initially, all detected substances within the intensity thresholds for aggregates ($Th_{agg}$, $I_{agg-max}$, and $I_{agg-min}$) were identified as aggregates through binarization. Subsequently, performing binarization of the original image with thresholds for pillars, pillars were identified as null. By multiplying the two obtained images, only the aggregated were recognized within the binarized image, eliminating the null pillar. After excluding data corresponding to several particles, the average area of CPs was obtained by dividing the total aggregate area by the number of aggregates.

### 3.2.4. Quantification of NPs concentration

As described earlier, detection and quantification were performed based on the extent of CP aggregate formation. In this context, the slope of the increasing average area of aggregates was utilized to construct a calibration curve. This choice was made due to the absence of a clear and reproducible plateau in most cases, even with extended mixing times (approximately 40 minutes). The evaluation of detection performance included parameters such as the limit of detection (LOD), sensitivity, resolution, and the coefficient of determination ($R^2$) value of the calibration curve.
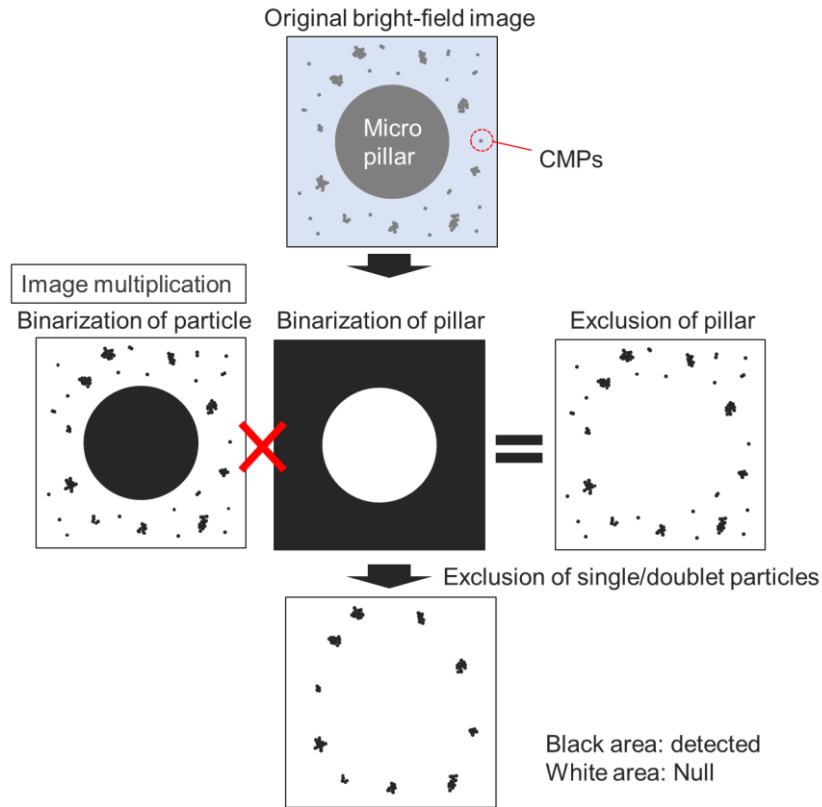
Fig. 3-3 Flow chart of image analysis to evaluate the area of CPs aggregates.

## 3.3. Estimation of CPs/NP diffusion and binding capacity

### 3.3.1. Diffusion of CPs/NPs

In an environment of steady laminar flow, substances move along the streamlines of the flow, except for molecular diffusion. Here, in a microfluidic system, which typically involves very small length scales in space, there arises a question of whether convection, driven solely by the diffusion phenomenon, is sufficient to complete mixing. The answer to this question can be elucidated by estimating the diffusion coefficient ($D_{dif}$) of the substances in the fluid and the associated time scale for mixing, as demonstrated (Kastelowitz and Yin 2014). The diffusion coefficient ($D_{dif}$) can be expressed using the following equation.

$$D_{dif} = \frac{k_B T}{3\pi\mu d} \tag{3-1}$$

where $k_B$, T, $\mu$, $d$, represent boltzmann constant, temperature, viscosity, and diameter of substance. From the above equation, the diffusion coefficients for the CPs and NP in our experimental system were calculated to be $D_{CP} = 0.07\ \mu m^2/s$ and $D_{NP} = 2.87\ \mu m^2/s$, respectively.

Using the diffusion coefficients obtained above, we can determine the time scale for mixing that occurs solely due to diffusion. The relationship between the distance over which substances move via diffusion and the corresponding time scale can be expressed as

$$x = \sqrt{2Dt} \tag{3-2}$$

where $x$ and $t$ represent the distance over which substances move due to diffusion and the associated time scale. According to this equation, it would take approximately 1200 min and 30 min for CPs and NP to advance 100 $\mu$m solely through diffusion, respectively. These time intervals are unacceptably long, highlighting the necessity for a mixing system. From these calculations, the influence of the diffusion coefficients of both CPs and NPs do not influence the mixture due to their relatively small values.

### 3.3.2. Binding capacity of NPs on single CP

In addition, the capacity of how many NPs can bind to a single CP was calculated. We assumed that NPs densely surrounded the CP without gaps. Considering a binding site of sphere shape with a diameter equal to the sum of the CP diameter and the NP radius (Fig. 3-4), the surface area of the binding site sphere ($A_c$) and the NP cross-sectional area ($A_s$) can be determined as follows:

$$A_c = \pi \times (d_c + r_s)^2 \tag{3-3}$$

$$A_s = n \times \pi \times \left(\frac{d_s}{4}\right)^2 \tag{3-4}$$

where $d_c$, $d_s$, $r_s$, and $n$ represent CP diameter, NP diameter, NP radius, and number of binding NPs, respectively. When binding occurs without gaps, the two areas are equal. Substituting the CP diameter and NP radius used in our experiment yields $n = 1764$ (Table 3-1).
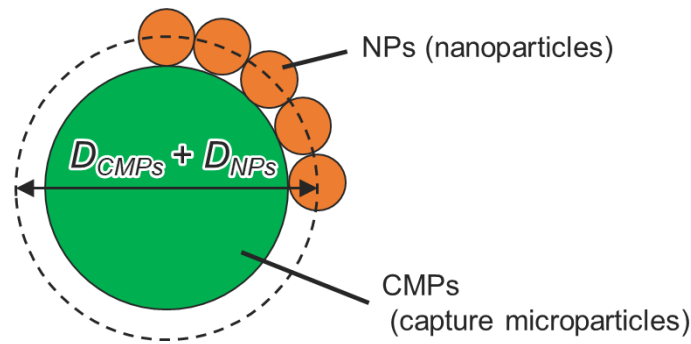


Fig. 3-4 Binding of NPs around single CP.

Table 3-1 Maximum number of NPs attached to single CPs.

| CMPs diameter | NPs diameter | Maximum number of NPs attached to single CMPs |
|---|---|---|
| 3 μm | 0.15 μm | 1764 |

Additionally, we estimated the relationship between number of CPs and NPs. In our major experimental condition, the concentration of CP and NP is represented as $N_c = 3.4 \times 10^7$ /mL and $N_s = 5.7 \times 10^9$ /mL. Here, the ratio of the number of NP to CP is $R_N = N_s/N_c = 178$ (Table 3-2). The volume of the surrounding liquid that each CP occupies can be calculated as $V_c = 10^9/N_c = 0.3$ μL (a cube with a side length of 30 μm). Therefore, when each type of particle is uniformly dispersed in the mixture, it implies that within a cubic space with a side length of 72 μm, there are 178 NPs distributed around a single CP. Considering the estimated diffusion timescale for the small beads from the previous section, it is reasonable to assume that particles in this space are not in contact for a duration, primarily transported solely through diffusion.

Table 3-2 Ratio of number of NPs and CPs in each NPs concentration. In this thesis, a pair of concentrations highlighted in the red square was predominantly used.

| CMPs concentration [/mL] | NPs concentration [/mL] | Ratio of number of NPs/CPMs |
|---|---|---|
| $3.17 \times 10^7$ | $5.7 \times 10^{10}$ | 1782.5 |
| ↑ | $1.1 \times 10^{10}$ | 356.5 |
| ↑ | $5.7 \times 10^9$ | 178.3 |
| ↑ | $1.1 \times 10^9$ | 35.7 |
| ↑ | $5.7 \times 10^8$ | 17.8 |
| ↑ | $1.1 \times 10^8$ | 3.6 |
| ↑ | $5.7 \times 10^7$ | 1.8 |

## 3.4. Results and discussion

### 3.4.1. Effectiveness of VIF system on the aggregate formation

We experimentally validate the effect of the VIF system on CPs aggregation formation. First, we preliminary investigated aggregate formation test using vortex mixing in a microtube at 500 rpm instead of VIF. We used a sample mixture containing NPs and polystyrene CPs concentrations of 5.7 × $10^9$ /ml and 3.0 × $10^7$ /ml, respectively. Upon microscopic observation, CPs aggregates were not induced even after 1 h mixing (Fig. 3-5). We expect that vortices in a microtube are large in the vortex mixing, meaning NPs and CPs tend to move in parallel so that efficient collision does not occur.
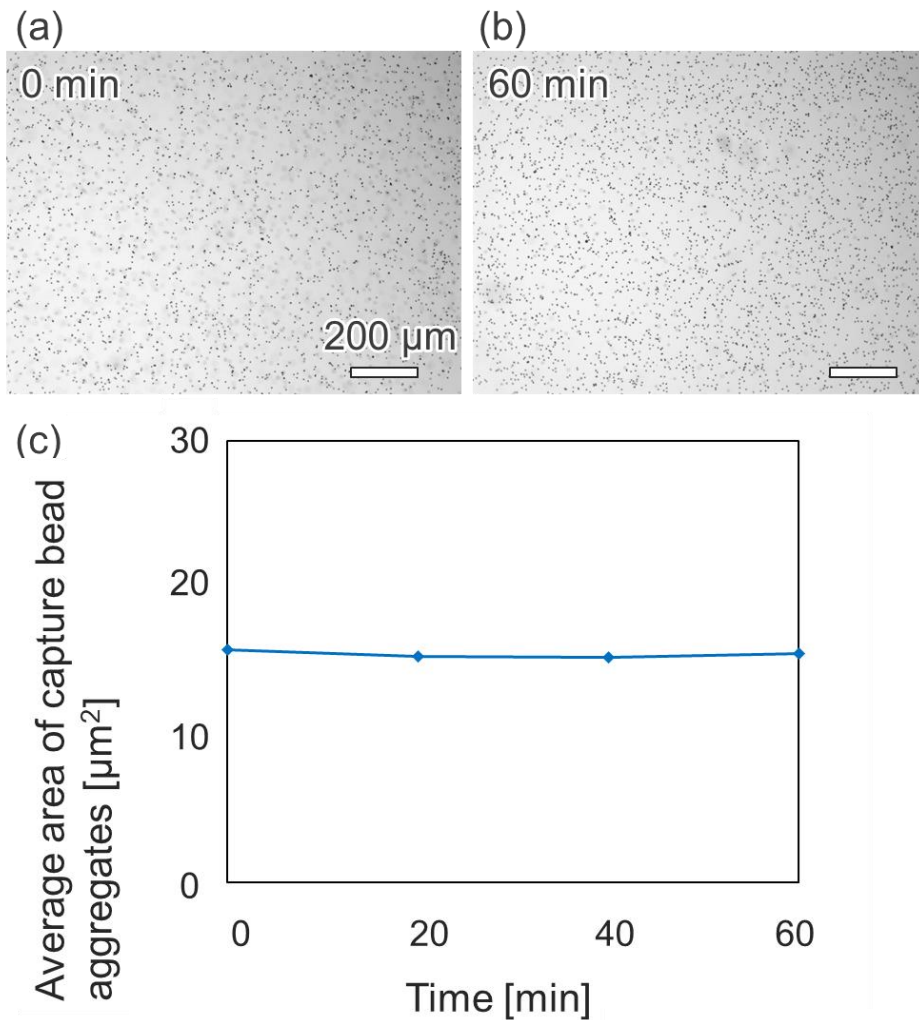


Fig. 3-5 Microscopic bright images of particles taken at (a) 0 min and (b) 60 min of vortex mixing, with concentrations of NP and CP were 5.7 × $10^9$ /mL and 3.0 × $10^7$ /mL, respectively. (c) Time evolution of the average area of CP aggregates in the mixture during vortex mixing. The stirring condition for vortex mixing was set to 500 rpm.

Subsequently, we performed the same microscopic observations in the condition of VIF stirring. Fig. 3-6 shows bright-field microscopic images of the particles on the micropillar substrate. The vibration condition was set to circular vibrations with a frequency $f = 500$ Hz, amplitude $A = 3.3$ μm. The condition of pillar geometry was set to $h = 50$ μm and $S = 200$ μm. At the initial time point (0 min; before the application of vibrations), CPs were uniformly dispersed in the observed field under all conditions, although NPs can not be observed due to their smaller size. This suggests that pre-mixing in a microtube via pipetting did not induce aggregation of CPs. In the case of the mixture containing both NPs and CPs, several relatively large aggregates of CPs (above 25 μm in diameter in the image) were induced upon 15 min vibration (Fig. 3-6 (a), lower panels). Additionally, control experiments were performed without VIF and NPs. Under the condition of VIF absence, no aggregation of capture CPs was detected (Fig. 3-6 (b), lower panels). This result indicates that Brownian diffusion is inadequate to promote collision and aggregation of CPs. In the case of the absence of NPs, relatively small aggregates (diameter less than 10 μm) were induced (Fig. 3-6 (c), lower panels). This result could be attributed to some intermolecular forces between the polystyrene CPs, leading to nonspecific adsorption. Nonetheless, the average area of the aggregate was smaller compared to the experiment where NPs were present in the sample. Hence, we hypothesize that vortices generated by local flow in the VIF contribute to the effective formation of aggregates of affinity CPs, in contrast to the conventional vortex mixing shown in Fig. 3-5, which is commonly utilized in commercial kits for NP detection employing CPs.

This initial series of experiments suggests that effective aggregation of CPs occurred only in the presence of an affinity between the target NPs and the CPs, within the VIF stirring. This observed phenomenon holds potential for NP detection. More precisely, it is suggested that microscale local swirling flow facilitated the collision between capture CPs and NPs. Subsequently, CPs aggregates encountered each other at the interference of neighboring vortices, resulting in the formation of larger aggregates.

Fig. 3-6 (a–c) Microscopic bright images of particles on the substrate with micropillars taken at 0 min and 15 min after application of the VIF. (a) VIF(+), NP(+), (b) VIF(−), NP(+), (c) VIF(+), NP(−). The conditions of circular vibrations in all cases were: $f$ = 500 Hz, and $A$ = 3.3 μm. Pillar geometry was set to $h$ = 50 μm and $S$ = 200 µm.

### 3.4.2. Effect of vibration conditions

We investigate the effect of vibration conditions, especially vibration frequency and amplitude, on aggregate formation. Here, we adopted two kinds of pillar geometry with smaller ($h$ = 50 μm/$S$ = 200 μm) and larger ($h$ = 100 μm/$S$ = 400 μm) cases. We analyzed the dependence of the extent of aggregation and flow fields which is obtained in Fig. 2-14 in chapter 2. Especially, the effect of vibration frequency and amplitude was investigated. The concentrations of NPs and CPs were 5.7 $\times 10^9$ /ml and 3.0 $\times 10^7$ /ml, respectively. Fig. 3-7 shows representative microscopic bright images of particles on the substrate with micropillars at 15 min after application of the VIF in various vibration conditions. For $f$ = 500 Hz and $A$ = 1.5 μm condition (Fig. 3-7 (a)), small aggregates formed around the pillars. With an increase in amplitude (Fig. 3-7 (b, c)), the size of the generated aggregates became larger. However, under high-frequency conditions, specifically at $f$ = 1000 Hz and $A$ = 3.3 μm condition (Fig. 3-7 (d)), the aggregates were smaller.
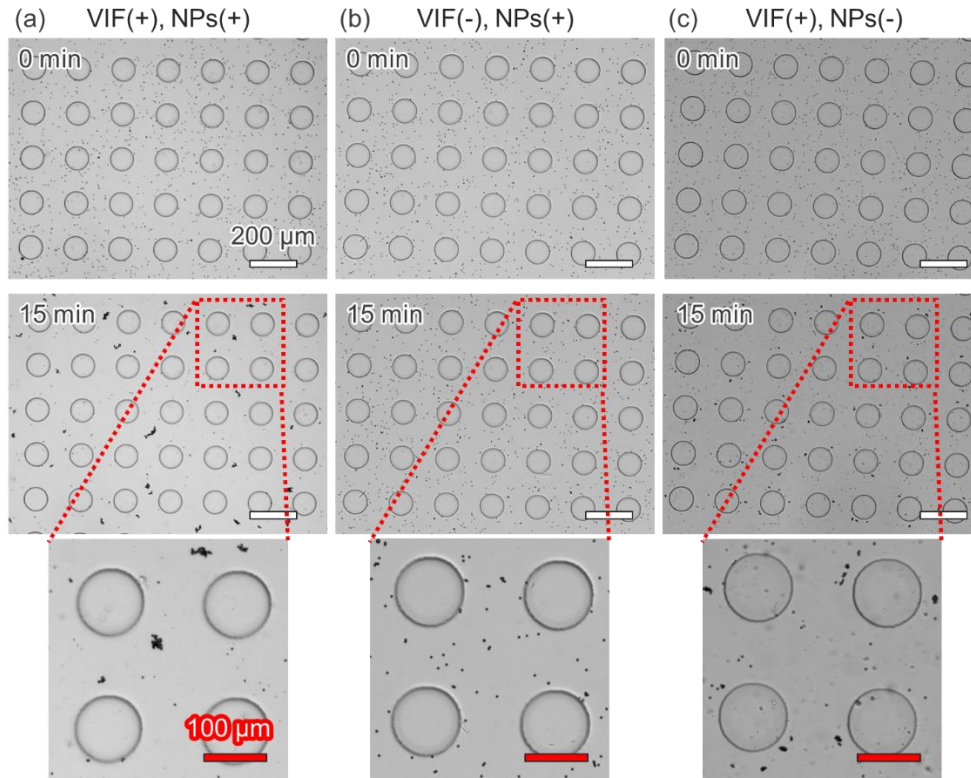
Fig. 3-7 Microscopic bright images of particles on the substrate with micropillars taken at 15 min after application of the VIF in various vibration conditions. Pillar geometry in all cases was: $h = 50$ μm and $S = 200$ μm. The conditions of circular vibrations were (a) $f = 500$ Hz, and $A = 1.5$ μm, (b) $f = 500$ Hz, and $A = 3.3$ μm, (c) $f = 500$ Hz, and $A = 5.2$ μm, and (d) $f = 1000$ Hz, and $A = 3.3$ μm. Pillar geometry was set to $h = 50$ μm and $S = 200$ μm.

Fig. 3-8 illustrates the average area of aggregates for each vibration parameter. Regarding amplitude dependence, the aggregate area increased with the amplitude. On the other hand, as the aggregate area increased, the error bars also grew. As for frequency dependence, peaks were observed at frequencies of 500 Hz and 800 Hz, whereas the aggregate area decreased at 1000 Hz.

The average area of aggregates demonstrated an increase in the velocity magnitude within the range below 300 μm/s. In this interval, higher induced velocities corresponded to a higher likelihood of CP collision, leading to aggregate growth. However, at velocities exceeding 300 μm/s, the aggregate size decreased. This outcome suggests that shear stress acted on the CP aggregates, causing them to break and resulting in smaller aggregates. Although the most significant aggregate formation occurred under the conditions of f = 500 Hz and A = 5.2 μm, there was notable variability among triplicate experiments. Consequently, we opted for the conditions f = 500 Hz and A = 3.3 μm in subsequent experiments due to the observed reduced variability

The average area of aggregates increased with velocity magnitude in the range below 300 μm/s. In this region, the higher the induced velocity, the more likely it is that the collision of CPs proceeds such that aggregates grow. However, at velocities above 300 μm/s, the aggregate size decreased. This result indicates that shear stress acted on the CP aggregates and caused them to break, resulting in smaller aggregates. Although the largest aggregate formation was obtained at condition $f$ = 500 Hz and $A$ = 5.2 μm, the variability among triplicated experiments was relatively large. Thus, we employed the condition $f$ = 500 Hz and $A$ = 3.3 μm, which exhibited the smallest variability, in the following experiments.
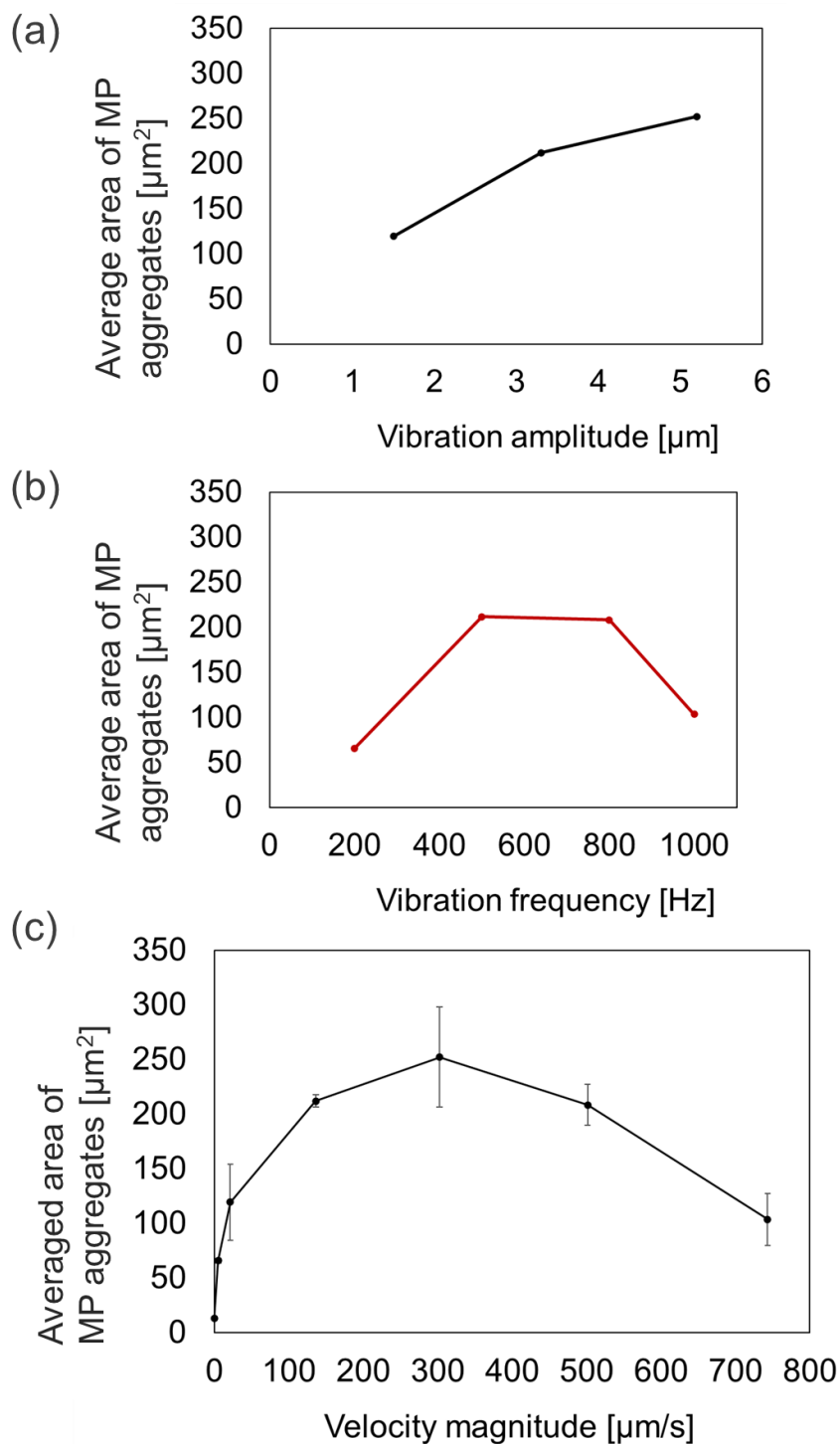
Fig. 3-8 The average area of CP aggregates in bright-field images under various vibration conditions: (a) dependence on the vibration amplitude and (b) the vibration frequency. (c) Relationship between the magnitude of the velocity and the average area of CP aggregates after 15 min. Error bars indicate the standard deviation from triplicate experiments. Pillar geometry was set to $h = 50$ μm and $S = 200$ μm.

Next, we examined the influence of vibration conditions on aggregate formation under the condition $h = 100$ μm and $S = 400$ μm. Fig. 3-9 shows microscopic bright images of particles on the substrate with micropillars captured at 10 min after application of the VIF. For higher frequency with $f = 800$ Hz and $A = 2$ μm compared to $f = 600$ Hz (Fig. 3-11 (b)), aggregate size got larger, and the aggregate sizes were relatively uniform, with one forming around each pillar. In cases of larger vibration amplitudes, smaller aggregates were formed. Increasing the amplitude resulted in the formation of relatively larger aggregates with size variations, particularly at $f = 200$ Hz with either $A = 8$ μm or $A = 9$ μm.

Fig. 3-10 illustrates the quantitative examination of the dependence of aggregate area on vibration frequency and amplitude. The aggregate area increased with the augmentation of both frequency and amplitude. Fig. 3-10 (b) depicts the dependency of aggregate area on velocity. For frequency dependency, we set $f = 400, 600, 800$ Hz with a constant amplitude $A = 2$ μm. Regarding amplitude dependency, we set $A = 6.2, 7.8, 9.7$ μm with a constant frequency of $f = 200$ Hz. Even within the same velocity range, there was a tendency for agitation with higher frequency and smaller amplitude conditions to form larger aggregates.
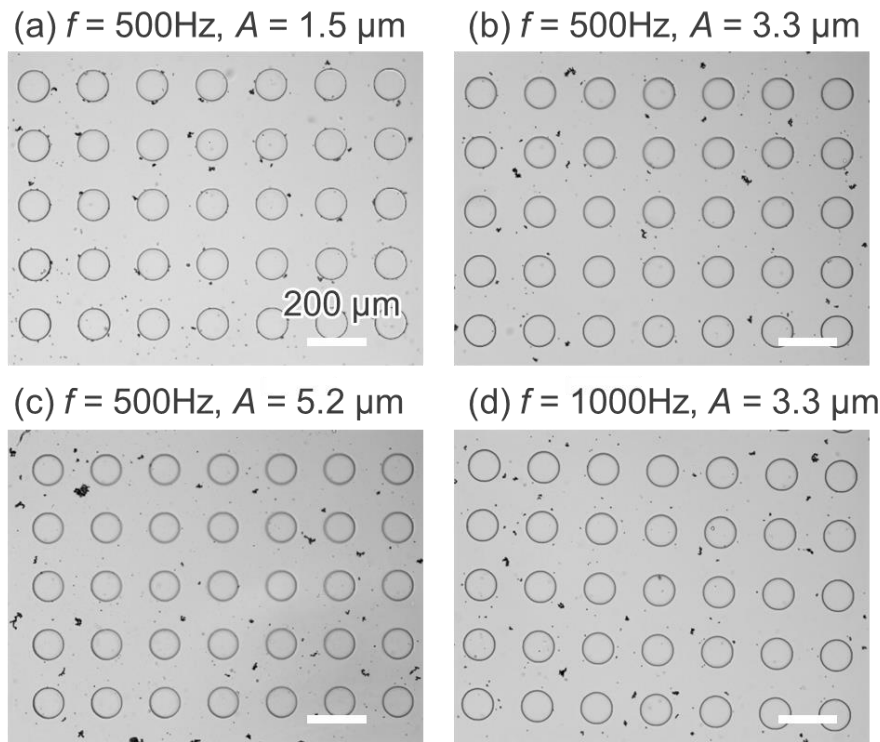


Fig. 3-9 Microscopic bright images of particles on the substrate with micropillars taken at 15 min after application of the VIF with vibration conditions in (a) $f = 600$ Hz, and $A = 2$ μm, (b) $f = 800$ Hz, and $A = 2$ μm, (c) $f = 200$ Hz, and $A = 8$ μm, (d) $f = 200$ Hz, and $A = 9$ μm. Pillar geometry was set to $h = 100$ μm and $S = 400$ μm.
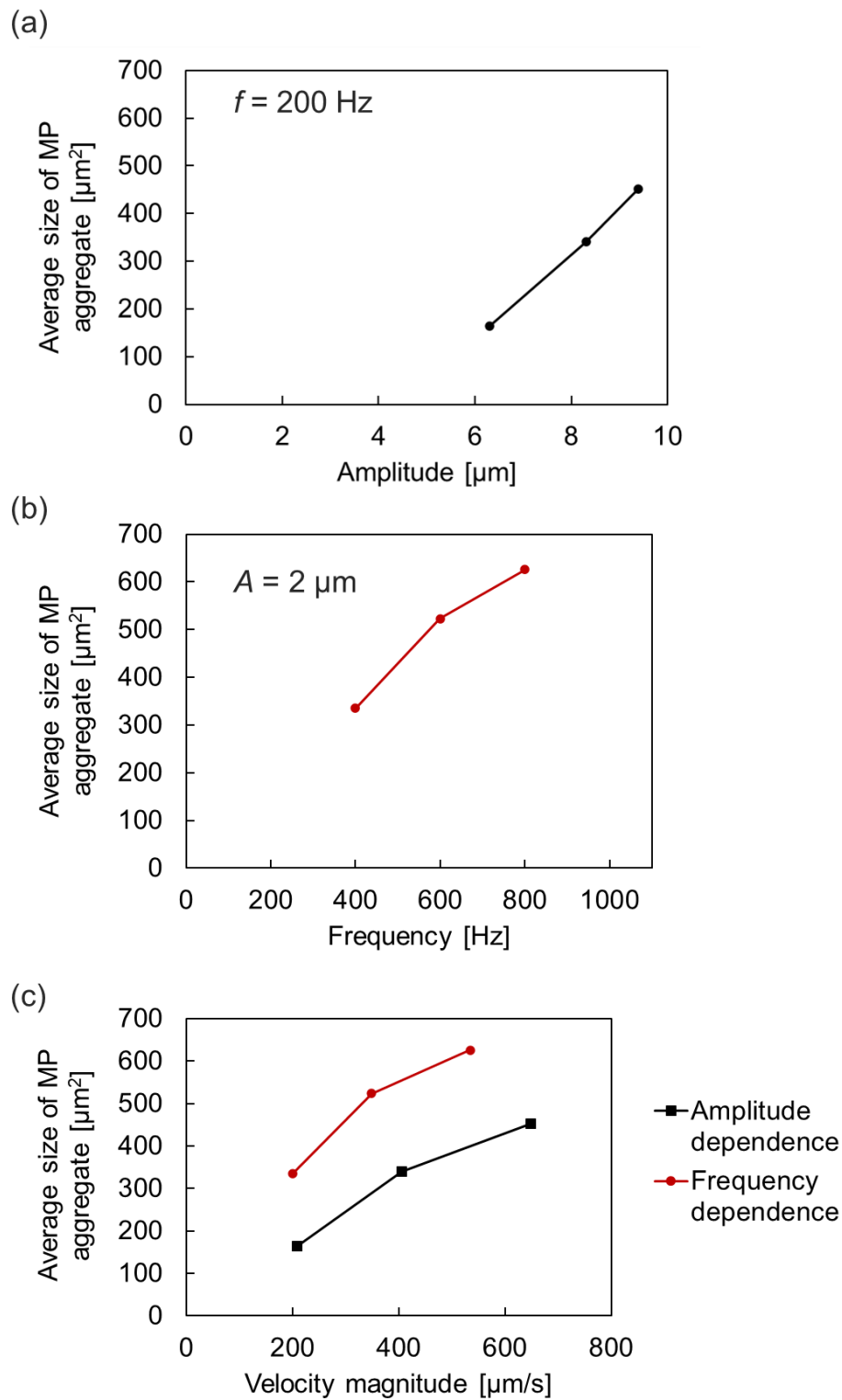
Fig. 3-10 (a) Relationship between average size of CP aggregates and amplitude and frequency. (b) relationship between the average size of CP aggregates and velocity magnitude. Pillar geometry was set to $h = 100$ μm and $S = 400$ μm.

### 3.4.3. Effect of pillar geometry

Next, we investigated the effect of the pillar arrangement on the aggregate formation under conditions identical to those in Fig. 2-17 with a constant height of $h = 100$ μm. The vibration condition is set to $f = 600$ Hz and $A = 2$ μm. Fig. 3-11 shows microscopic bright images of particles on the substrate with micropillars at 15 min after application of the VIF in various pillar arrangements. The binarized image for CPs aggregate detection is shown in Fig. 3-12. Under the condition where the inter-pillar separation was set to $S = 200$ μm (Fig. 3-11 (a)), the size and location of relatively large aggregates exhibited randomness. On the other hand, under the $S = 400$ μm conditions (Fig. 3-11 (b)), uniform aggregates were consistently found near each pillar. For $S = 600$ μm condition (Fig. 3-11 (c)), in addition to the induction of larger aggregates, small aggregates were detected as shown in the binarized image (Fig. 3-12). For the formation of the aggregates with $S = 400$ μm in the hexagonal array (Fig. 3-11 (d)), uniform aggregates were induced around near each pillar, similar to the $S = 400$ and 600 μm conditions in the square array.
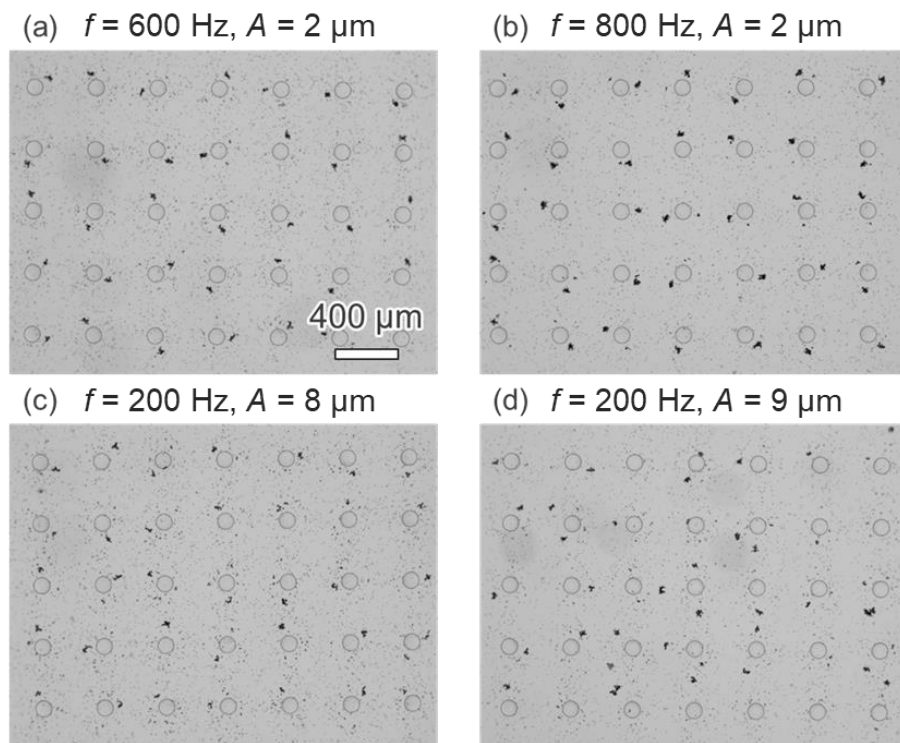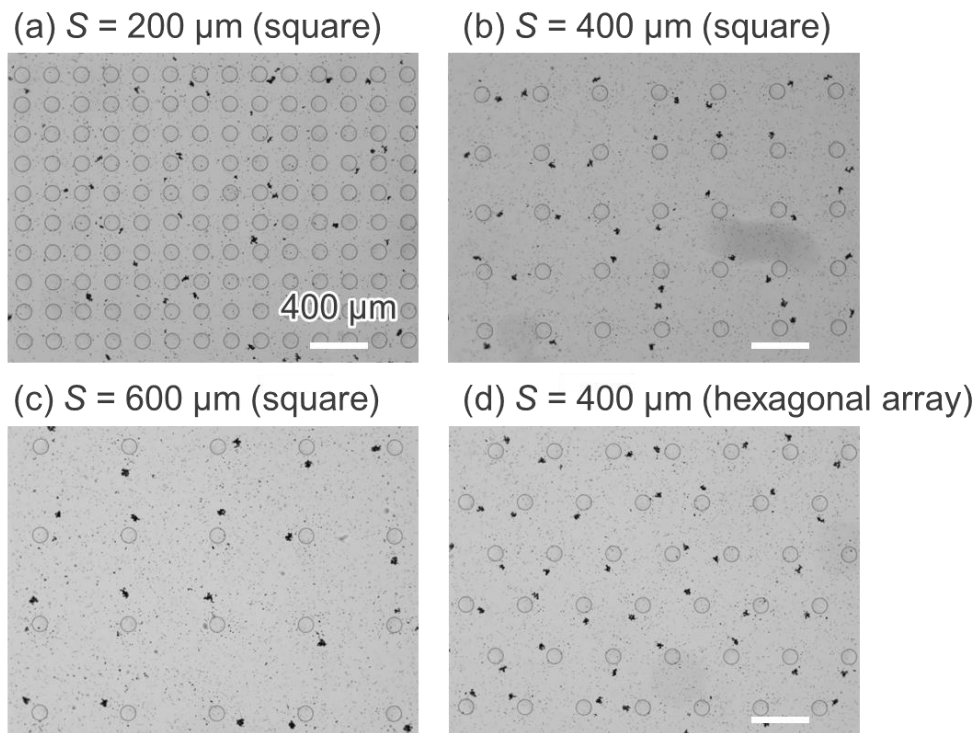


Fig. 3-11 Microscopic bright images of particles on the substrate with micropillars taken at 15 min after application of the VIF with (a) 200 μm, (b) 400 μm, (c) 600 μm for square, and (d) 400 μm for the hexagonal array. The conditions of vibrations were $f= 600$ Hz and $A= 2$ μm for $h = 100$ μm.

(a) $S$ = 200 µm (square)　　(b) $S$ = 400 µm (square)

400 µm

(c) $S$ = 600 µm (square)　　(d) $S$ = 400 µm (hexagonal array)
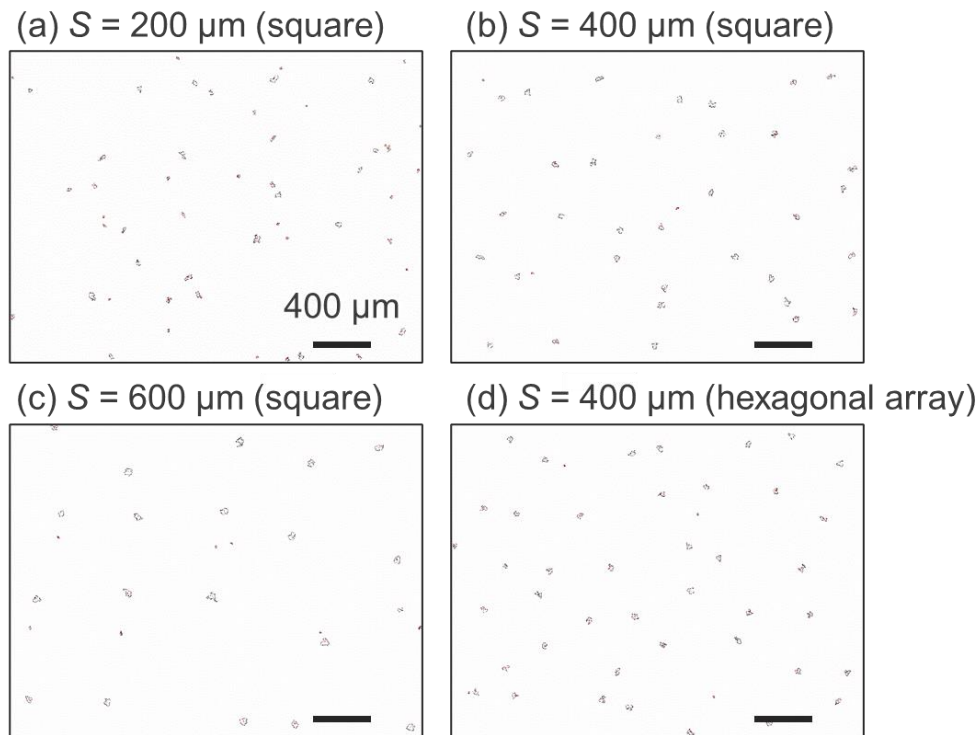
Fig. 3-12 Binarized images of CPs aggregates on the substrate with micropillars taken at 15 min after application of the VIF with (a) 200 µm, (b) 400 µm, (c) 600 µm for square and (d) 400 µm for the hexagonal array. The conditions of vibrations were $f$ = 600 Hz and $A$ = 2 µm for $h$ = 100 µm.

The subsequent quantitative examination of the average area of CP aggregates in each arrangement is shown in Fig. 3-13. For square array cases, $S$ = 200 µm got the smallest aggregate size. With wider pillar separation to $S$ = 400 µm and 600 µm, aggregate size increased. The average area of CP aggregates in the hexagonal array is almost the same as a square array. For the variation in each aggregate size, a significant variability was observed with $S$ = 200 µm and $S$ = 600 µm. In contrast, $S$ = 400 µm resulted in a smaller variation, reflecting the formation of approximately uniform-sized aggregates around each pillar. In the hexagonal array case with $S$ = 400 µm, the variability of the aggregate area was comparable to those in the square array with $S$ = 400 µm. Under the condition of $S$ = 200 µm, it is presumed that the occurrence of aggregates at random locations contributes to the variability in aggregate size. In the case of $S$ = 600 µm, the presence of both large and small aggregates contributes to the variability in size as shown in Fig. 3-13. These results suggest that a separation of $S$ = 400 µm leads to relatively uniform aggregate formation.
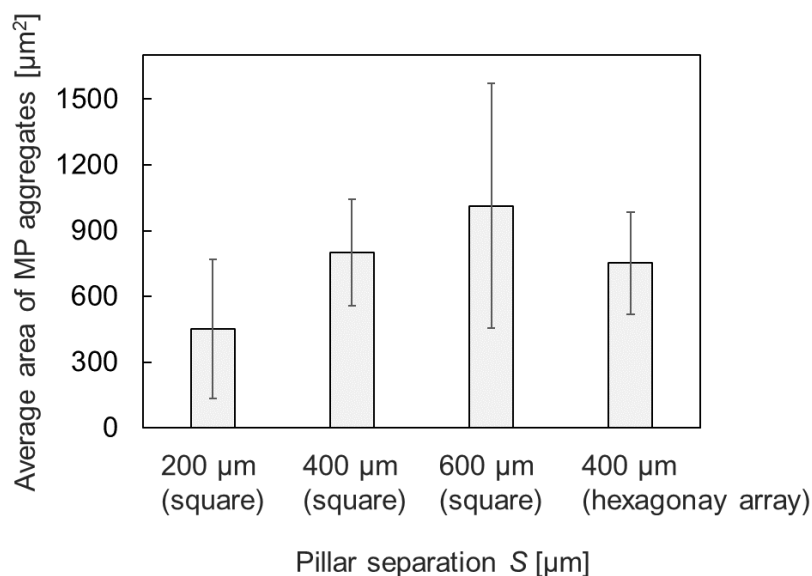
Fig. 3-13 The conditions of circular vibrations in all cases were: $h = 100$ μm, $f = 500$ Hz, and $A = 3.3$ μm. The average area of capture-bead aggregates in bright-field images under various pillar separation conditions. Error bars represent the standard deviations of the area of CP aggregates in the microscopic bright image.

Table 3-3. shows the relationship between the number of pillars and aggregates in each pillar arrangement on the captured screen. For $S = 200$ μm, despite having 154 pillars, only 54 aggregates were formed. In contrast, for $S = 600$ μm, with 15 pillars, a larger number of aggregates, specifically 44, were formed. These results correspond to the conditions with a large standard deviation in aggregate area, as shown in Fig. 3-13 indicating the non-uniformity of aggregates. On the other hand, for $S = 400$ μm in both square and hexagonal arrays, a similar number of aggregates were formed, with little difference in the number of pillars. In the hexagonal array, the higher number of pillars in the given space leads to a larger number of formed aggregates. The subsequent parameter study of vibration conditions utilized the $S = 400$ μm condition with a square array.

These findings suggest that narrower inter-pillar separation facilitated the stochastic collision of aggregates due to interference between vortices, whereas wider separation led to localized collision events of CPs within individual vortices. These phenomena contributed to enhancing the reproducibility of NPs detection. In our future research endeavors, we intend to conduct an in-depth investigation into the impact of flow patterns on aggregate formation, aiming to further reduce the assay time.

Table 3-3 Relationship between the number of pillars and aggregates in each pillar arrangement.

| Pillar separation $S$ | 200 µm (square array) | 400 µm (square array) | 600 µm (square array) | 400 µm (hexagonal array) |
|---|---|---|---|---|
| Number of pillars | 154 | 35 | 15 | 42 |
| Number of aggregates | 54 | 38 | 44 | 46 |

### 3.4.4. Quantification of NP concentration

Next, we conducted experiments to quantify NPs concentration. Specifically, we examined the dependence of the average area of CP aggregates on the concentration of NPs to test the capability of the proposed system for quantitative measurements. Again, two pillar geometric conditions with smaller ($h$ = 50 µm/$S$ = 200 µm) and larger ($h$ = 100 µm/$S$ = 400 µm) cases were used. The vibration conditions for each geometry were set to $f$ = 500 µm, $A$ = 3.3 µm and $f$ = 600 µm, $A$ = 2 µm, respectively. These settings demonstrated minimal variations in aggregate formation, as discussed in the previous section.

First, a smaller geometric condition was used. Fig. 3-14 shows the time evolution of the average area of CP aggregates under the vibration conditions: $f$ = 500 Hz and $A$ = 3.3 µm. In all conditions that contain NPs in the sample, the average area of CP aggregates increased almost linear linearly over time (NP concentrations of $5.7 \times 10^9$ /mL, $1.1 \times 10^9$ /mL, $5.7 \times 10^8$, /mL, and $5.7 \times 10^7$ /mL). Fig. 3-15 shows Beeswarm plots depicting the area of CP aggregates after 15 min for each NPs concentration. These results support the hypothesis that the quantity of NPs adsorbed onto the CPs increases with NP concentration, facilitating aggregate formation. On the other hand, the incremental growth in the average area of CP aggregates remained small within the control experiment where NPs were absent (gray line). These results provide quantitative evidence that the presence of NPs in the sample correlates with the average area of CP aggregates within the VIF.

Fig. 3-14 Time evolution of the average area of CP aggregates in various concentrations of NPs.
Error bars indicate the standard deviation from triplicate experiments.
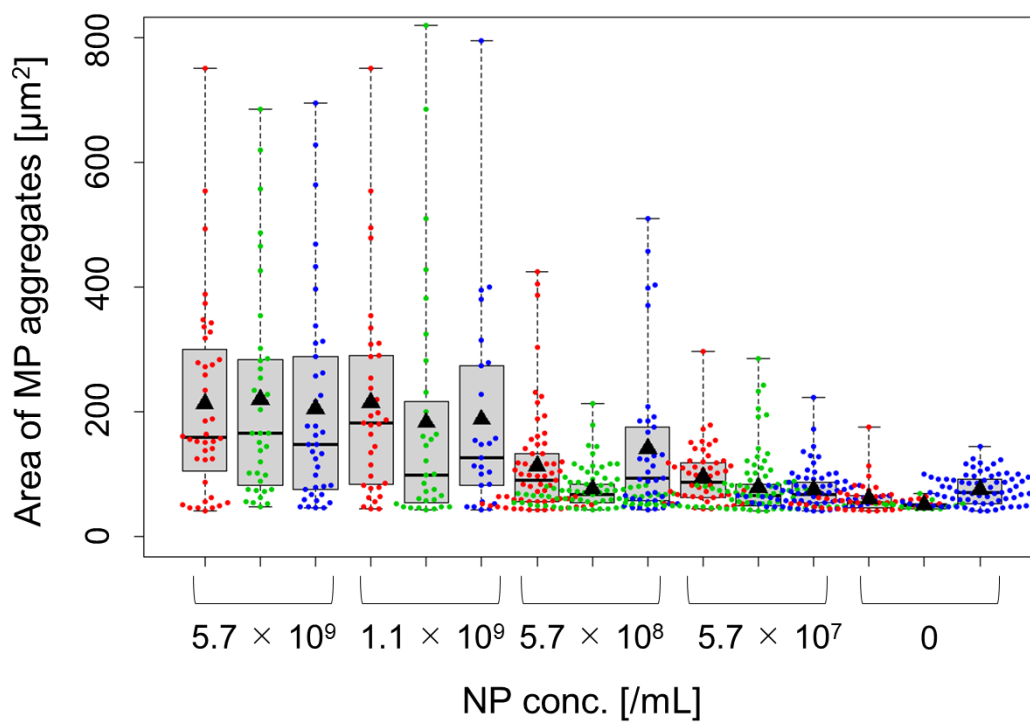


Fig. 3-15 Beeswarm plots illustrating MP aggregate area at the 15 min for each NP concentration.
(The results presented here are from triplicated experiments.)

The relationship between the NP concentration and the slope of the time-dependent increase in the CP aggregates area is shown in Fig. 3-16. We selected the slope of increase in the CP aggregates area rather than the size at the plateau. This is because a clear and reproducible plateau was not induced in longer time mixing (~40 min). A statistically significant average could not be obtained within a single frame as the number of aggregates decreases.

Based on this graph, the concentration of NPs in the sample can be estimated. Linear regression analysis was conducted with the fitting equation of $y = 1.8629 \log x - 31.618$ with an $R^2$ value of 0.854. The LOD was determined to be $1.1 \times 10^8$ /mL, indicating that quantifying the NP concentration can be achieved by assessing the slope of the time-dependent increase in aggregate size beyond this concentration.
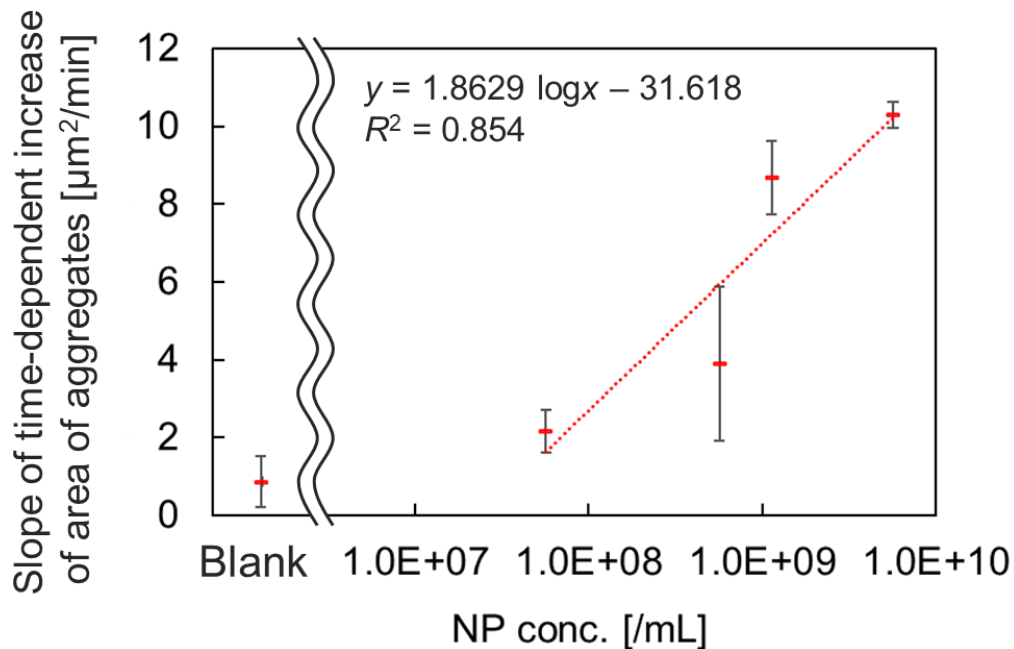


Fig. 3-16 Relationship between the NP concentration and the slope of the time-dependent increase of the aggregate size. Error bars indicate the standard deviation from triplicate experiments.

Next, a quantification test was conducted using a larger geometric condition ($h = 100$ μm/$S$ = 400 μm). Fig. 3-17 shows the time variation of the average area of the CP aggregates in the 5−25 min range, with vibration conditions set at $f = 600$ Hz and $A = 2$ μm. NPs concentrations were set to $5.7 \times 10^9$ /mL, $5.7 \times 10^8$ /mL, $1.1 \times 10^8$ /mL, and $7.6 \times 10^7$ /mL, while the constant CPs concentration was $3.3 \times 10^7$ /mL. In cases where NPs were present, the aggregate area significantly increased under the three higher concentration conditions compared to the 0 /mL condition. Particularly, at the highest concentration of $5.7 \times 10^8$ /mL, it reached almost a plateau of about 15 min. The size of the aggregates reached around 1000 μm², indicating a significant increase compared to the smaller geometric

condition ($h = 50$ μm and $S = 200$ μm). On the other hand, at the lowest concentration condition of $7.6 \times 10^7$ /mL, the area increase was comparable to the blank condition (0 /mL NPs concentration). Beeswarm plots of the area of the CP aggregates after 15 min for each NPs concentration are shown in Fig. 3-18.
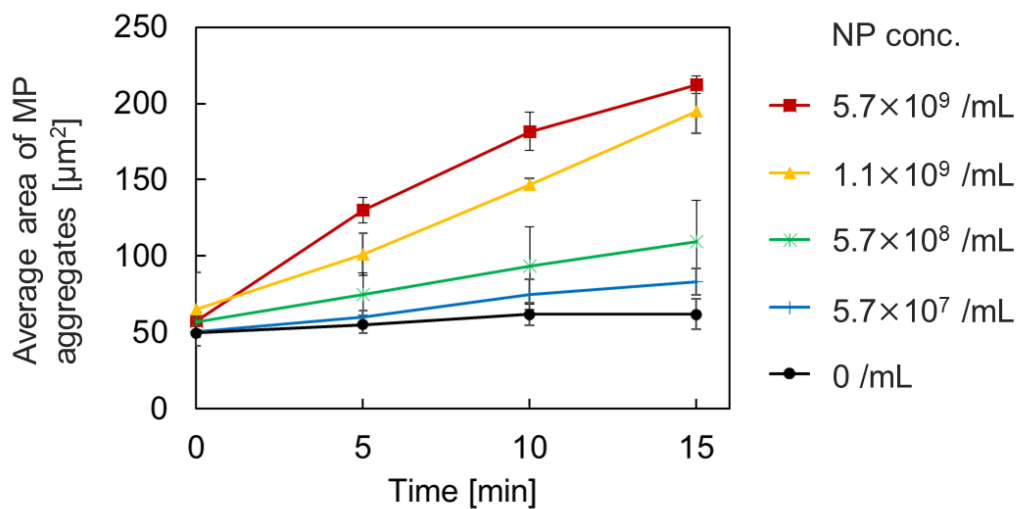


(b)
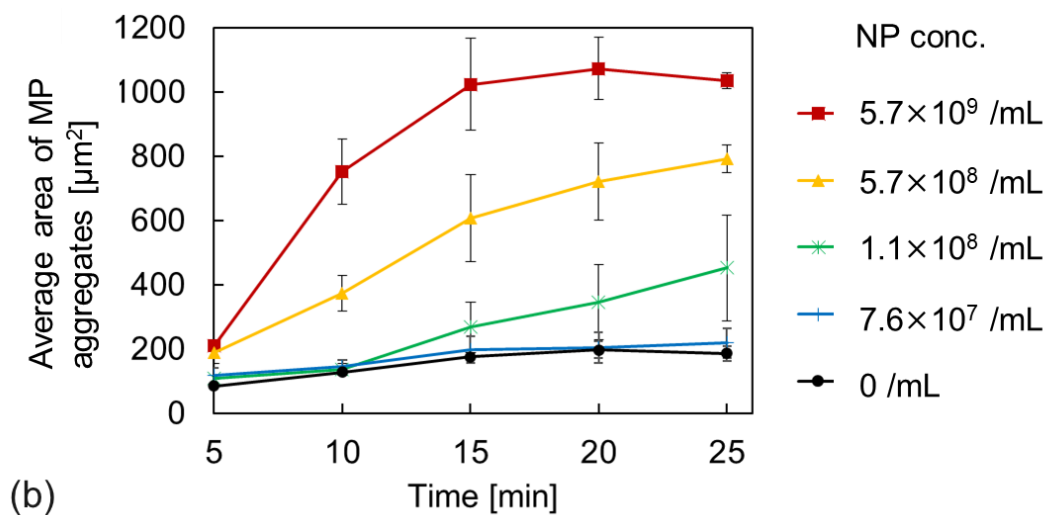
Fig. 3-17 Time evolution of the average area of CP aggregates in various concentrations of NPs. Error bars indicate the standard deviation from triplicate experiments.
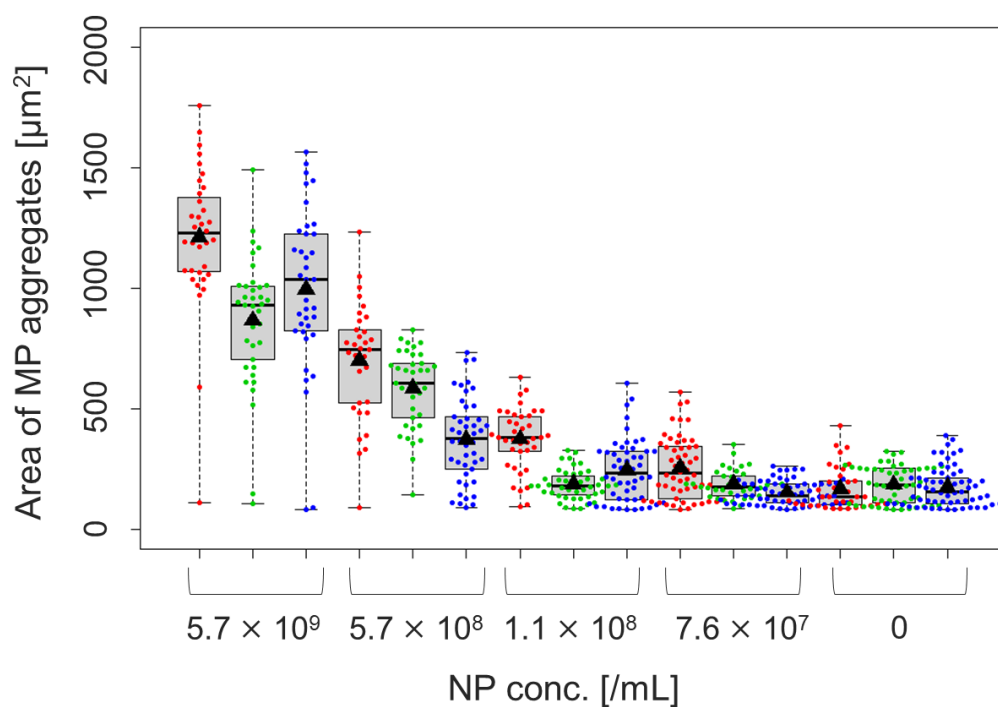
Fig. 3-18 Beeswarm plots illustrating MP aggregate area at the 15 min for each NP concentration. (The results presented here are from triplicated experiments.)

Quantitative analysis of NPs concentration was conducted under this. Fig. 3-19 shows the calibration curve derived from the slope of the increase of aggregate area for the linear region of 5−15 min. In this plot, linear regression analysis was performed with the fitting equation of $y = 16.329 \log x - 286.17$ with an $R^2$ value of 0.9979. The LOD was calculated as $8.2 \times 10^7$ /mL, suggesting that the NP concentration can be quantified by determining the slope of the time-dependent increase in aggregate size above this concentration.
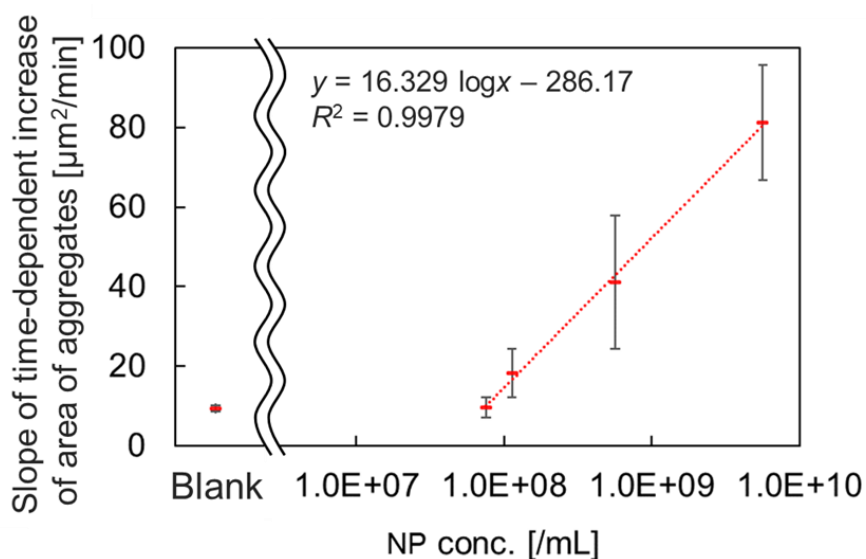
Fig. 3-19 Relationship between the NP concentration and the aggregate size. The vibration condition is set to $S = 400$ μm, $f = 600$ Hz, $A = 2$ μm. Error bars indicate the standard deviation from triplicate experiments.

Table 3-4 shows a comparison of detection performance in the pillar geometric conditions. In the case of a larger geometric condition, the resolution was 1/4 compared to the smaller geometric condition. Nevertheless, LOD, sensitivity, and $R^2$ showed an increase. Particularly, sensitivity increased by approximately eightfold, and $R^2$ approached 1, indicating that the predictions of the calibration curve are almost identical to the observed values. These results suggest an enhancement in detection accuracy despite the lower resolution in the larger geometric condition.

Table 3-4 Comparison of detection performance in different pillar geometric conditions.

| Pillar geometric condition | $h = 50$ μm, $S = 200$ μm | $h = 100$ μm, $S = 400$ μm |
|---|---|---|
| Resolution | 0.52 μm$^2$ | 2 μm$^2$ |
| Sensitivity (slope of the calibration curve) | 1.8629 | 16.3 |
| $R^2$ (coefficient of determination) | 0.854 | 0.9979 |
| Limit of detection (LOD) | $1.1 \times 10^8$ /mL | $8.2 \times 10^7$ /mL |

## 3.5. Summary of Chapter 3

We employed the VIF to immunoagglutination assays aimed at detecting NPs in minute samples. In a proof-of-concept experiment utilizing a model NP capture system based on avidin-biotin interactions, the VIF effectively induced the aggregation of CPs exclusively in the presence of the target NPs. In the quantification experiment, two configurations of pillar geometry were utilized, encompassing smaller ($h = 50$ μm and $S = 200$ μm) and larger ($h = 100$ μm and $S = 400$ μm) cases. Our findings indicated that the average area of CPs aggregates, assessed using standard bright-field microscopy and straightforward image analysis, was influenced by the velocity of local swirling flow. Additionally, an optimal velocity magnitude for the formation of large aggregates was identified for the smaller geometric case. On the other hand, under larger geometric conditions, the aggregation area did not decrease significantly even in high-velocity regions. Additionally, in the latter condition, relatively larger and uniform aggregates were induced. These trends of aggregate formation can be easily adjusted using vibration parameters and geometric conditions, indicating the versatility of our system for a wide variety of NP capture systems.

The performance of detection was compared under these two conditions. In the larger geometric condition, despite a detection resolution of approximately 1/4 of that in the smaller geometric condition, the performance of detection metrics such as LOD, sensitivity, and $R^2$ of the calibration curve was improved. This improvement is attributed to the formation of relatively uniform and larger aggregates in the larger geometric condition. Specifically, the enhanced uniformity in aggregate area led to increased reproducibility in aggregate formation, resulting in improved $R^2$ of the calibration curve. Additionally, the increased area of aggregates formed within the same time frame contributed to a higher slope in the initial phase of aggregate area growth, leading to a substantial enhancement in sensitivity. The above improved $R^2$ and sensitivity collectively contributed to the improvement of LOD. These results suggest that a larger geometric condition achieves a relatively large and uniform aggregate formation, which facilitates more accurate NPs detection compared to smaller geometric case, while using the avidin-biotin capturing system.

However, despite the improvements in sensitivity and $R^2$, the improvement in LOD remained limited to the order of $10^7$ /ml. This can be attributed to the fact that, as indicated in Table 3-2, at the order of $10^7$ /ml, only several numbers of NPs can be adsorbed by a single CP, which may not be sufficient for effective aggregate formation. Further enhancements in LOD should be conducted through considerations beyond the physical parameters described in this thesis. Specifically, using smaller-diameter CPs to increase the surface-area-to-volume ratio is one potential avenue for improvement. Nevertheless, the extensive concentration range of NPs within the sample ($10^7$–$10^9$ /ml) can be assessed by analyzing the slope of the time-dependent increase in the projected area of

60

aggregates. This indicates the applicative potential of our methodology for effectively detecting NPs over a diverse concentration spectrum.

# Chapter 4.

# Three-dimensional numerical simulation of the flow field
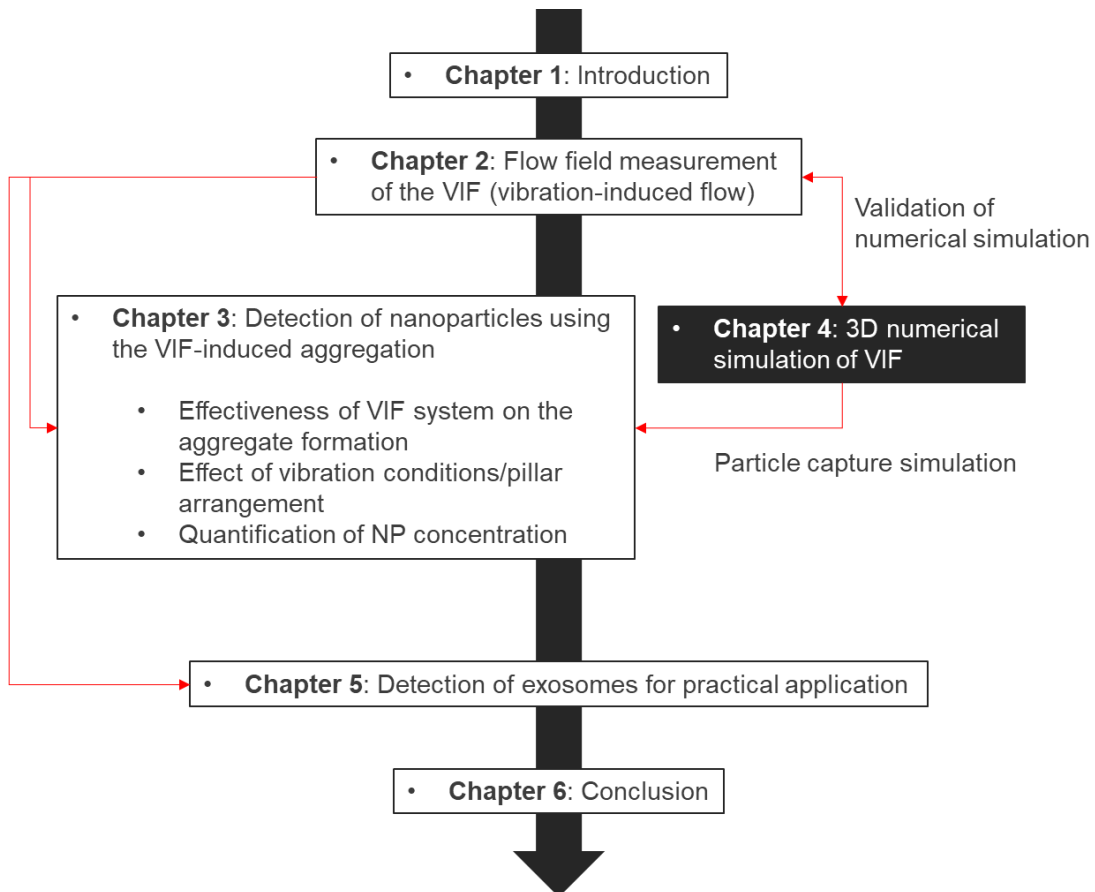
## 4.1. Overview

In this chapter, we present a numerical model to predict VIF under various vibration conditions. This model is an extension of our previously reported numerical simulation (Kaneko et al. 2018), which focused on understanding the three-dimensional behavior of VIF. Our earlier work involved the development of a numerical simulation tool capable of directly solving the Navier-Stokes equations and continuity equations in a 3D computational domain. This tool enables the calculation of the net-induced flow around a vibrating micropillar without relying on perturbation theory or introducing moving boundaries. In our methodology, we solve the governing equations in a coordinate system that moves with the vibrating substrate containing the micropillar. The effects of vibration are incorporated as a time-varying inertial force acting on the fluid volume. This approach eliminates the need for moving boundaries. Moreover, the volume penalization method (Osher and Sethian 1988) facilitates the seamless integration of micropillars with complex shapes into the Cartesian grid system. Subsequently, the resulting time-dependent velocity field transforms into the coordinate system at rest. Previously, we applied this numerical code to analyze the flow field around a simple cylindrical pillar with circular vibration. The simulation results, including vector plots, velocity distributions, and 3D secondary flow, exhibited good agreement with experimental PIV (Particle image velocimetry) observations (Kaneko et al. 2018). This numerical code offers the advantage of calculating the flow field around periodically vibrating solid structures without the use of moving boundaries, achieved by employing a moving coordinate system fixed to the vibrating pillars. For practical applications, enhancing mixing characteristics is crucial, particularly through the introduction of a non-axisymmetric pillar combined with different types of vibration. In this context, numerical simulations serve as a promising tool for optimizing both the 3D shape of a micropillar and the vibration parameters. However, to date, no studies have validated numerical simulations through a comprehensive comparison between simulated and experimental results for complex micropillar structures under various vibration conditions.

Moreover, the development of a numerical computation method capable of calculating the flow field around three-dimensionally vibrating micropillars would enable the prediction of particle behavior in agitation. Here, we conducted particle capture simulations to predict the early stages of aggregate formation using the numerical simulation tool.

## 4.2. Numerical procedures

### 4.2.1. Computational domain and vibration conditions

We calculated the flow field surrounding a micropillar positioned between two parallel plates subjected to periodic vibration. The computational domain is illustrated in Fig. 4-1 (a). We assume the liquid is incompressible and exhibits Newtonian fluid behavior (water). The top and bottom boundaries correspond to the two parallel plates, with a pillar affixed to both plates and positioned at the center of the computational domain. The half-height of the computational domain is represented by $\delta$. The two orthogonal directions tangential to the substrate are designated as $x$ and $z$, while the direction normal to the wall is $y$. The origin is positioned at the center of the bottom plate. For this study, the diameter and height of the cylindrical pillar were set to 100 µm, matching the height of the computational domain. The width of the computational domain occupied by a single pillar was set at 400 µm. We selected these dimensions for ease of flow field comparison in experiments. Specifically, the height was chosen to induce a relatively gentle velocity gradient in the vertical direction compared to smaller pillars in the range of several tens of µm, aiming to minimize errors in the vertical direction. choice of 400 µm width enables the observation of the flow around a single pillar with almost minimal interference between adjacent pillars. We assume that the entire system containing the substrate, pillar, and water, is subjected to either circular vibrations (Fig. 4-1 (c)) or (Fig. 4-1 (d)) parallel to the substrate. For circular vibration, either clockwise (CW) or counter-clockwise (CCW) were applied. The vibration period and the amplitude are represented as $A$ and $T$, respectively. In the present numerical model, we adopt a moving coordinate system that follows the motion of the plates instead of using a fixed coordinate system, to eliminate the occurrence of moving boundaries. To incorporate the effects of vibrations, a body force (inertial force) rotating horizontally is applied within the fluid region. Subsequently, the flow field acquired in the moving coordinate system is transformed into the fixed coordinate system.
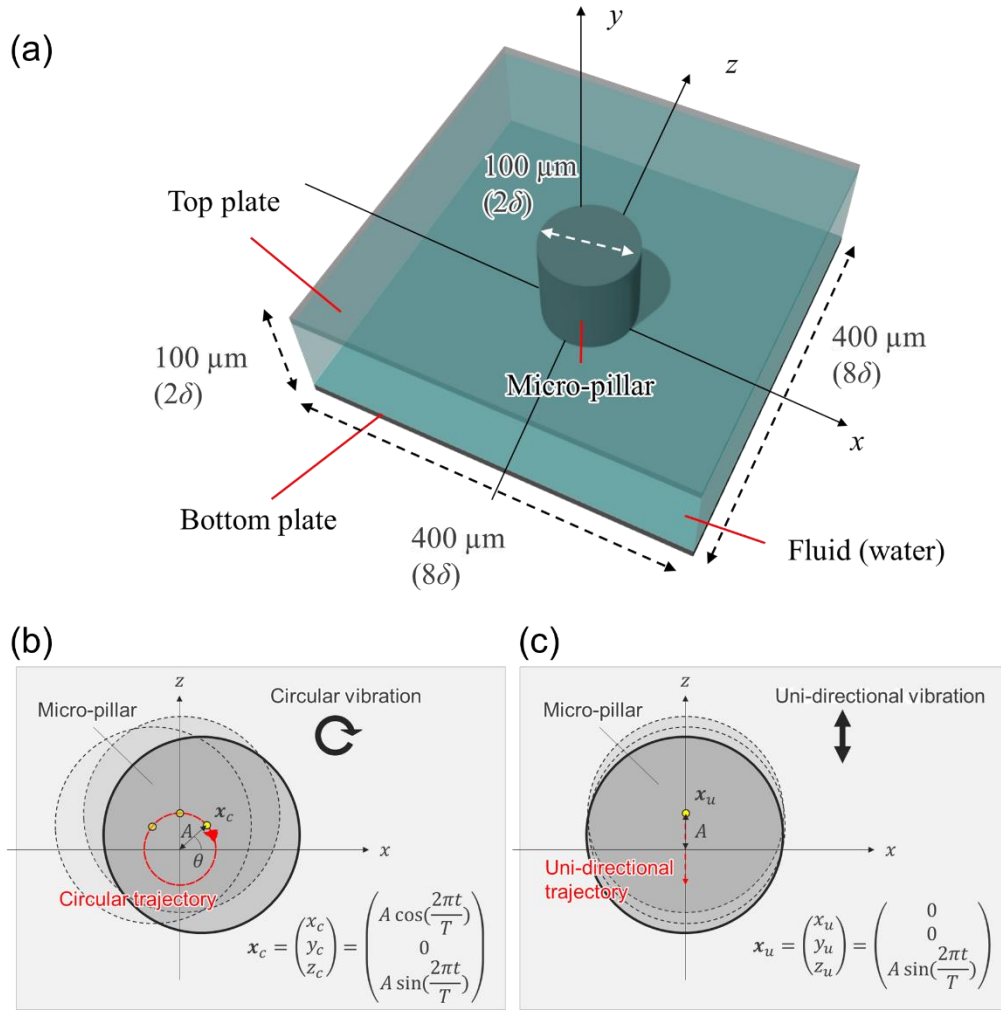
Fig. 4-1 (a) Schematic of the computational domain and coordinate system cylindrical pillar. The trajectory of the micropillar subjected to (b) circular vibration and (c) rectilinear vibration, respectively.

Considering the incompressibility of the liquid and its Newtonian fluid characteristics, the flow is described by the governing equations of Navier–Stokes and continuity:

$$\frac{\partial \underline{u_i}}{\partial t} + \underline{u_j}\frac{\partial \underline{u_i}}{\partial \underline{x_j}} = -\frac{1}{\rho}\frac{\partial \underline{p}}{\partial \underline{x_i}} + v\frac{\partial^2 \underline{u_i}}{\partial \underline{x_j}\partial \underline{x_j}}, \tag{4-1}$$

$$\frac{\partial \underline{u_i}}{\partial \underline{x_i}} = 0, \tag{4-2}$$

where $v$, $\rho$, and $\underline{p}$ represent kinetic viscosity, density of the fluid, and static pressure, respectively. The two orthogonal directions tangential to the substrate are designated as $\underline{x}$ and $\underline{z}$, while the direction normal to the wall is $\underline{y}$. Time is denoted as $\underline{t}$. We introduce under-bar, which indicates a

65

physical quantity in the fixed coordinate system, to distinguish these equations from the moving coordinate along a subsequently defined circular orbit. The origin of the computational domain is placed at the center of the bottom substrate. $\underline{u_i}$ represents the fluid velocity, where the subscript $i$ represents, $i$ = 1, 2, 3 corresponds to the three directions $x$, $y$, $z$, respectively. A micropillar, with a height identical to the computational domain $2\delta$, is affixed to the bottom substrate. As well as the top and bottom walls (i.e., $y$ = 0 and $2\delta$), surface of the pillar are subjected to non-slip conditions. For horizontal directions $x$ and $z$, periodic boundary condition is applied, indicating that the geometry shown in Fig. 4-1 (a) repeats in horizontal two directions. As shown in Fig. 4-1 (c), (d), micropillar is subject to circular and rectilinear orbit. Using the radius and period of the oscillation $A$ and $T$, the relative displacements of the micropillar $\boldsymbol{x_C}$ and $\boldsymbol{x_U}$ are expressed as

$$\boldsymbol{x_C} = \begin{pmatrix} x_C \\ y_C \\ z_C \end{pmatrix} = \begin{pmatrix} A\sin\left(\dfrac{2\pi t}{T}\right) \\ 0 \\ A\cos\left(\dfrac{2\pi t}{T}\right) \end{pmatrix}, \qquad (4\text{-}3)$$

$$\boldsymbol{x_U} = \begin{pmatrix} x_U \\ y_U \\ z_U \end{pmatrix} = \begin{pmatrix} A\sin\left(\dfrac{2\pi t}{T}\right) \\ 0 \\ 0 \end{pmatrix}, \qquad (4\text{-}4)$$

For the opposite direction of circular in this CW direction, the displacement in CCW is represented as $-\boldsymbol{x_C}$. The velocity of the solid substrate, denoted as $\boldsymbol{u_C}$ and $\boldsymbol{u_C}$, can be determined by conducting the time derivative of $\boldsymbol{x_C}$ and $\boldsymbol{x_U}$ as follows;

$$\boldsymbol{u_C} = \begin{pmatrix} \dfrac{dx_C}{dt} \\ \dfrac{dy_C}{dt} \\ \dfrac{dz_C}{dt} \end{pmatrix} = \begin{pmatrix} \dfrac{2\pi A}{T}\cos\left(\dfrac{2\pi t}{T}\right) \\ 0 \\ -\dfrac{2\pi A}{T}\sin\left(\dfrac{2\pi t}{T}\right) \end{pmatrix} \qquad (4\text{-}5)$$

$$\boldsymbol{u_U} = \begin{pmatrix} \dfrac{dx_U}{dt} \\ \dfrac{dy_U}{dt} \\ \dfrac{dz_U}{dt} \end{pmatrix} = \begin{pmatrix} \dfrac{2\pi A}{T}\cos\left(\dfrac{2\pi t}{T}\right) \\ 0 \\ 0 \end{pmatrix} \qquad (4\text{-}6)$$

We introduce another coordinate system $\boldsymbol{x} = (x, y, z)^T$, which moves at the identical velocity as the substrate.

$$x = \begin{pmatrix} x \\ y \\ z \end{pmatrix} = \begin{pmatrix} \underline{x} \\ \underline{y} \\ \underline{z} \end{pmatrix} - \begin{pmatrix} x_C \\ 0 \\ x_C \end{pmatrix}, \tag{4-7}$$

Thus, the relative fluid velocity to the substrate is expressed as:

$$u = \begin{pmatrix} u \\ v \\ w \end{pmatrix} = \begin{pmatrix} \underline{u} \\ \underline{v} \\ \underline{w} \end{pmatrix} - \begin{pmatrix} u_C \\ 0 \\ w_C \end{pmatrix}. \tag{4-8}$$

Here, a variable without an under-bar represents a quantity in the moving coordinate system. The governing equations (4-1) and (4-2) can be written in the moving coordinate by transforming to $x_i$ and $u_i$, from $\underline{x}_i$ and $\underline{u}_i$, respectively, as follows

$$\frac{\partial u_i}{\partial t} + u_j \frac{\partial u_i}{\partial x_j} = -\frac{\partial p}{\partial x_i} + \frac{1}{Re} \frac{\partial^2 u_i}{\partial x_j \partial x_j} + f_i, \tag{4-9}$$

$$\frac{\partial u_i}{\partial x_i} = 0, \tag{4-10}$$

A dimensionless inertia force $f_i$ indicates the effect of the vibration resulting from the acceleration/deceleration of the moving coordinate, expressed as

$$f_C = -\frac{d\mathbf{u}_c}{dt} = - \begin{pmatrix} \dfrac{du_C}{dt} \\ \dfrac{dv_C}{dt} \\ \dfrac{dw_C}{dt} \end{pmatrix} = \begin{pmatrix} A\left(\dfrac{2\pi}{T}\right)^2 \sin\left(\dfrac{2\pi t}{T}\right) \\ 0 \\ A\left(\dfrac{2\pi}{T}\right)^2 \cos\left(\dfrac{2\pi t}{T}\right) \end{pmatrix}. \tag{4-11}$$

$$f_U = -\frac{d\mathbf{u}_c}{dt} = - \begin{pmatrix} \dfrac{du_C}{dt} \\ \dfrac{dv_C}{dt} \\ \dfrac{dw_C}{dt} \end{pmatrix} = \begin{pmatrix} A\left(\dfrac{2\pi}{T}\right)^2 \sin\left(\dfrac{2\pi t}{T}\right) \\ 0 \\ 0 \end{pmatrix}. \tag{4-12}$$

Physical variables are normalized using the length scale $\delta$ and the oscillation period $T$ to generalize the problem. Hence, the normalized velocity scale is expressed as $U_{ref} = \delta/T$. The dimensionless coordinate is then expressed as

$$x^* \equiv \frac{x}{\delta} = \frac{1}{\delta}\begin{pmatrix} x \\ y \\ z \end{pmatrix}. \tag{4-13}$$

$$u^* \equiv \frac{x}{U_{ref}} = \frac{T}{\delta}\begin{pmatrix} u \\ v \\ w \end{pmatrix}. \tag{4-14}$$

A dimensionless quantity is denoted as a superscript of an asterisk. The normalized (dimensionless) pressure and time are denoted as $p^* = p/(\rho\ U_{ref}^2)$ and $t^* = t/T$, respectively. Equations (4-1) and (4-2) with dimensionless forms are expressed by substituting these relationships as

$$\frac{\partial u_i^*}{\partial t^*} + u_j^* \frac{\partial u_i^*}{\partial x_j^*} = -\frac{1}{\rho^*}\frac{\partial p^*}{\partial x_i^*} + v^* \frac{\partial^2 u_i^*}{\partial x_j^* \partial x_j^*} + f_i^*, \tag{4-15}$$

$$\frac{\partial u_i^*}{\partial x_i^*} = 0, \tag{4-16}$$

where the dimensionless inertia force $f^*_i$ is defined as

$$f_i^* = \frac{2\pi}{St}\begin{pmatrix} cos(2\pi\omega t) \\ 0 \\ sin(2\pi\omega t) \end{pmatrix}. \tag{4-17}$$

For the opposite direction of circular in the CW, the inertia force in the CCW direction is expressed as $-f_C$. as well as the case of displacement. After non-dimensionalizing all physical quantities by the half-height of the channel $\delta$ and the vibration period $T$, the aforementioned equations are solved in the actual calculation.

### 4.2.2. Numerical methods and conditions

For solving the governing equations (4-1) and (4-2) in the moving coordinate, we use a pseud-spectral method. Here, a solution is expanded by Fourier modes and Chebyshev polynomials in the $x$/$z$ directions and $y$ direction, respectively. Regarding the advancement of time, we use the Crank–Nicolson for the diffusion terms, while the convection terms are subject to the second-order Adams Bashforth scheme (Hasegawa and Kasagi 2011; Suzuki and Hasegawa 2017).

The numbers of modes applied is represented as ($N1$, $N2$, $N3$) = ($64 \times 33 \times 64$) in $x$, $y$, and $z$ directions, respectively. To eliminate aliasing errors, the 3/2 rule is applied, denoting that the non-linear terms are calculated 1.5 times finer in each direction of physical grid points. The time step, normalized by the vibration period $T$, is defined as $\Delta t^* = 1.0 \times 10^{-4}$, implying that $t^{*-1} = 10^4$ time steps are needed to calculate the velocity field for one vibration period $t^* = 1$. Rotational vibration is

introduced at $t = 60$ to attain a fully developed flow field after the calculation begins with a stationary flow at $t = 0$. Following the transient, the flow field becomes completely periodic in one vibration cycle.

### 4.2.3. Volume penalization method for defining the pillar shape

To enforce a no-slip condition at a solid surface with complex geometry, we use a volume penalization method. This technique is the category of immersed boundary methods, where a complex structure is incorporated into the cartesian coordinate system. Unlike employing a coordinate system fitted to the boundary, the immersed boundary offers advantages such as straightforward grid generation, irrespective of the complexity of geometry. Furthermore, precise discretization schemes designed for the cartesian grid system can be employed.

In this investigation, the pillar's geometry is initially represented by a level-set function $\phi_0$ (Osher and Sethian 1988). The level-set function $\phi_0$, a signed distance function from a surface, is commonly employed to describe intricate interface geometry. In this context, $\phi_0$ is defined as positive inside the solid and negative in the fluid domain. Subsequently, $\phi_0$ is transformed into the phase-identification function $\phi$. Within this transformation, $\phi$ is assigned unity in the solid regions and null in the fluid regions. To prevent numerical instability, the phase-identification function smoothly transitions from zero to one across the interface within a few grid points. Introducing an artificial damping force proportional to $\phi$ into the Navier–Stokes equation enforces the no-slip condition at the solid surface. Specifically, the conversion from the level-set function to the phase-identification function is achieved using the following formula:

$$\phi = 0 \qquad\qquad \phi_0 < -\delta_{int} \qquad\qquad (4\text{-}18)$$

$$\phi = \left[ 1 + \exp\left\{ \frac{4\left(\frac{\phi_0}{\delta_{int}}\right)}{\left(\frac{\phi_0}{\delta_{int}}\right)^2 - 1} \right\} \right]^{-1} \qquad -\delta_{int} < \phi_0 < \delta_{int} \qquad (4\text{-}19)$$

$$\phi = 1 \qquad\qquad \delta_{int} < \phi_0 \qquad\qquad (4\text{-}20)$$

The selected function is differentiable throughout the entire domain and precisely zero and unity in the fluid and solid domains, respectively. The imposition of a no-slip condition at the solid surface involves introducing an artificial damping force in the Navier-Stokes equations (4-15) as follows:

69

$$\frac{\partial u_i}{\partial t} + u_j \frac{\partial u_i}{\partial x_j} = -\frac{\partial p}{\partial x_i} + \frac{1}{Re}\frac{\partial^2 u_i}{\partial x_j \partial x_j} + f_i - \eta\phi u_i \qquad (4\text{-}21)$$

In this context, the final term on the right-hand side represents the term of the volume penalization. The term is non-zero at $\phi = 0$, effectively suppressing all velocity components within the solid. Equations (4-21) revert to the original Navier-Stokes equations (4-15) within the flow domain where $\phi = 0$. The strength of the volume penalization method lies in its capability to implement solid objects with diverse shapes by adjusting the spatial distribution of $\phi$ within the same Cartesian grid system. However, a drawback is the relatively slow grid convergence attributed to the smeared representation of the interface within a few grid points, as previously mentioned.
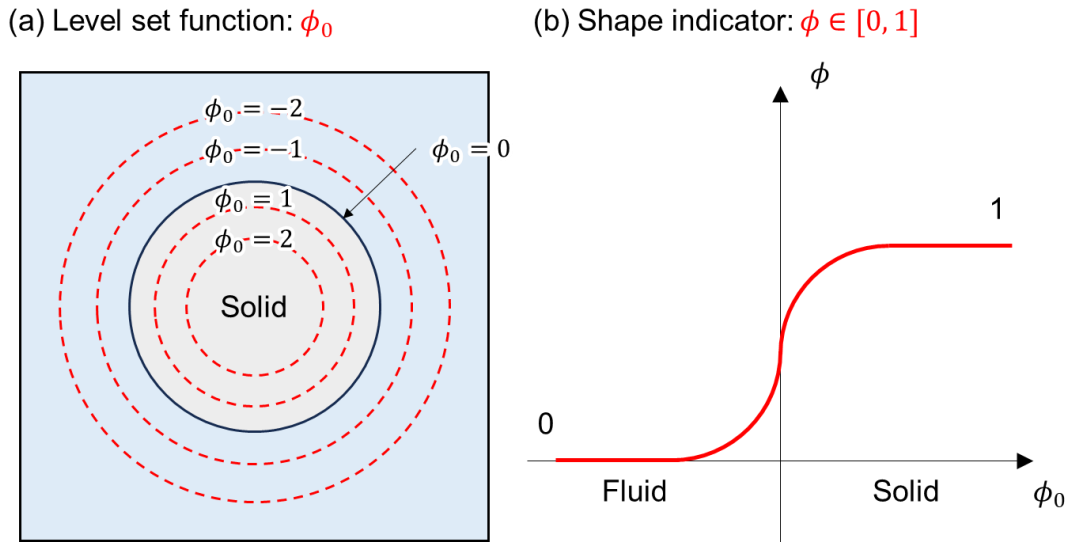


Fig. 4-2 Expression of the interface by (a) level-set function and (b) Shape indicator.

### 4.2.4. Lagrangian time-averaging of the flow field

For the calculation of an unsteady flow, it is widely acknowledged that a Lagrangian and Eulerian mean velocity field are not consistent (Andrews and Mcintyre 1978). Certainly, this phenomenon is demonstrated in the previous studies (Nama et al. 2017; Kaneko et al. 2018) for the case of VIF around oscillating micropillar. Thus, we calculate a time-averaged Lagrangian velocity field in the numerical simulation to compare the results with experimental ones. Here, trajectories of fluid particles are calculated by using the 4th order Runge–Kutta method (Suzuki et al. 2004; Kaneko et al. 2018) which applies time integration of local fluid velocity. Particles are initially placed at mid-plane ($y = 50$ μm) with tangentially uniform spacings of $\Delta x = \Delta y = 4.17$ μm in the three-dimensional

space. As the particle location is not always on the grid point precisely, linear interpolation of the sub-grid velocity is conducted using the velocities at the surrounding eight grid points. The integration of the particle Lagrangian velocity is performed using fifty instantaneous velocity fields within one vibrating cycle, with a smaller time step $\Delta t^* = 5.0 \times 10^{-3}$. Thus, the velocity field at a moment between the snapshots is acquired through linear interpolation of the two adjacent snapshots. Following the tracking of fluid particles for ten cycles of the applied vibration, the time-averaged Lagrangian velocity field is derived from the displacement between the initial and final positions of each particle.

### 4.2.5.   Particle capture simulation for predicting initial stage of aggregate formation

To predict the particle capture induced by the VIF, a Lagrangian fluid particle tracking simulation is conducted, using the instantaneous flow field. The time-averaged Lagrangian velocity obtained in the previous section merely represents particle motion with time-averaging. However, in reality, fluid particles move with periodic oscillations following the instantaneous velocity. Therefore, to precisely reproduce the behavior of the path of the fluid particle advection, it is necessary to use instantaneous velocity instead of time-averaged Lagrangian velocity. Particle tracking is performed for particles initially distributed in specific regions in the 3D flow field using the same numerical method used for Lagrangian time-averaging.

In practice, two types of virtual particles are placed in the computational domain: large capture particles ($D_{CP}$ = 3 μm) and small target particles ($D_{NP}$ = 0.15 μm). Using the obtained flow, a particle tracking simulation is conducted using the fourth-order Runge-Kutta method for the calculation of particle capture. Capture is determined to have occurred when the distance $P$ between the centers of the two types of particles became smaller than the sum of their radii (i.e., $P \leq (D_{CP} + D_{NP})/2$). Capture rate ($I_t$) is given as

$$I_t = \frac{N_t}{N_0} \times 100, \qquad\qquad (4\text{-}22)$$

where $N_0$ and $N_t$ represent total number of target particles at initial state and number of captured-target particles, respectively. Once capture occurs, the target particle is removed from the calculation and does not collide with any other capture particles. Number of arranged CP and NP is set to 32, 72, 405, 777, for $S$ = 150, 200, 400, and 600 μm, respectively. These numbers correspond to concentrations of $2.2 \times 10^7$ /mL, $2.2 \times 10^7$ /mL, $2.2 \times 10^7$ /mL, $2.6 \times 10^7$ /mL, and $2.2 \times 10^7$ /mL (Table 4-1).
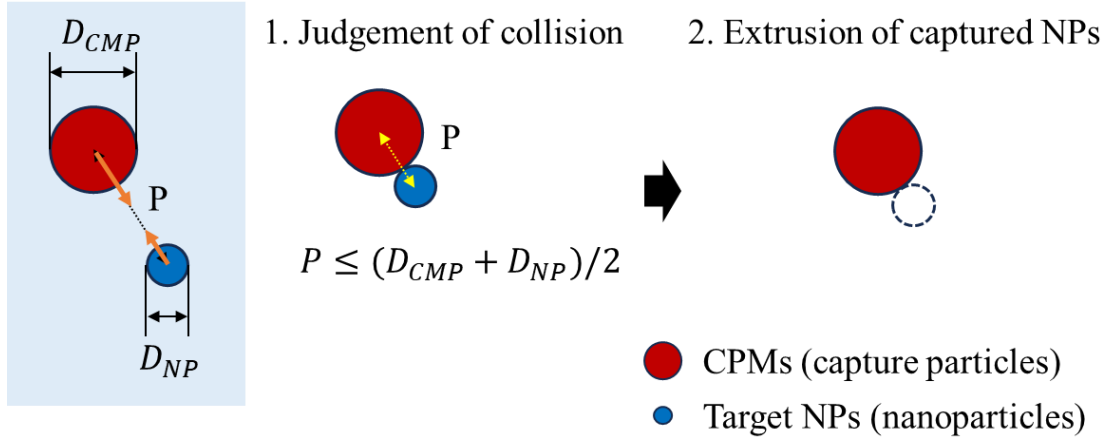
Fig. 4-3 Capture determination algorithm of CP and NPs.

Table 4-1 Concentration of NP in each condition.

| Pillar separation $S$ [μm] | 150 | 200 | 400 | 600 |
|---|---|---|---|---|
| Number of MPs | 32 | 72 | 405 | 777 |
| Conc. MPs [/mL] | $2.18 \times 10^7$ | $2.24 \times 10^7$ | $2.66 \times 10^7$ | $2.21 \times 10^7$ |
| Number of NPs | 32 | 72 | 405 | 777 |
| Conc. NPs [/mL] | $2.18 \times 10^7$ | $2.24 \times 10^7$ | $2.66 \times 10^7$ | $2.21 \times 10^7$ |

## 4.3. Comparison with experimental flow fields

At first, we compare the Lagrangian velocity field around the cylindrical pillar subject to circular vibration between the simulation and experimental PIV results. Fig. 4-4 (a, b) shows 2D vector plots of the Lagrangian flow fields at the mid-plane of the pillar height ($y = 50$ μm) obtained with the numerical simulation and PIV measurements. Vibration conditions are set to frequency $f = 600$ Hz (corresponding to the inverse of the vibration period, $T$) and an amplitude $A = 3.3$ μm, which are identical in the simulation and experimental. The flow fields with simulation and experiment exhibit consistency in terms of swirling flow patterns and their velocity magnitudes. In addition, the radial profiles of azimuthal velocity in Fig. 4-4 (c) show similar trends in the peak positions (around $r = 75$ μm, approximately 25 μm away from the pillar wall) and the decline of the profile with increasing distance from the pillar. These results confirm the accuracy of the current simulation.

Fig. 4-5 shows vector plots of the Lagrangian velocity field projected to the *x*-*y* and *z*-*y* plane. The flow around the pillar is predominantly two-dimensional, as it flows along the periphery of the pillar.



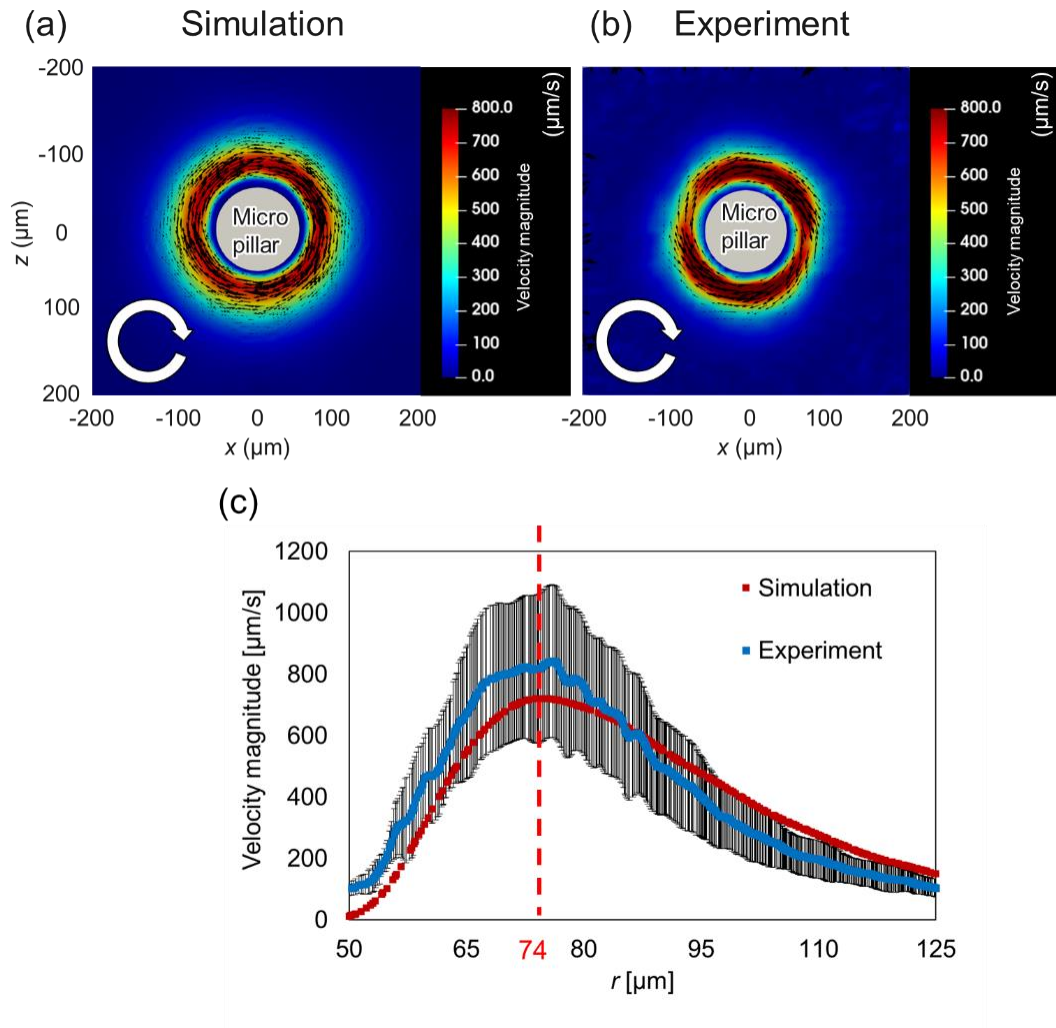Fig. 4-4 2D vector plots of time-averaged Lagrangian velocity field around a cylindrical pillar obtained through (a) the numerical simulation and (b) PIV measurement. The white arrows in each figure indicate the direction of circular vibration. (c) Lagrangian azimuthal velocity profiles as functions of the distance from the center of the pillar *r*. Error bars indicate the standard deviation from triplicate experiments.
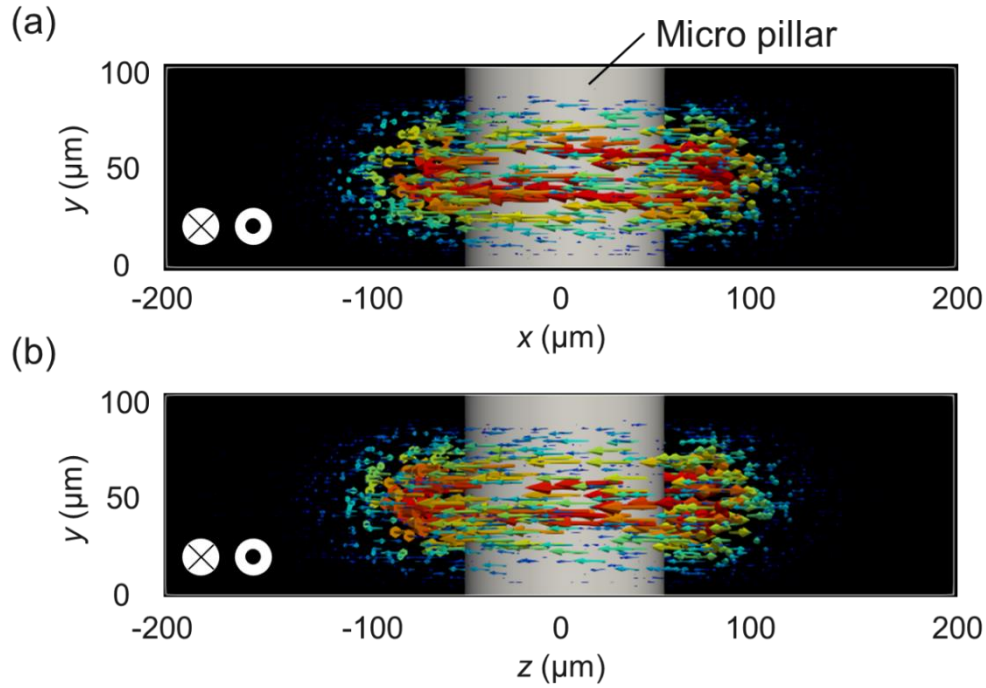
Fig. 4-5 Vector plots of the Lagrangian velocity field projected to *x-y* and *z-y* plane.

### 4.3.1. Time-averaged Lagrangian flow field with the rectilinear vibration

Next, we explore the time-averaged Lagrangian flow field around a cylindrical micropillar under the rectilinear vibration as defined by equations (4-12). The vibration condition is set to $f =$ 600Hz and $A = 3.3$ μm. 2D streamlines and vector plots obtained in the numerical simulation are shown in Fig. 4-6. The horizontal flow field obtained via PIV measurements for comparison with simulation is depicted in Fig. 2-19 in Chapter 2. In both simulation and experimental cases for streamlines (Fig. 4-6 (a) and Fig. 2-19 (a)), symmetrical flow patterns around a pillar featuring four vortices in each of the four quadrants are generated. The streamlines remain confined within each quadrant, illustrating the interference of flow among neighboring pillars arranged in a square lattice. Additionally, the horizontal flow field with the simulation and PIV measurement shows good agreement as shown in 2D vector plots at the mid-plane (Fig. 4-7 (b) and Fig. 2-19 (b)). In these vector plots, influx and ejection flows are generated in the directions of parallel and perpendicular to the vibration, respectively similar to previous studies (Lutz et al. 2005; Hayakawa et al. 2018). On the other hand, the magnitude of the ejection flow exceeds that of the influx flow. This phenomenon can be elucidated by considering the three-dimensionality of the induced Lagrangian flow as illustrated in Fig. 4-7 (c, d). For the vector plots in the *xy*-plane, ejected Lagrangian flow is generated which converges toward the center of the pillar height, leading to flow acceleration. Conversely, in the *zy*-

plane, the influx flow approaching the pillar side wall diverges towards the top and bottom plates. The 3D characteristics observed in Fig. 4-7 (c, d) were not anticipated by previous theoretical analyses under 2D flow assumption (Hayakawa et al. 2018), indicating that the necessity for a 3D analysis to accurately predict the Lagrangian velocity induced around a pillar subjected to rectilinear vibration.

For velocity magnitude, although vibration conditions $f$ and $A$ are the same as those of the circular vibration, the peak velocity magnitude is nearly eight times smaller in the case of rectilinear vibration. This trend suggests that circular vibration is more effective in inducing a net flow with a smaller input energy.
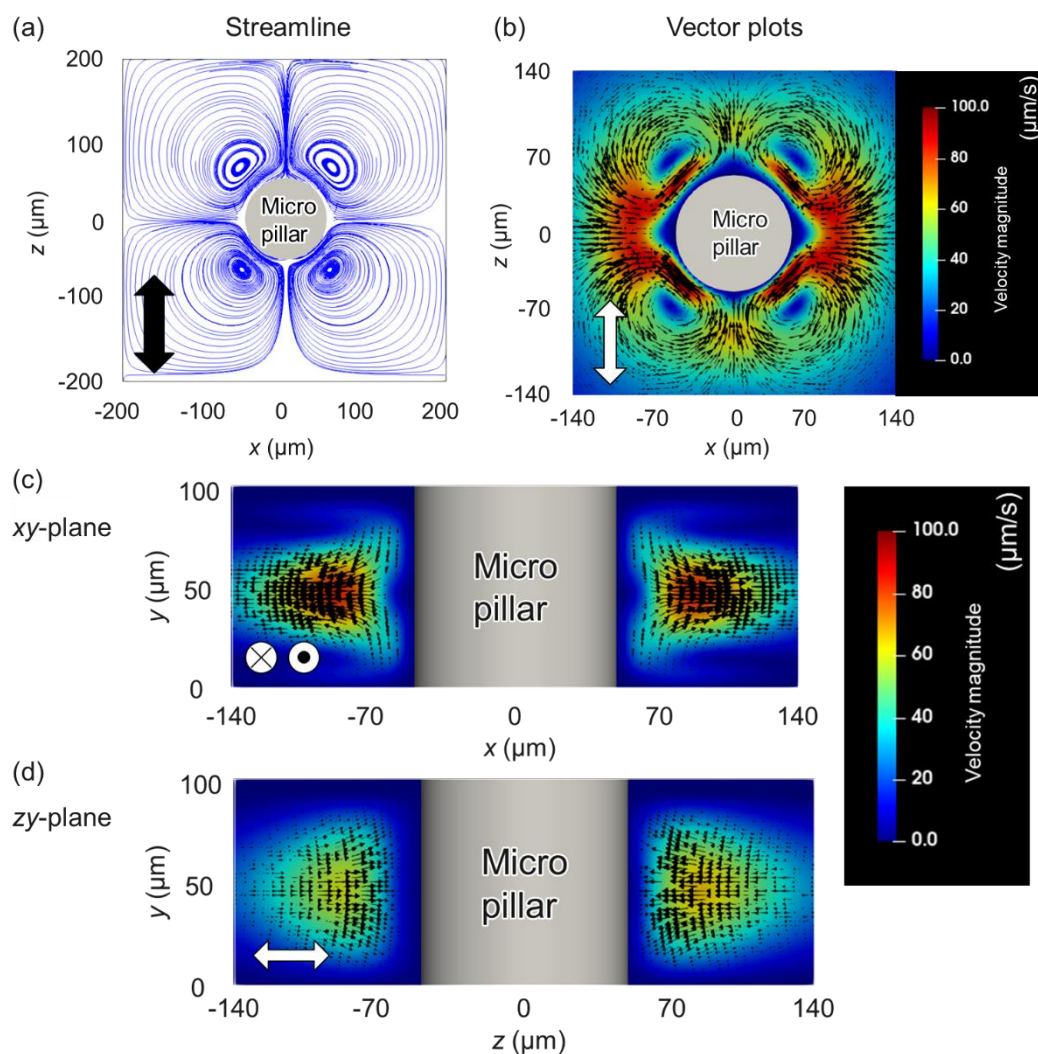


Fig. 4-6 (a) 2D streamlines of the time-averaged Lagrangian velocity field around a cylindrical pillar subjected to rectilinear vibration. (b) 2D vector plots of the Lagrangian velocity field. (c, d) Vector plots of the Lagrangian velocity field in the vertical plane for (c) $xy$-plane and (d) $zy$-plane. The black and white arrows in each figure represent the direction of the vibration.

Fig. 4-7 depicts the peak velocity magnitude of influx and ejection flows. Generally, the velocity magnitude obtained from the simulation is approximately 30% smaller than the experimental result. However, a consistent trend is apparent in both the simulation and experimental results, with the Lagrangian velocity being larger in the ejection flow compared to the influx flow.
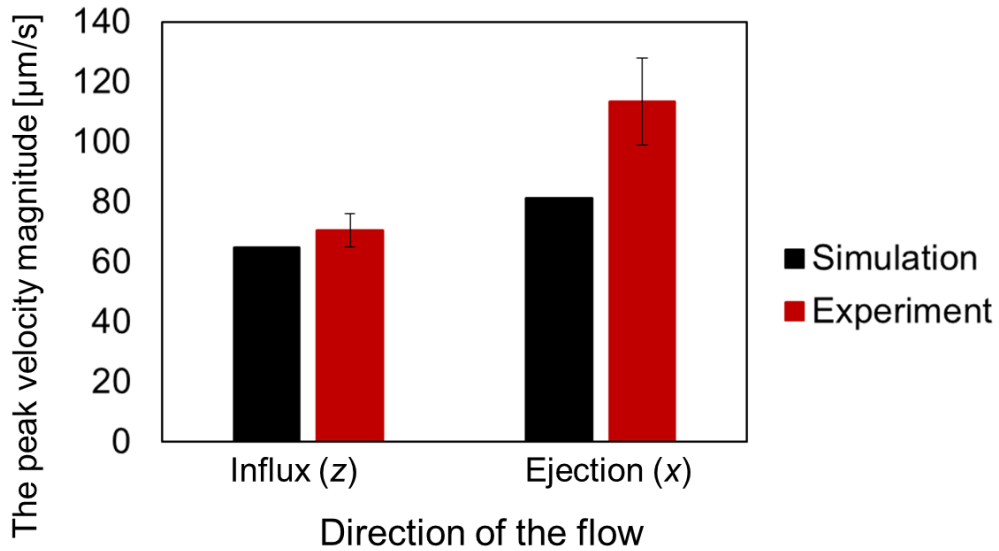


Fig. 4-7 Comparison of the peak velocity magnitude along the *x* (ejection) and *z* (influx) axes between the numerical simulation and PIV measurement. Error bars represent the standard deviation of triplicated experiments.

### 4.3.2. Time-averaged Lagrangian flow field with a complex shape

To enhance the versatility of our numerical simulation for sophisticated fluid control, we investigate a flow field around a pillar with an asymmetric cross-section, namely, a Ninja-star as illustrated in Fig. 4-8 (a). Specifically, we set the length of the arm $l$ to be 70 μm, with outside and inside curvatures ($R_1$ and $R_2$) of 35 μm and 30 μm, respectively. SEM images of asymmetric micropillars are shown in Fig. 4-8 (b). The entire system is driven by circular vibration, which can either clockwise (CW) or counter-clockwise (CCW), as illustrated in Fig. 4-1 (c). These scales and vibration patterns are defined following previous work (Hayakawa and Arai 2017). The vibration conditions in both the simulation and the experiment are consistent; $f = 600$ Hz and $A = 3.3$ μm.
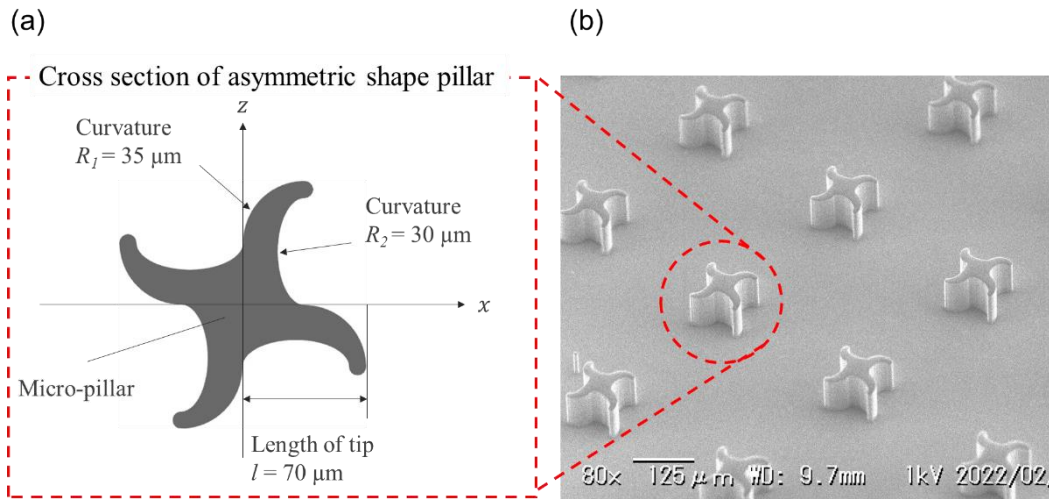


Fig. 4-8 (a) Schematic of a cross-section of the asymmetric (Ninja-star) shape. (b) SEM images of micropillars with asymmetric shape with the height $h = 100$ μm and pillar separation $S = 400$ μm.

Fig. 4-9 shows a comparison of streamlines induced around the asymmetric pillar with both CW and CCW directions, as observed through numerical simulation and experiment. For the circular vibration in the CW direction, four small vortices form inside the bent arms of the Ninja star (Fig. 4-9 (a, b)). Conversely, with CCW vibration, four vortices are induced far from the edge of the pillar (Fig. 4-9 (c, d)). These results suggest that the present simulation effectively reflects the effect of the vibration direction on the induced Lagrangian velocity field.



Fig. 4-9 Streamlines of the time-averaged Lagrangian velocity field around the asymmetric pillar under circular vibrations in (a, c) Numerical simulation and (b, d) experimental results. Experimental observation utilizes long-exposure particle imaging for fluorescent particles. Vibration directions are indicated by black or white arrows in each figure, representing either (a, b) CW or (c, d) CCW directions.

Next, we compare 2D vector plots of the Lagrangian velocity field around the asymmetric pillar between simulation and PIV measurement (Fig. 4-10). In both CW and CCW conditions, a local flow circulating the pillar is induced, similar to the cylindrical pillar condition. When the direction of vibration reverses, the rotational direction of the circulating flow also reverses. Additionally, the highest absolute velocity is concentrated near the tips of the four arms of the Ninja star, with the maximum velocity resembling that of a cylindrical pillar (~800 µm/s). These patterns are consistently observed in both the simulation and the experimental results, as illustrated in Fig. 4-10 (a, c) and Fig. 4-10 (b, d), respectively. The peak velocity around the asymmetric pillar, i.e., the averaged maximum velocity magnitudes near the four arms of the pillar, are compared between the simulation and experiment Fig. 4-10 (e). The results in the simulation exhibit quantitative agreement with the experimental one, and the simulation accurately predicts the trend of a larger Lagrangian velocity in the case of CCW rotation. Furthermore, the influence of three-dimensionality is nearly negligible in the case of circular vibration, despite the complex shape of the pillar.

In summarizing the comparison between simulation and experiment, the current simulation accurately reproduces the flow fields with both cylindrical and complex shapes under different vibration directions. Obtained simulation results are validated through experimental PIV measurements.

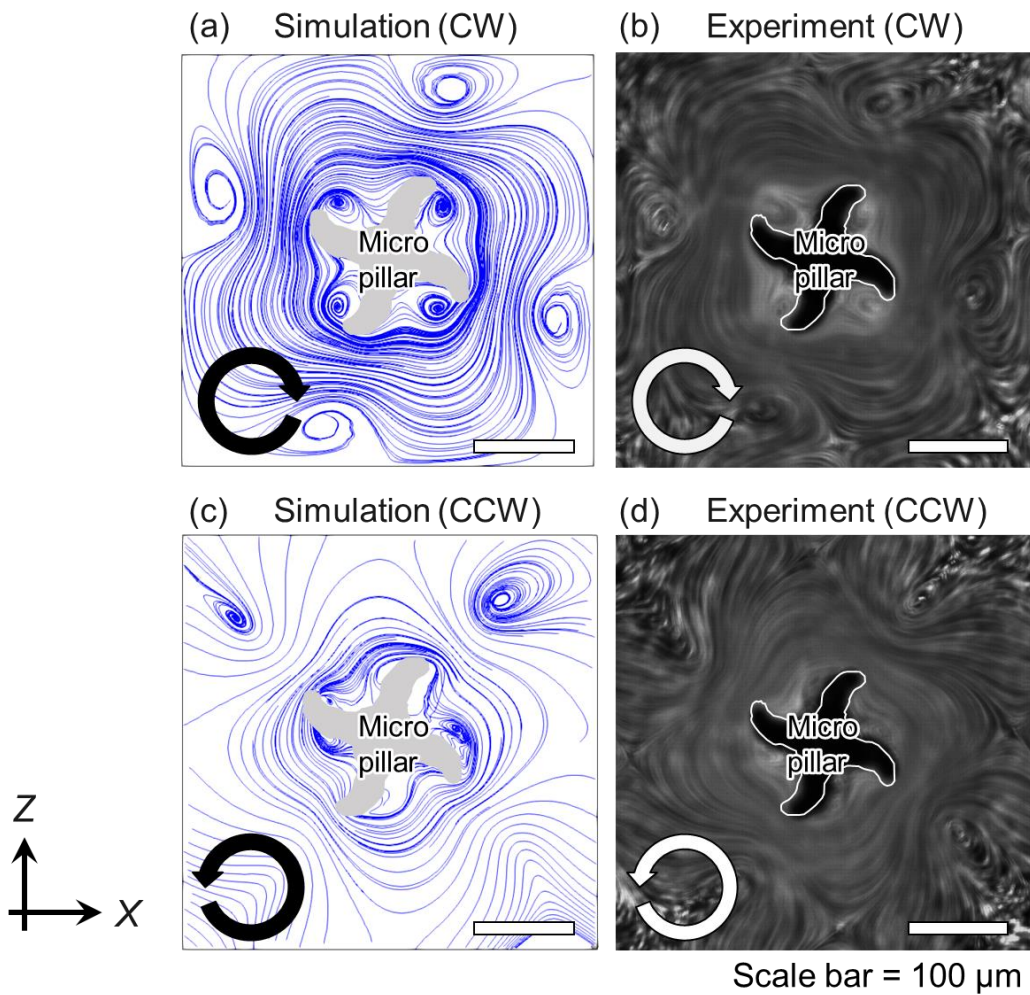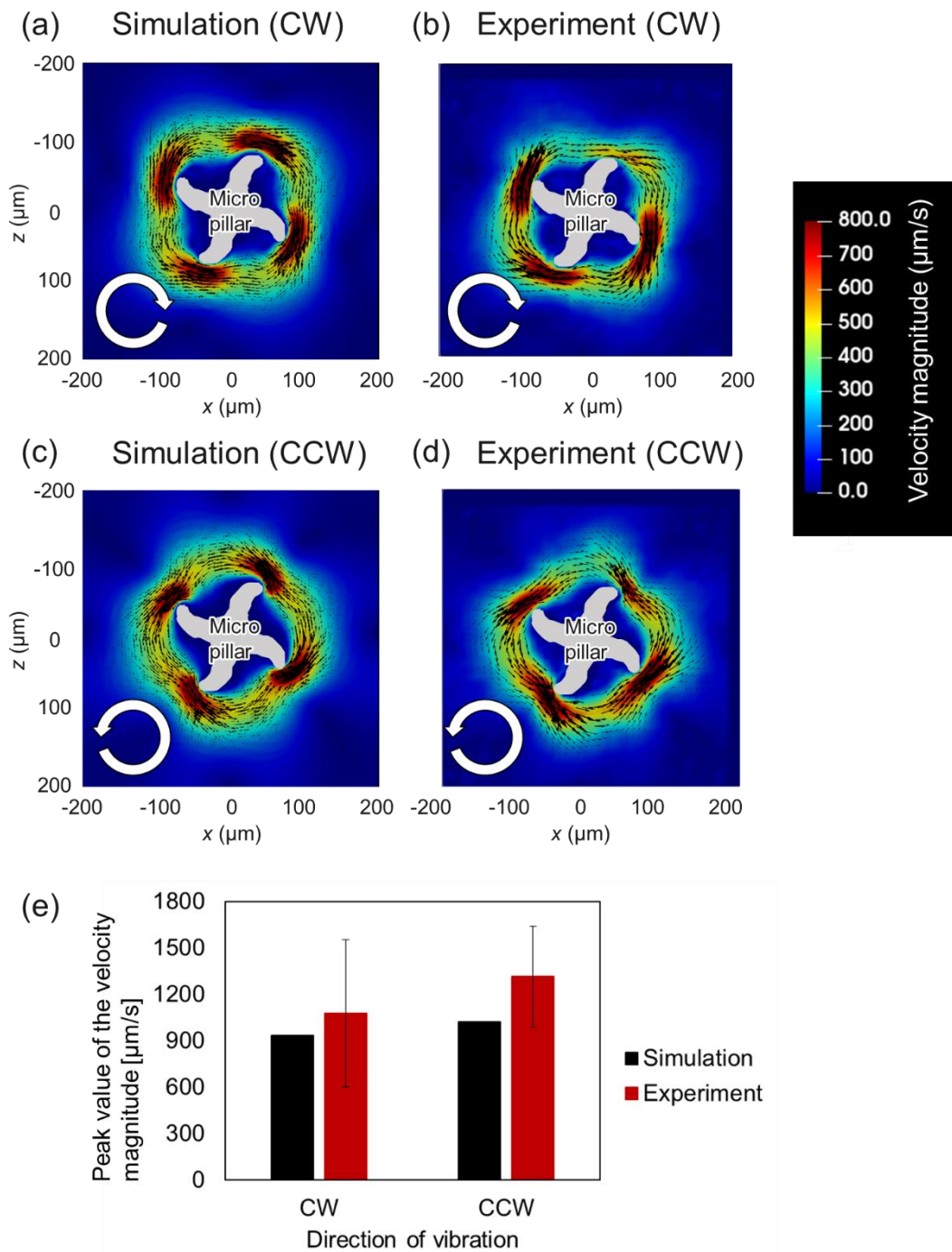Fig. 4-10 2D vector plots of the time-averaged Lagrangian velocity field around the asymmetric pillar under circular vibrations in (a, c) numerical simulation and (b, d) experiment. Vibration directions are specified as either (a, b) CW or (c, d) CCW. The white arrows in each figure indicate the direction of the vibration. (e) Peak velocity magnitudes around the asymmetric pillar.

## 4.4. Dependence of vibration parameters/pillar separation on the flow field

As described in Chapter 2, vibration parameters have impacts on the resulting flow field (Hayakawa et al. 2015) in the VIF. Here, the effects of frequency $f$, amplitude $A$, and pillar separation $S$ on the time-averaged Lagrangian velocity field are numerically investigated. Specifically, the frequency $f$ is varied as 100, 200, 400, 600, 800, and 1200 Hz with a constant $A = 3.3$ µm and $S = 400$ µm. In the second set of simulations, the amplitude $A$ is systematically changed as 1, 2, 3.3, and 6 µm under the constant $f = 600$ Hz and $S = 400$ µm. In the third set of simulations, the pillar separation $S$ is varied as 150, 200, 400, and 600µm under the constant $f = 600$ Hz and $A = 3.3$ µm.

Fig. 4-11 depicts radial profiles of the azimuthal velocity with dependence on $f$, $A$, and $S$. The velocity increases with the increment of both frequency and amplitude, indicating frequency and amplitude dependence. Regarding pillar separation, the velocity magnitude increases with an increase in pillar separation, and the velocity profile expands. Under conditions with $S = 400$ and 600 µm, the distribution remained largely unchanged.
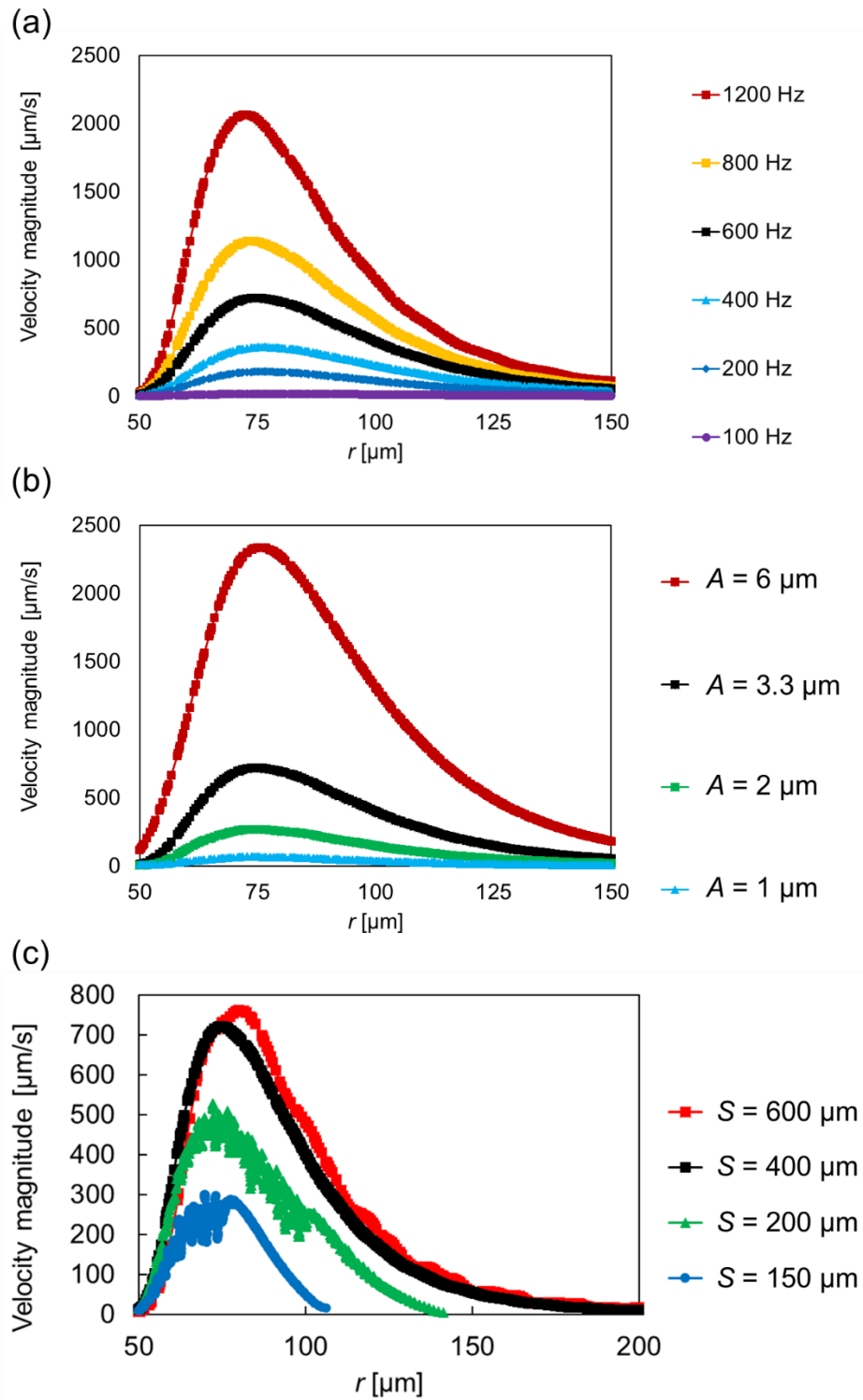
Fig. 4-11 Azimuthal velocity profiles as a function of the distance from the pillar center ($r$) with dependence on (a) frequency $f$, (b) amplitude $A$, and (c) pillar separation $S$.

The magnitude and the location of the maximum Lagrangian azimuthal velocity are quantitatively summarized in Fig. 4-12 (a, b), where the horizontal axis is the value of a normalized parameter which is unity when the frequency, amplitude, and pillar separation are $f_0$ = 600 Hz and $A_0$ = 3.3 μm, $S_0$ = 400 μm respectively.

The dependence of the frequency and the amplitude of the peak azimuthal velocity on these parameters shows similar trends to our previous theoretical analysis based on the 2D stream function equations (Hayakawa et al. 2015). Specifically, the peak velocity value increases monotonically and nonlinearly as $f$ and $A$ increase (Fig. 4-12 (a)). For the dependence of pillar separation, peak velocity magnitude increases as $S$ increases in the range where $S/S_0$ is lower than 1. Conversely, when $S/S_0$ is higher than 1, the velocity magnitude slightly increases with the increase of $S$.

The radial peak position (from the center of the pillar) of the Lagrangian azimuthal velocity profile is also depicted for each normalized parameter to characterize the shapes of the velocity profiles (Fig. 4-12 (b)). The result indicates that the peak position approaches the side wall of the pillar with increasing frequency. This tendency agrees well with our previous theoretical analysis (Hayakawa et al. 2015), which explained that the frequency dependency of the peak position can be explained by the Stokes boundary layer thickness, $\delta_s = \sqrt{2\nu/\omega}$, where $\nu$ and $\omega$ are the kinematic viscosity and angular frequency, respectively. On the other hand, the peak position moves away from the side wall of the pillar as both amplitude and pillar separation increase. This result should reflect the fact that an increase in vibration amplitude expands the flow field. Additionally, the flow field expands with a wider pillar separation due to the reduction of interference between adjacent pillars.

In summary, vibration frequency, amplitude, and pillar separation alter the magnitude of induced velocity in a similar manner, but the effects on the velocity profiles, especially on the boundary layer thickness, are different.
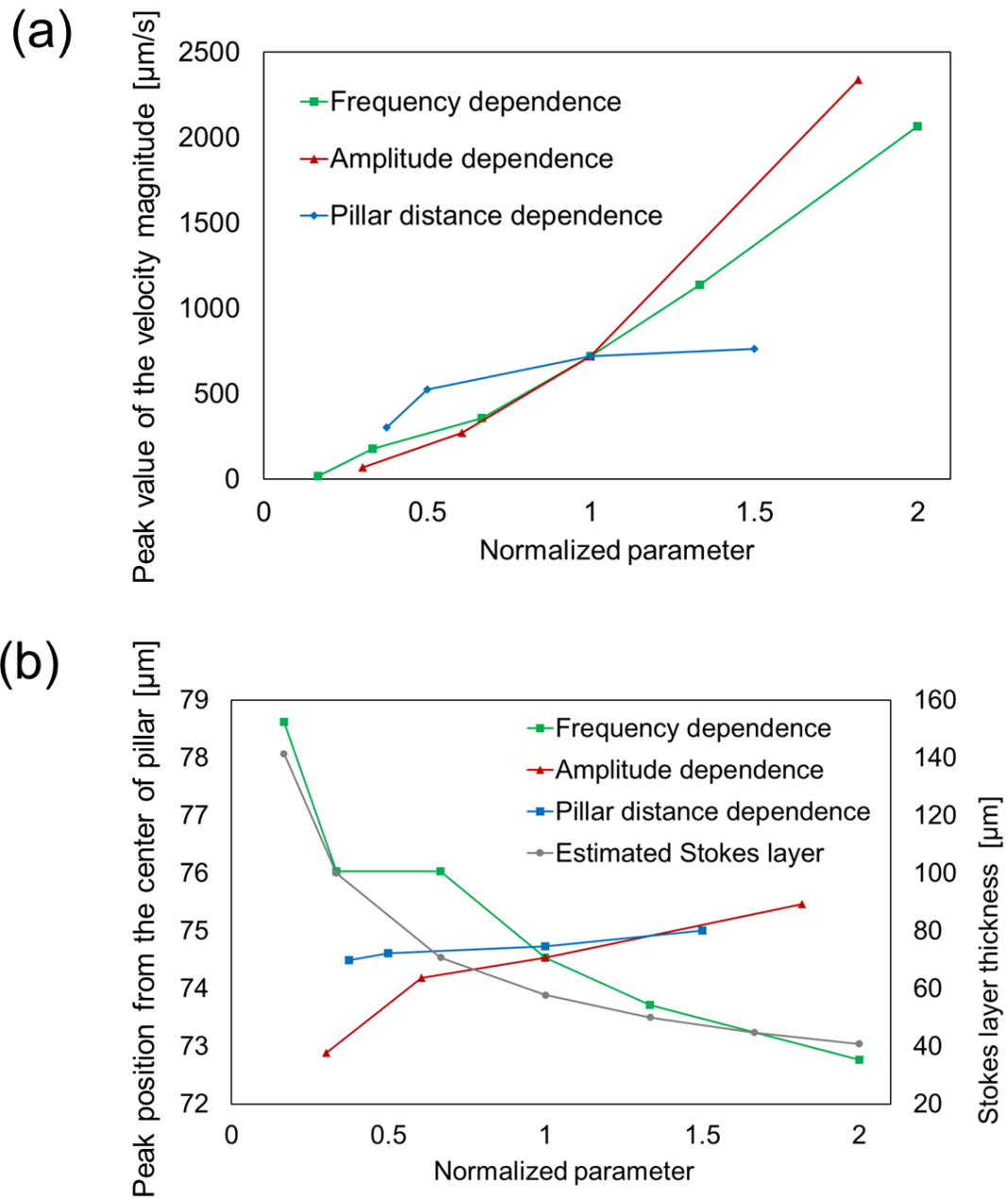
Fig. 4-12 (a) Relationship between the peak velocity magnitude and the vibration parameters (normalized frequency $f/f_0$, amplitude $A/A_0$, and pillar separation $S/S_0$). (b) Relationship between the peak position of the velocity profile (zero at the center of the pillar) and normalized parameters. The gray line in the panel represents the theoretical stokes layer thickness.

## 4.5. Particle capture simulation

Next, we conducted a numerical simulation of particle capture between CP/NP using particle tracking. The pillar separation of $S = 200$ µm and 400 µm was adopted which is used for NP detection in chapter 2. The vibration condition is set to $f = 600$Hz and $A = 3.3$ µm.

Fig. 4-13 shows snapshots before particle agitation in the computational domain in $S = 200$ µm and 400 µm conditions. Two kinds of particles are uniformly arranged in the $x$-$z$ and $x$-$y$ planes. To investigate the three-dimensional particle behavior induced by agitation, particles are placed within several different $x$-$z$ directions. Before agitation, the particles are initially located near the center of the computational domain. However, due to local vortex flows, particle advection occurred, resulting in both CP and NP becoming uniformly and randomly distributed within the computational domain (Fig. 4 14). Particle migration is induced due to local circular flows around the pillar, causing the CP/NP to disperse randomly throughout the domain (Fig. 4-14). Under both $S = 200$ µm and 400 µm conditions, particles exhibited three-dimensional motion, but under the $S = 400$ µm condition, a relatively large number of particles remained near the center of the computational domain. In contrast, under the $S = 200$ µm condition, most particles dispersed three-dimensionally without remaining confined to the initial horizontal cross-section. In the vector plots of Fig. 4-5, it appeared that there was little evidence of a three-dimensional flow field around the pillar subjected to circular vibration. However, particles exhibited three-dimensional advection with particle tracking simulation.
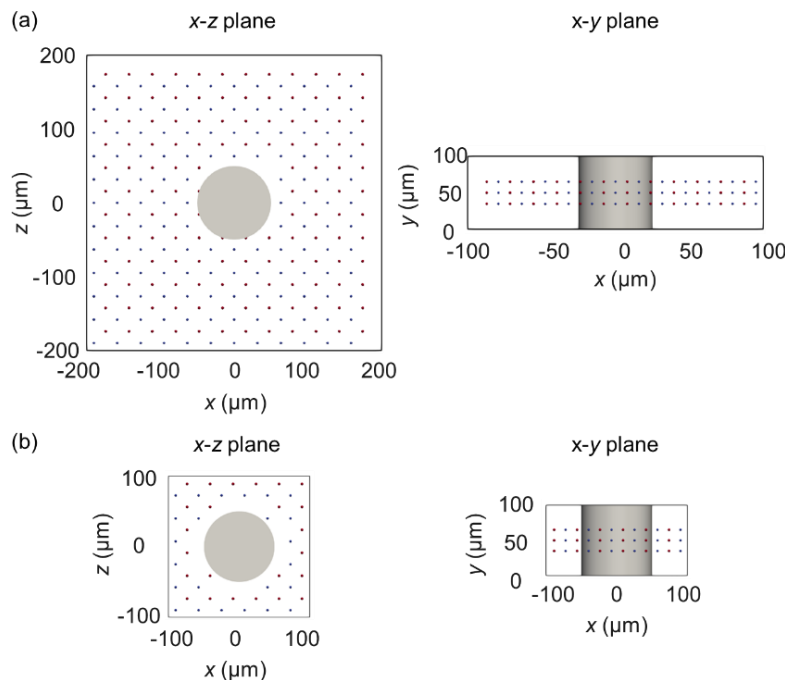


Fig. 4-13 Snapshots of the initial position of the particle tracking simulation. The tracer particles initially dispersed uniformly around the pillar. (a) $S = 400$ µm and $S = 200$ µm condition.
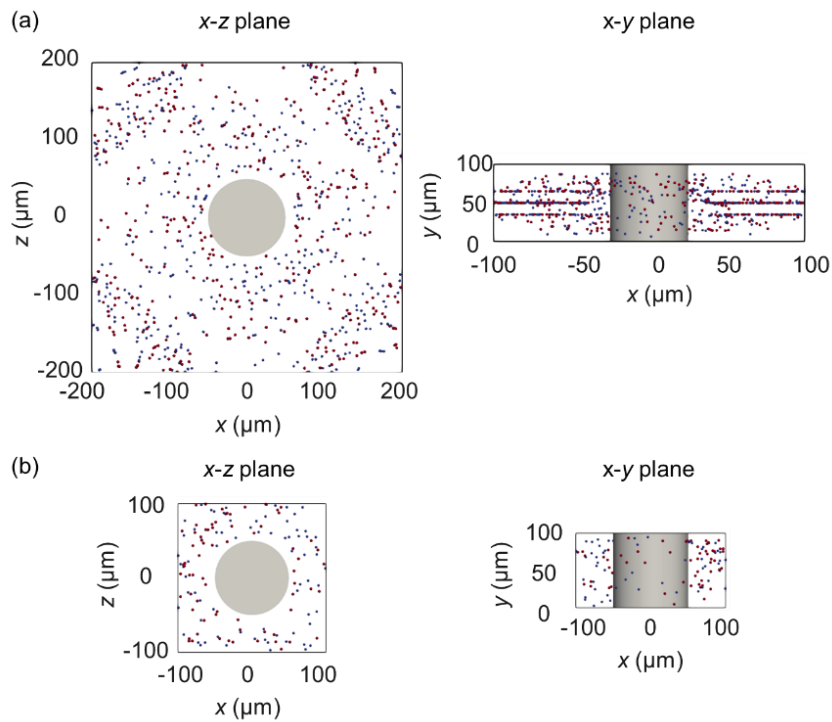
Fig. 4-14 Snapshots of the particle tracking simulation at 200s for stirring. (a) $S = 400$ μm and $S = 200$ μm condition. The vibration condition is set to $f = 600$ Hz and $A = 3.3$ μm. and PIV measurement. Error bars represent the standard deviation of triplicated trials.

Through the particle tracking simulations, we were able to visualize the three-dimensional behavior of particles. However, in the experimental particle dispersion environment, it is not feasible to freely control the arrangement of particles. Therefore, in numerical simulations as well, calculations are conducted with an initial configuration condition where particles are randomly positioned (Fig. 4-15 (a)).

Fig. 4-15 (b) shows the time course of the capture rate of target particles under the conditions of $S = 200$ μm and 400 μm, respectively. The error bars represent the standard deviation of the capture rate across three independent calculations. Over the agitation period of 0 to 200 s, the capture rate increases with time. Under the $S = 400$ μm condition, the capture rate reached approximately 20% at 200 s. Under the $S = 200$ μm condition, there was greater variability in the capture rate compared to the S = 400 μm condition, and the capture rate reached around 30% at the 200 s.
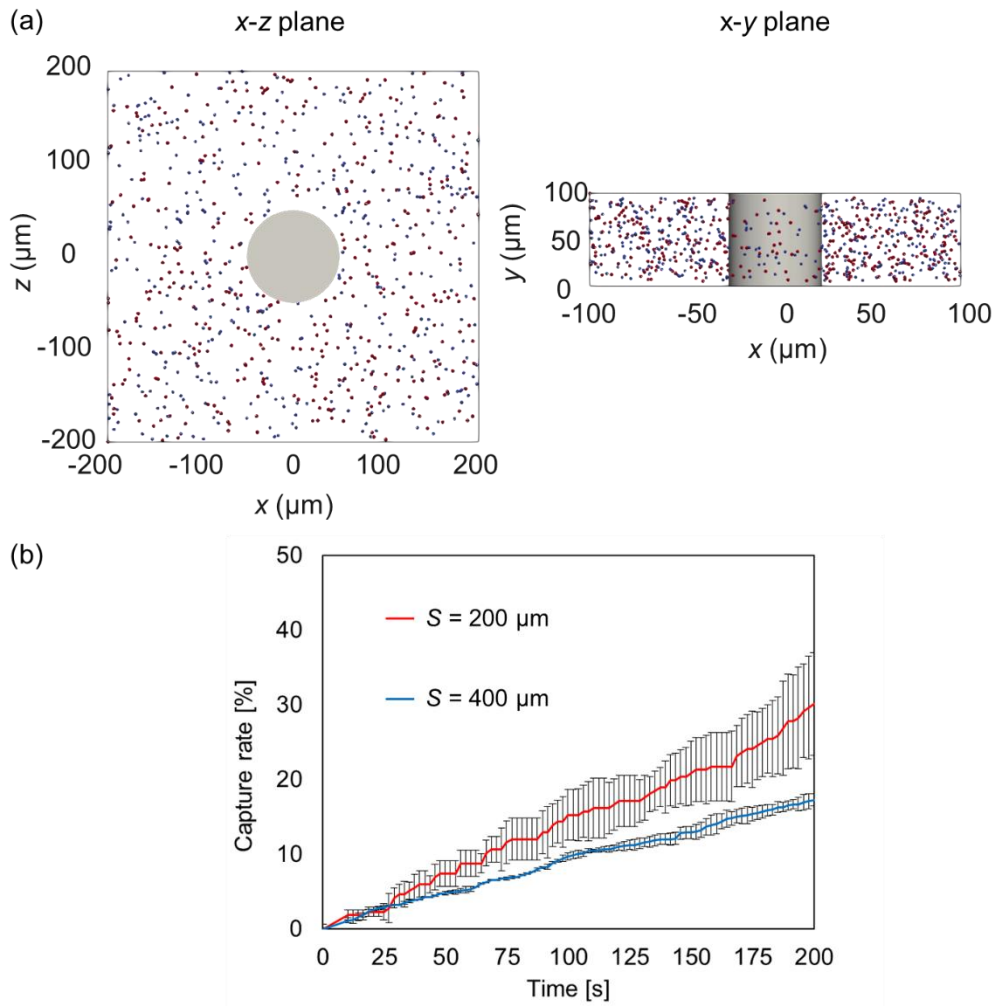
Fig. 4-15 (a) Snapshots of the initial position of the particle tracking simulation in $S = 400$ μm condition. (b) Time course of capturing rate of target particle. Pillar separation is set to (black and gray line) $S = 400$ μm and (red and orange line) $S = 200$ μm, with each $f = 600$ μm and $A = 3.3$ μm.

Next, we investigated the trajectories of a single pair of CP and NP to see how they collide under exploration in the computational domain. The vibration condition is set to $S = 200$ μm, $f = 600$ Hz, and $A = 3.3$ μm.

Fig. 4-16 shows the trajectory of the single pair of NP and CP. In the trajectory from the beginning of stirring (Fig. 4-16 (a)), the positions of NP and CP in the $x$-$z$ plane are initially separated. Examining the trajectory during the last 9.8 seconds leading up to the collision (Fig. 4-16 (b)), CP caught up with NP and collided with it. The time-evolution plot of $y$ ($t$-$y$ plot) until the collision (Fig. 4-16 (c)) depicts the three-dimensional particle behavior during advection from almost the same position. These results demonstrate that NP and CP, initially positioned at a distance from each other, undergo advection following a circular flow with three-dimensional motion and eventually collide.

87
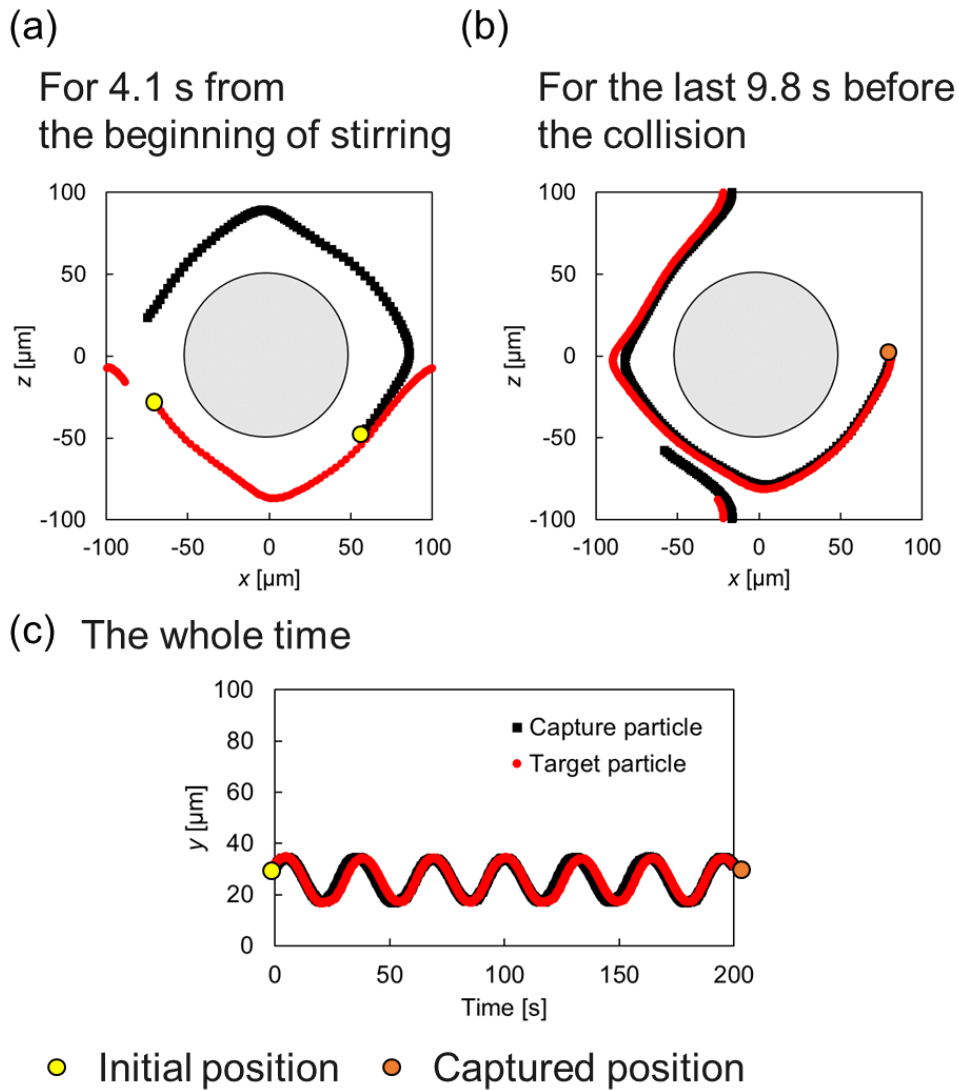
Fig. 4-16 Trajectory of the single pair of NP and CP. (a) The trajectory for 4.1 s from the beginning of stirring. (b) Trajectory for the last 9.8 s before the collision. (c) Time-evolution of $y$ ($t$-$y$ plot) until the collision. The vibration condition is set to $S = 200$ μm, $f = 600$ Hz, and $A = 3.3$ μm.

Subsequently, we examined the locations where the collision between NP and CP occurs at 200 seconds of stirring. Fig. 4-17 illustrates a capture point projected onto the $x$-$z$ plane and the temporal evolution of the $y$ capture position ($t$-$y$ plot). Under the $S = 400$ μm condition (Fig. 4-17 (a)), collisions predominantly occurred in the vicinity of the pillar sidewall. In the $y$-direction capture point, a tendency for captures in three-dimensional space randomly was observed. In the case of $S = 200$ μm condition (Fig. 4-17 (b)), a trend was evident that capture occurs randomly both in the $x$-$z$ plane and the $y$ direction.
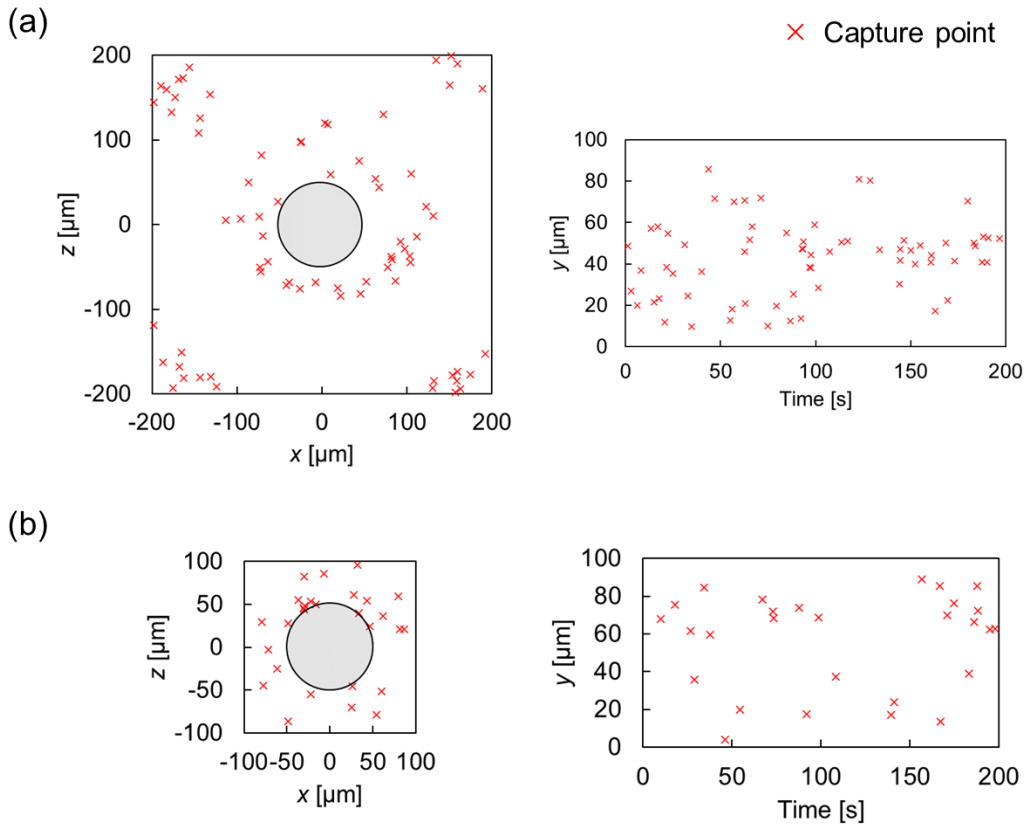
Fig. 4-17 Capture point after 200s for stirring in the condition of (a) $S$ = 400 μm and (b) $S$ = 200 μm condition. The vibration condition in each is set to $f$ = 600 Hz and $A$ = 3.3 μm.

### 4.5.1. Effect of the vibration conditions on capture rate

Next, the effect of various vibration conditions on the capture rate was investigated. Specifically, we examined the effect of vibration frequency, amplitude, and separation between pillars. Fig. 4-18 shows the relationship between the capture rate after 200 s for these vibration conditions. Regarding pillar separation dependence (Fig. 4-18 (a)), the capture rate increases as the pillar separation gets shorter. In addition, the variation of capture rate among the three calculations increases as the pillar separation gets shorter. In the case of different frequencies (Fig. 4-18 (b)), the capture rate increases as the frequency increases. Similarly, for the dependence of vibration amplitude (Fig. 4-18 (c)), the capture rate increases as the amplitude increases. Here, the capture rate with $S$ = 200 μm condition is also plotted in the panel. Similarly to Fig. 4-18 (a), a shorter pillar separation corresponds to a higher capture rate for all amplitude conditions.

89

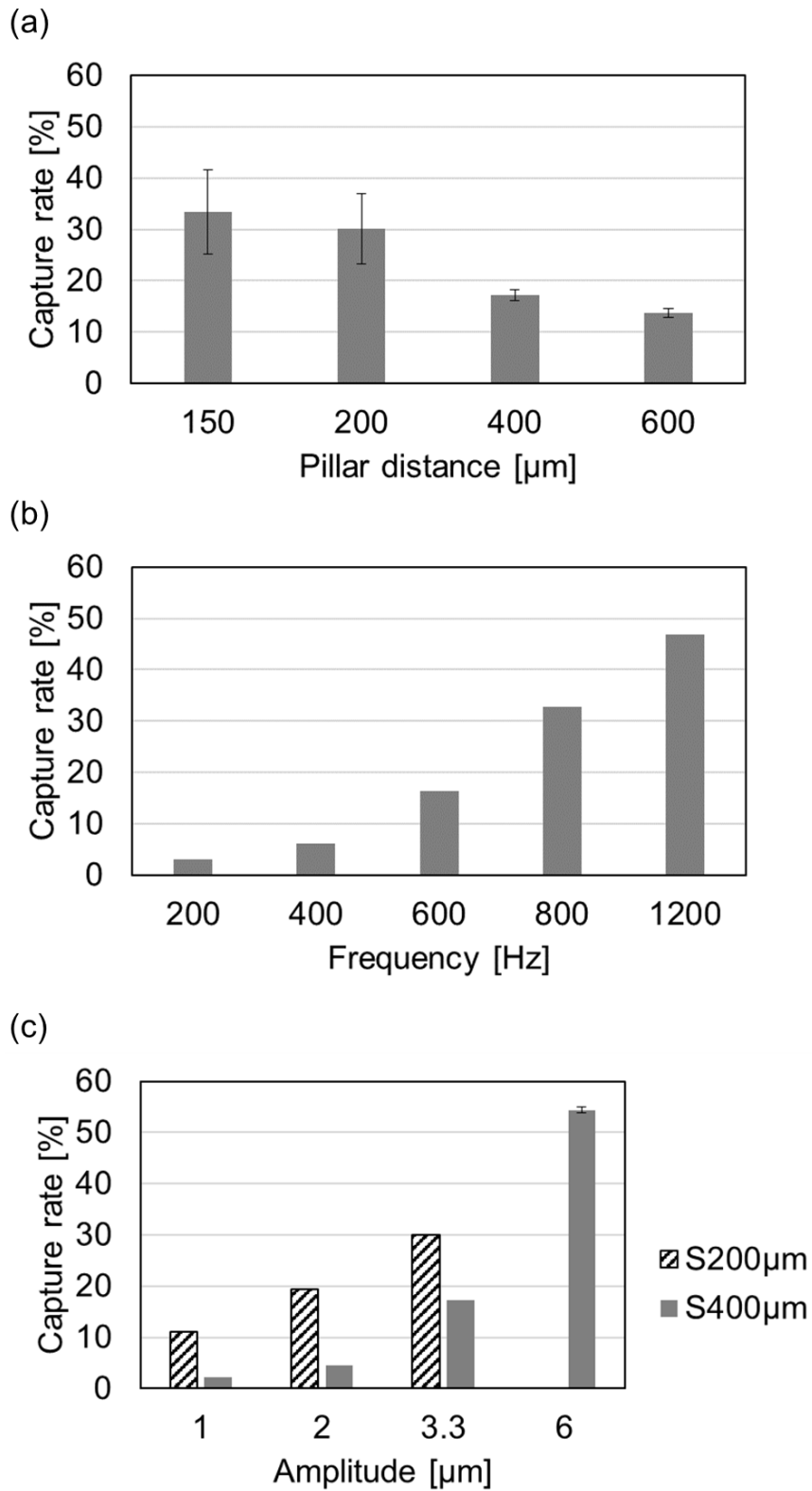Fig. 4-18 Relationship between capture rate and (a) pillar separation, (b) frequency, and (d) amplitude at 200s vibration.

Using capture rates and the vibration conditions presented in Fig. 4-18, we examine the relationship between capture rate and velocity magnitude, investigating the frequency and amplitude dependencies (Fig. 4-19). An escalation in velocity corresponds to an increase in both frequency and amplitude, as illustrated in Fig. 4-12 (a). Regarding the frequency and amplitude dependence (Fig. 4-19 (a)), the capture rate increases with the rise in velocity magnitude, observed across both frequency and amplitude. This result suggests that the capture rate is dependent on velocity, indicating an acceleration in particle collisions.
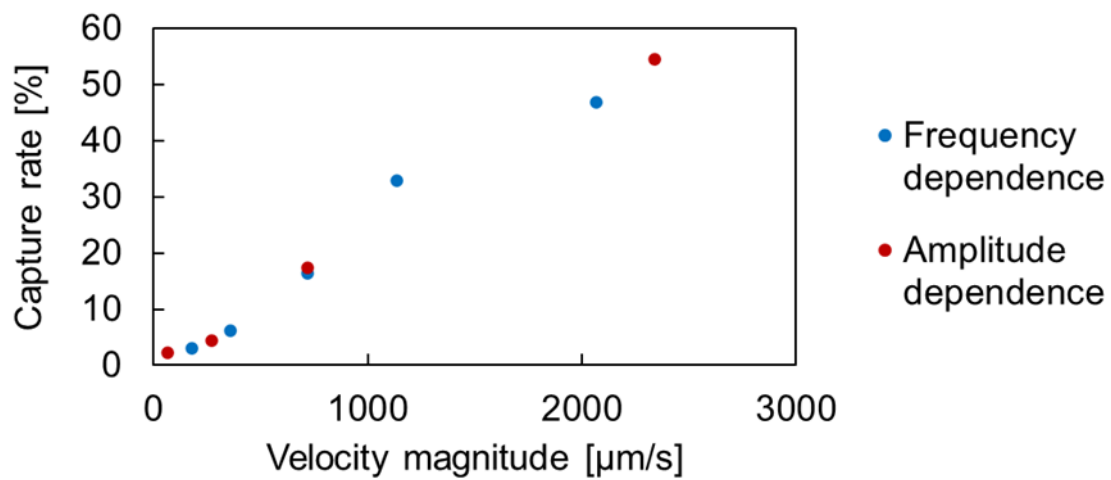


Fig. 4-19 Relationship between capture rate at 200s and velocity magnitude.

### 4.5.2. Correlation between numerical capture rate and experimental aggregate formation

Next, the relationship between the formation of aggregates observed in the experiments and the capture rate obtained from the numerical simulation was investigated. Fig. 4-20 shows the correlation between the averaged area of CP aggregates and the particle capture rate obtained in the experiment and numerical simulation, respectively. Fig. 4-20 (a) shows the relationship between the average area of CP aggregates in the experiment and the capture rate with frequency/amplitude dependence. They show a positive correlation. This suggests that particle capture and aggregate formation are facilitated in response to the increase in velocity.
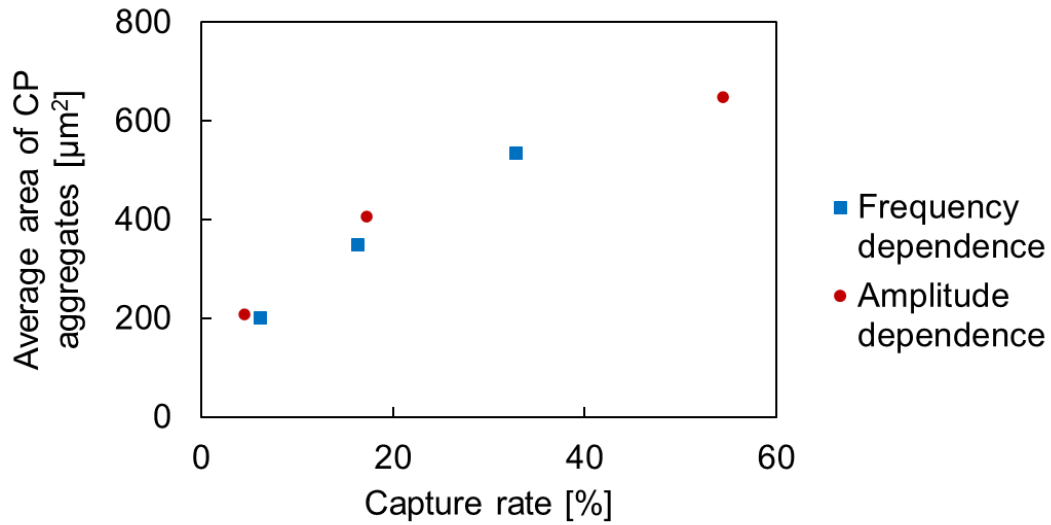
Fig. 4-20 Correlation between the averaged area of CP aggregates and particle capture rate obtained in experiment and numerical simulation, respectively.

### 4.5.3. Dependence on particle concentration

Finally, we investigated the dependence of NP concentration on the capture rate, to compare with the concentration dependence of the aggregation area in experiment results. Here, NP concentrations are set to $2.2 \times 10^7$ /mL, $1.1 \times 10^8$ /mL, $2.2 \times 10^8$ /mL, and $4.5 \times 10^8$ /mL, respectively (initial positions of particles are shown in Fig. 4-21). Particles are randomly dispersed throughout the entire computational domain. We employed the $S = 200$ µm condition, which exhibited a high collision frequency in the parameter study in Fig. 4-18. The vibration condition is set to $f = 600$ µm and $A = 3.3$ µm.

Fig. 4-21 Snapshots of the initial position of the particle tracking simulation in various NPs concentrations. The concentration of NPs is set to (a) $2.2 \times 10^7$ /mL, (b) $1.1 \times 10^8$ /mL, (c) $2.2 \times 10^8$ /mL, and (d) $4.5 \times 10^8$ /mL, respectively.

Fig. 4-22 (a) shows the time course of the capturing rate of target particles in various NP concentrations. There is no large difference in capture rates for any concentration. On the other hand, in a probability distribution of the number of attache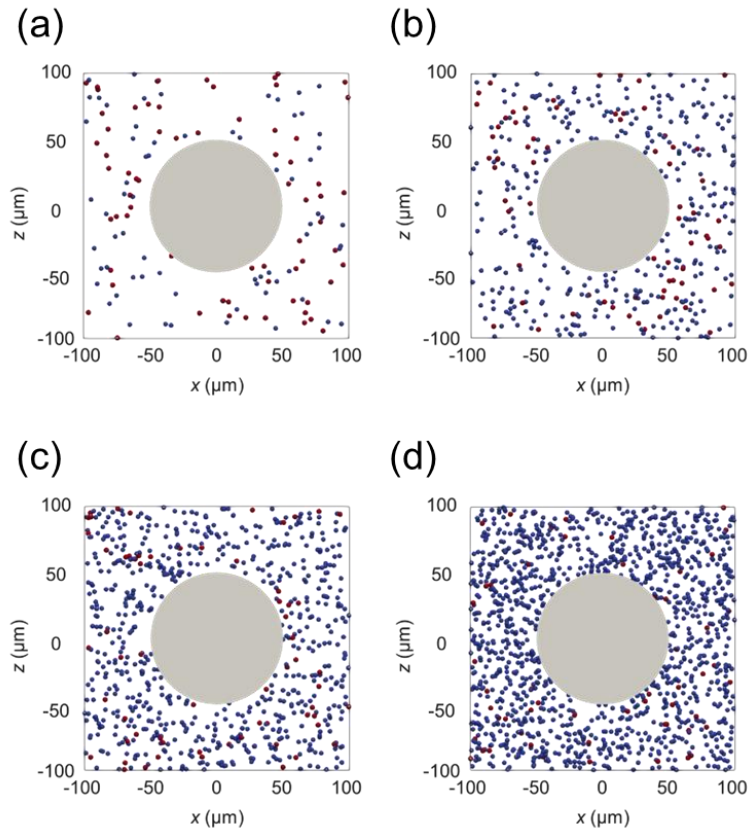d NPs to single CPs (Fig. 4-22 (b)), differences are observed in the distribution for each concentration condition. Under the condition of the lowest NP concentration of $2.2 \times 10^7$ /mL, the peak position in the distribution is zero, indicating that most CPs do not collide with NPs. As the NP concentration increases to $1.1 \times 10^8$ /mL, $2.2 \times 10^8$ /mL, and $4.5 \times 10^8$ /mL, the peak position shifts to the right, accompanied by a decrease in the normalized frequency.

Even with variations in NPs concentration, the capture rate remains unchanged in conditions where vibration conditions and pillar geometric conditions are constant. However, an increase in the NP concentration in the computational domain leads to the peak position shift in probability distribution. This shift is attributed to the increased number of NPs in the computational domain and the resultant higher frequency of collisions, leading to an increased number of attached NPs per single CP.

In this simulation, the CPs concentration is set to $2.2 \times 10^7$ /mL, which is of the same order as the experimental concentration of $3.3 \times 10^7$ /mL. Also, a peak shift in the probability distribution in the simulations was observed at NP concentrations greater than $1.1 \times 10^8$ /mL. In the experiments of aggregate formation, the dependence on aggregate area has been observed at concentrations around this order $1.1 \times 10^8$ /mL. Thus, concentration dependence in the simulation was confirmed at CPs/NPs concentrations of the same order as in the experiments. These results suggest that it is possible to predict not only the mere capture rate but also the extent to which NPs adhere to CPs, for the particle capture in the early stages of aggregation via the present simulation. This prediction is anticipated to contribute to the prediction of NP detection corresponding to CPs aggregate area.
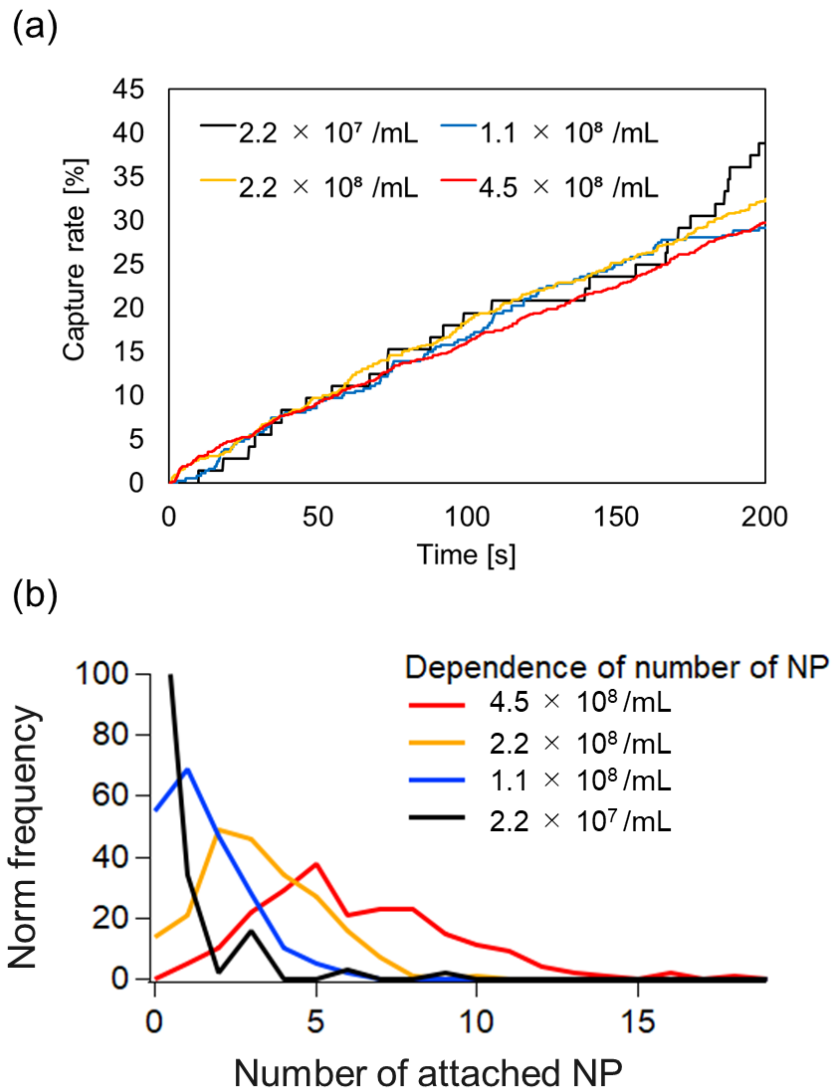


Fig. 4-22 (a) Time course of capturing rate of a target particle in various NP concentrations. (b) Probability distribution of number of attached NPs to single CPs.

## 4.6.  Summary of Chapter 4

To predict the particle capture phenomenon at the initial stages of aggregation, we performed a three-dimensional numerical simulation in various vibration conditions by extending our numerical model (Kaneko et al. 2018). The present numerical model enables the facile adjustment of vibration directions and amplitudes by modifying the conditions of the time-varying inertia force acting on the fluid, thus, we conducted a numerical simulation of VIF subjected to various vibrations. In addition, our simulation can implement complex 3D shape pillars by using the volume penalization method. Using the velocity field obtained in the simulation, we conducted fluid particle tracking to derive the Lagrangian velocity field, facilitating a direct comparison of the simulation results with the particle trajectories observed in our experiments.

First, we compare the flow field obtained in the simulation with experimental PIV measurements to validate the present simulation. In particular, we investigate the flow field around cylindrical and asymmetrical pillars. Vibration patterns are set to either circular or rectilinear vibration. For flow fields with cylindrical pillars under circular vibration, numerical results such as 2D vector plots and velocity profiles accurately reproduce experimental results similar to previous work (Kaneko et al. 2018). Second, we investigate the Lagrangian velocity field generated around a cylindrical micropillar under rectilinear vibration. This specific vibration pattern resulted in both influx and ejection flow parallel and normal to the vibration, respectively. The peak velocity magnitude of the ejection flow surpassed that of the influx flow. Third, we conducted a numerical simulation of the flow around a micropillar with an asymmetric cross-section. Our findings indicate that the Lagrangian velocity induced by CCW vibration surpasses that observed under CW vibration. This distinction holds promise for achieving adaptable mixing control by toggling between vibration directions, as described in a previous study (Hayakawa and Arai 2017). Our numerical tool exhibits promise for the precise quantitative prediction of VIF around complex pillar geometries. The trend of the flow field obtained with the simulation was reproduced by experimental measurements, validating the current numerical model.

Using the present simulation, we investigate the flow field around the cylindrical pillar under circular vibration condition, which is primarily employed in NP detection experiments. Specifically, we examined the influence of parameters such as vibration frequency, amplitude, and pillar separation. Notably, the frequency and amplitude significantly impact the velocity profile including velocity magnitude and peak position. The velocity magnitude increased with an increase in frequency, amplitude, and pillar separation. The peak velocity moved away from the pillar with increasing amplitude and pillar separation, while it approached with an increase in frequency.

Furthermore, we assessed the correlation between particle capture and the flow field around the micropillar. Assuming a capture system in an experimental environment, fluid particles are

randomly dispersed within the computational domain. With agitation, the capture rate increased over time. Additionally, we found that the capture rate is increases as velocity magnitude increases. We quantitatively compared particle capture in numerical simulations with the results of aggregation formation in experiments. In the simulation of particle capture, there is a correlation with the experimental trends in that the capture rate and average area of aggregates increase with an increase in frequency/amplitude. These results support that the CPs aggregate area in the aggregate formation experiments increases in response to velocity, which is attributed to an accelerated collision between particles with the increase in velocity. Our particle capture simulation enables us to predict not only the capture rate but also the trajectory until the collision and capture position in the 3D space. In summary, by using the constructed numerical simulations, we can elucidate the behavior of particle capture in the VIF system.

# Chapter 5.

# Detection of extracellular vesicles
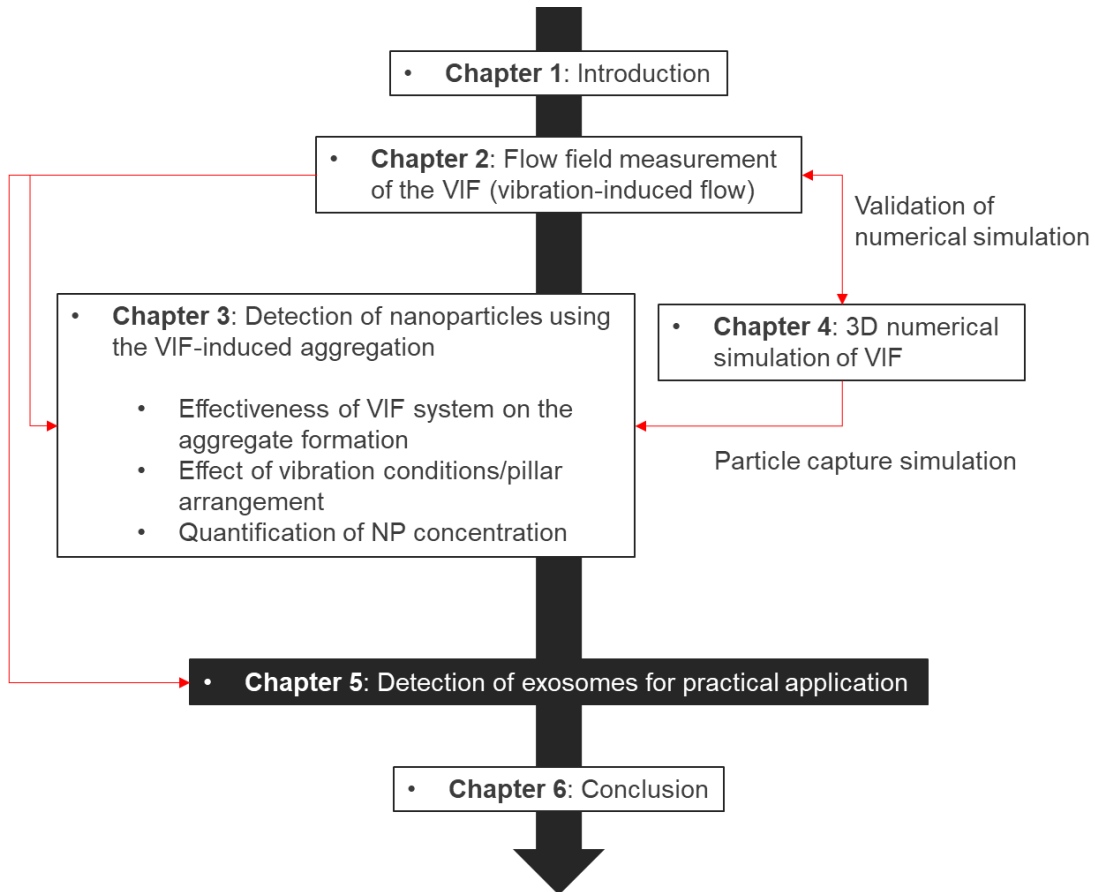
## 5.1. Overview

In Chapter 3, the effectiveness of our VIF system is demonstrated for detecting NPs using affinity CPs. However, its applicability in diagnostic scenarios remains uncertain, primarily due to the higher affinity between avidin and biotin compared to other biological affinity-capture systems. Consequently, we further conducted experiments to evaluate the performance of the system in detecting extracellular vesicles (EVs), important biological NPs existing in body fluids. First, we assess the capability of VIF to detect EVs. The subsequent stage involves examining the potential of the VIF system for quantifying EVs. Here, we chose pillar geometry for the following experiments with $h = 50$ μm and $S = 200$ μm for proof of concept.

## 5.2. Experimental procedures

### 5.3.3. Preparation of EVs and magnetic CPs.

We used EVs derived from bovine milk (EXBM100L, Cosmo Bio, Co., Ltd., Japan) for the test sample. To minimize nonspecific adsorption of EVs, a 100-fold dilution of EV blocking polymer reagent (EV-save) (058–09261, FUJIFILM Wako Pure Chemical Corp., Japan) was introduced to the original EV sample and was gently stirred at 10 rpm for 15 min. As a capturing system of EVs, we used Tim-4 conjugated magnetic CPs (297-79701, FUJIFILM Wako Pure Chemical Corporation, Japan) according to the protocol of the manufacturer. These CPs exhibited an affinity for phosphatidylserine on the EV membrane (Fig. 5-1). In brief, CPs conjugated with the Tim-4 were washed twice using washing buffer including 0.5 mL buffer, 4.5 mL ultrapure water, and 50 μL EV binding enhancer containing $Ca^{2+}$ ions. The magnetic CPs suspension was centrifuged and was then placed on a magnetic stand for 1 min to separate the CPs from the supernatant, which was subsequently removed. Followingly, 40 μL PBS buffer containing 0.125 w/w% BSA and 0.0025 w/w% Tween-20 was introduced to a microtube containing the washed Tim-4-conjugated magnetic CPs. After adding 30 μL EV solution to the microtube, a 10000-fold diluted binding enhancer solution containing $Ca^{2+}$ ions was introduced to the mixture. This concentration of binding enhancer was selected to facilitate the binding of EVs and Tim-4 with minimized nonspecific aggregation of magnetic CPs.
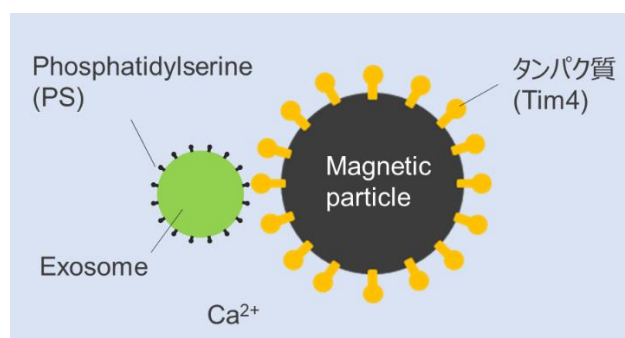
Fig. 5-1 Schematic of binding between phosphatidylserine (PS) on the surface of exosome and Tim4-coated magnetic CPs.
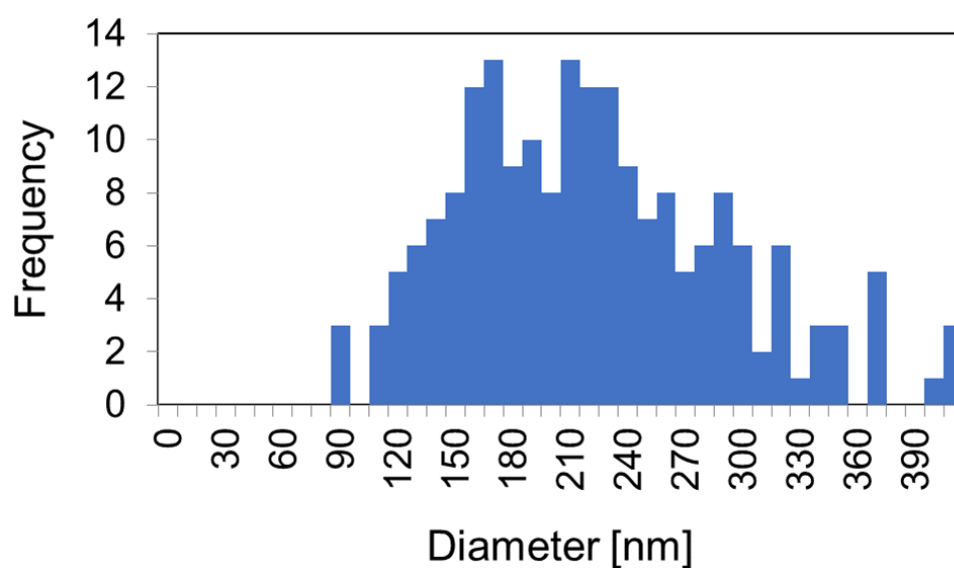


Fig. 5-2 Size distribution of milk-derived EVs measured using an imaging analyzer.

### 5.3.3. Installation of a mixture including EVs and magnetic CPs

The mixture containing magnetic CPs and EVs was gently pipetted 10 times to achieve uniform dispersion in the microtube. The surface treatment of the PDMS substrate and cover glass was performed to prevent nonspecific adsorption of EVs and magnetic CPs to them. In practice, the substrate and cover glass were coated with 0.5 wt% ethanol solution of a phospholipid-mimic polymer (Lipidure-CM5206, NOF Corp., Japan) for 3 min and were subsequently dried on a hotplate at 40 °C. Five µL of the mixture was placed onto the center of the substrate, then, the substrate was covered with the cover glass (Fig. 5-3).

O₂ plasma treatment:
(3min)

PDMS micropillar substrate

Phospholipid-mimic polymer coating:
incubated for 4 min, and dried on a
hotplate at 40 °C

Sample apply:
Mixture containing
the EVs and capture MPs

Covered with cover glass
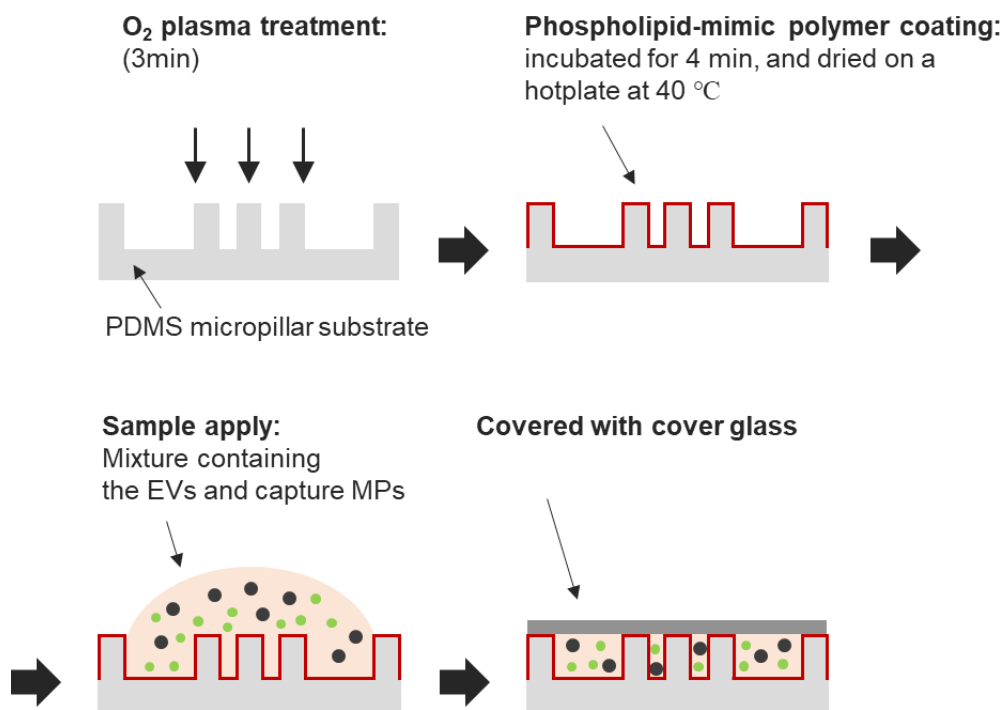
Fig. 5-3 Schematic illustration of application of sample including NPs and CPs to the substrate.

## 5.3. Effectiveness of magnetic CPs aggregation

We experimentally validate the effect of VIF on EVs-mediated aggregation of magnetic CPs. First, we performed preliminary examinations using vortex mixing. In the case of bulk vortex mixing in a test tube at 500 rpm instead of VIF, aggregates were not formed even after 1 h of mixing (Fig. 5-4).

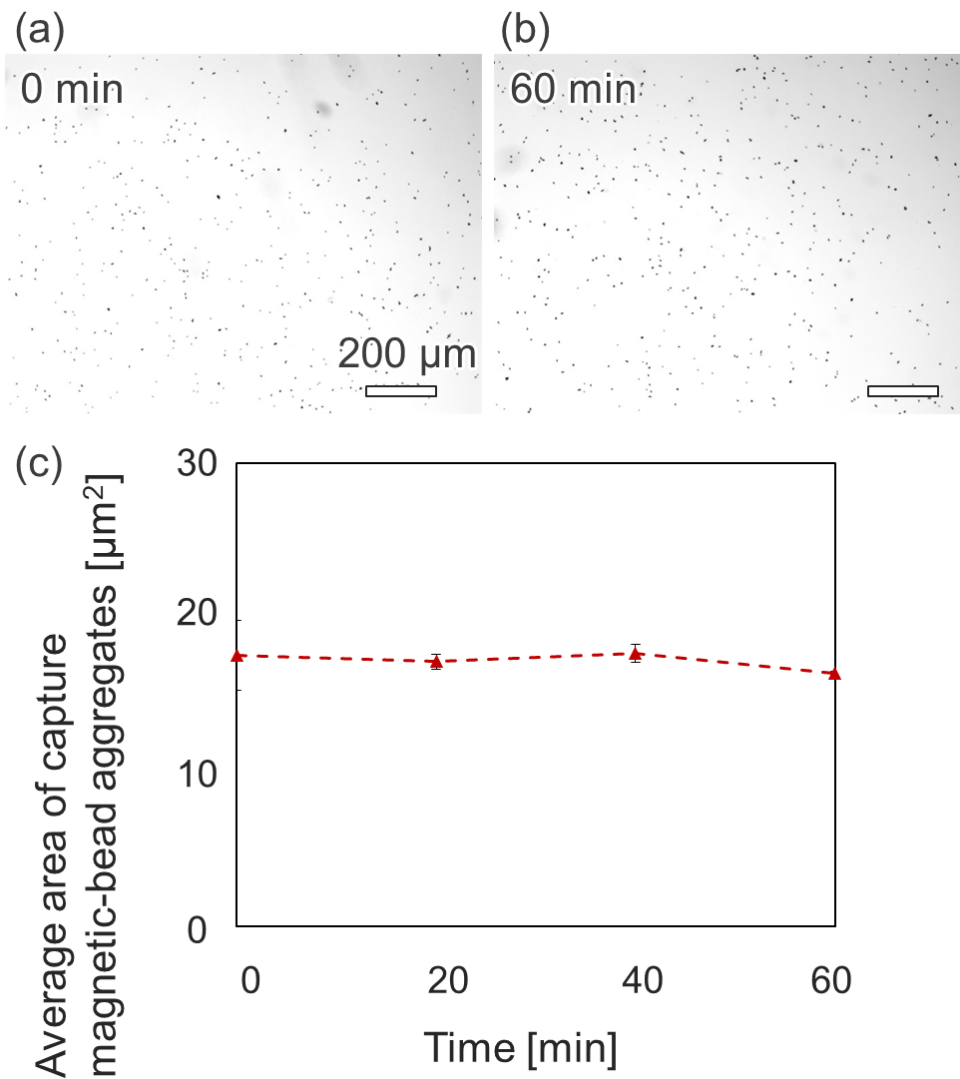Fig. 5-4 Microscopic bright images of particles taken at (a) 0 min and (b) 60 min of vortex mixing, with concentrations of EV and magnetic CP were $6.4 \times 10^9$ /mL and $1.5 \times 10^7$ /mL, respectively. (c) Time evolution of the average area of magnetic CP aggregates in vortex mixing. The stirring condition for vortex mixing was set to 500 rpm. Error bars indicate the standard deviation from triplicate experiments.

Next, we examined the effectiveness of our system. The circular vibration conditions were set to $f = 500$ Hz and $A = 5.2$ μm. We used this larger amplitude than that of the previous NP detection experiment because magnetic CPs were heavier, making their movement along the flow more difficult compared to polystyrene CPs.

Fig. 5-5 represents bright-field images around the micropillar taken at 0 and 15 min of vibration. At 0 min (before applying the vibration), the magnetic CPs were uniformly dispersed. However, after vibration for 15 min, many aggregates were induced (Fig. 5-5 (a), bottom panel). As part of the control experiments, we conducted experiments with no VIF and EVs ((Fig. 5-5 (b, c)). We found a similar trend in the results to those of the experiments involving the avidin–biotin capturing model system. In the case without VIF, magnetic CPs aggregate was not induced. In addition, the size of magnetic CPs was small in the absence of EVs. These results indicate that a local flow around the micropillar effectively induced aggregates of magnetic CPs only when there was an affinity between the target EVs and the CPs.
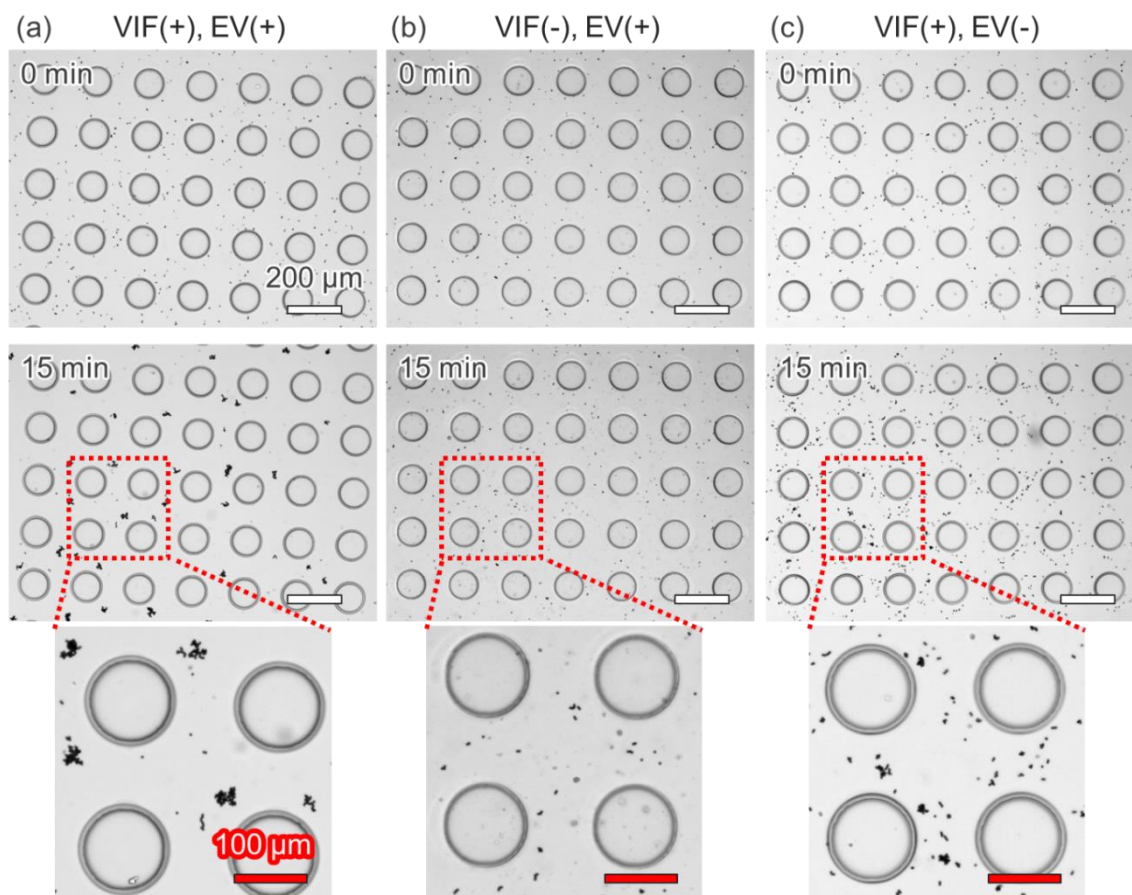


Fig. 5-5 Microscopic bright images of Tim-4 conjugated CPs taken at 0 min and 15 min of VIF: (a) VIF(+), EV(+), (b) VIF(–), EV(+), and (c) VIF(+), EV(–). In the VIF(+) cases, the vibration conditions were: $f = 500$ Hz and $A = 5.2$ μm.

## 5.4. Quantification of EVs concentration

The time evolution of the average area of the magnetic CPs aggregates is shown in Fig. 5-6. Upon applying vibrations to the micropillar substrate on which the sample containing EVs and CPs was placed, the average aggregate area exhibited an increase over time in all concentrations of EVs ($6.4 \times 10^9$ /mL, $1.28 \times 10^9$ /mL, $6.4 \times 10^8$ /mL, $6.4 \times 10^7$ /mL). Beeswarm plots of the CP aggregates area after 15 min at each EV concentration are presented in Fig. 5-7. The size of the aggregate showed minimal growth in the control experiments without NPs (black line), indicating that aggregation was induced by adsorption between EV and magnetic CP.
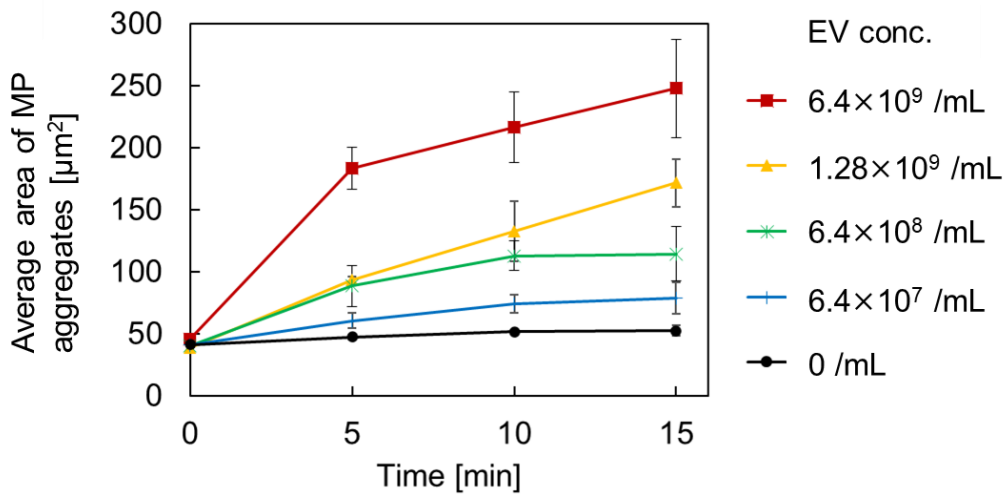


Fig. 5-6 Time evolution of the average area of aggregates with various EV concentrations.
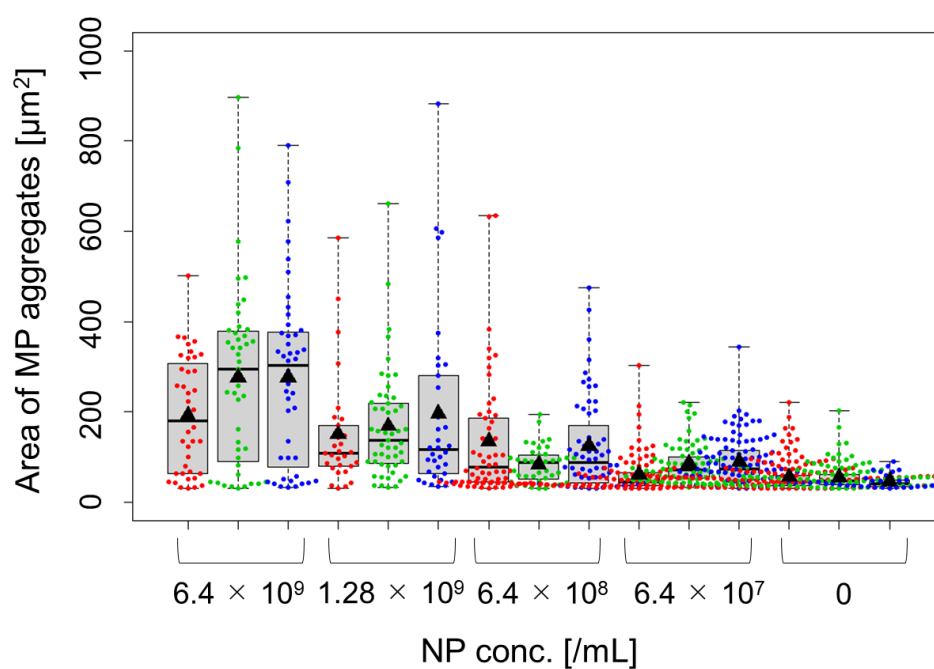
Fig. 5-7 Beeswarm plots illustrating magnetic MP aggregate area at 15 min for each EV concentration. (The results presented here are from triplicated experiments.)

Finally, we investigated performance in EVs detection based on Fig. 5-6. The relationship between the EVs concentration and the slope of the time-dependent increase in the CP aggregates area is shown in Fig. 5-8. We found that the average area of CP aggregates after 15 min of vibration increased as EV concentration increased, similar to the case of avidin–biotin capturing system. Based on linear regression analysis, a fitting equation of $y = 2.3329 \log x - 40.754$ with an $R^2$ value of 0.8722 was obtained. LOD in this system was calculated at $6.4 \times 10^7$ /mL (Table 5-1).

Fig. 5-8 Relationship between the slopes of the time-dependent increase of aggregate size (0–10 min) and the EV concentrations. Error bars indicate the standard deviation from triplicate experiments.
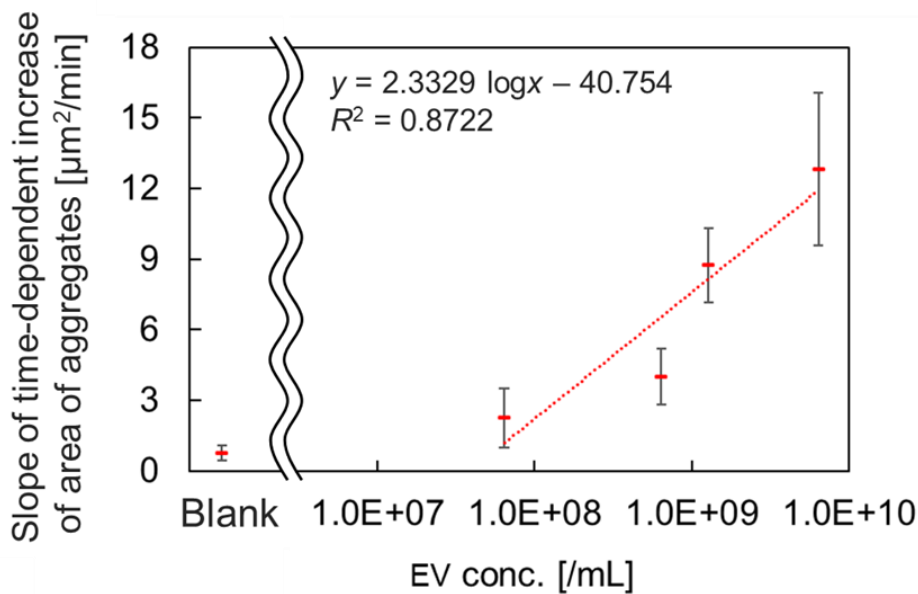
Table 5-1 Detection performance in EVs-Tim4 capturing system.

| Capturing system ($h$ = 50 μm, $S$ = 200 μm) | EVs-Tim4 capturing |
|---|---|
| Resolution | 0.52 μm$^2$ |
| Sensitivity (slope of the calibration curve) | 2.3329 |
| $R^2$ (coefficient of determination) | 0.8722 |
| Limit of detection (LOD) | 8.2 × 10$^7$ /mL |

## 5.5.   Summary of Chapter 5

In this chapter, we examined the practical diagnostic potential of this system using a commercial EVs capturing approach. Similarly to findings from the model NP capturing system, the VIF facilitated the aggregation of magnetic CPs, allowing for the quantification of EVs concentration. This chapter describes microscopic bright images illustrating the development of aggregates following

15 minutes of vibration, affirming the successful capture of EVs. Control experiments conducted without vibration, without EVs, and with bulk vortex mixing highlight the specificity of the magnetic CPs aggregation induced by the VIF system. Additionally, this chapter assesses the quantification performance of EVs by analyzing the time-dependent changes in the average area of magnetic CPs aggregates. The results exhibit a correlation between the increasing slope and EVs concentration, underscoring the capability of our method.

In both instances, involving the avidin-biotin and EVs-Tim4-serine capturing systems, the LOD in the current system was within the range of $10^7$ /mL. While the dissociation constants ($K_d$) for the avidin–biotin and Tim-4-serine systems are $10^{-15}$ M and $10^{-9}$ M (Miyanishi et al. 2007), respectively, the dynamics of aggregate formation demonstrated similarity under comparable vibration conditions. The detailed elucidation of the relationship between the strength of affinity and the dynamics of aggregate formation is a subject for future investigation. Nevertheless, this study suggests that the adaptability of the VIF system in fine-tuning flow conditions is beneficial for diverse detection targets.

# Chapter 6.

# Conclusion
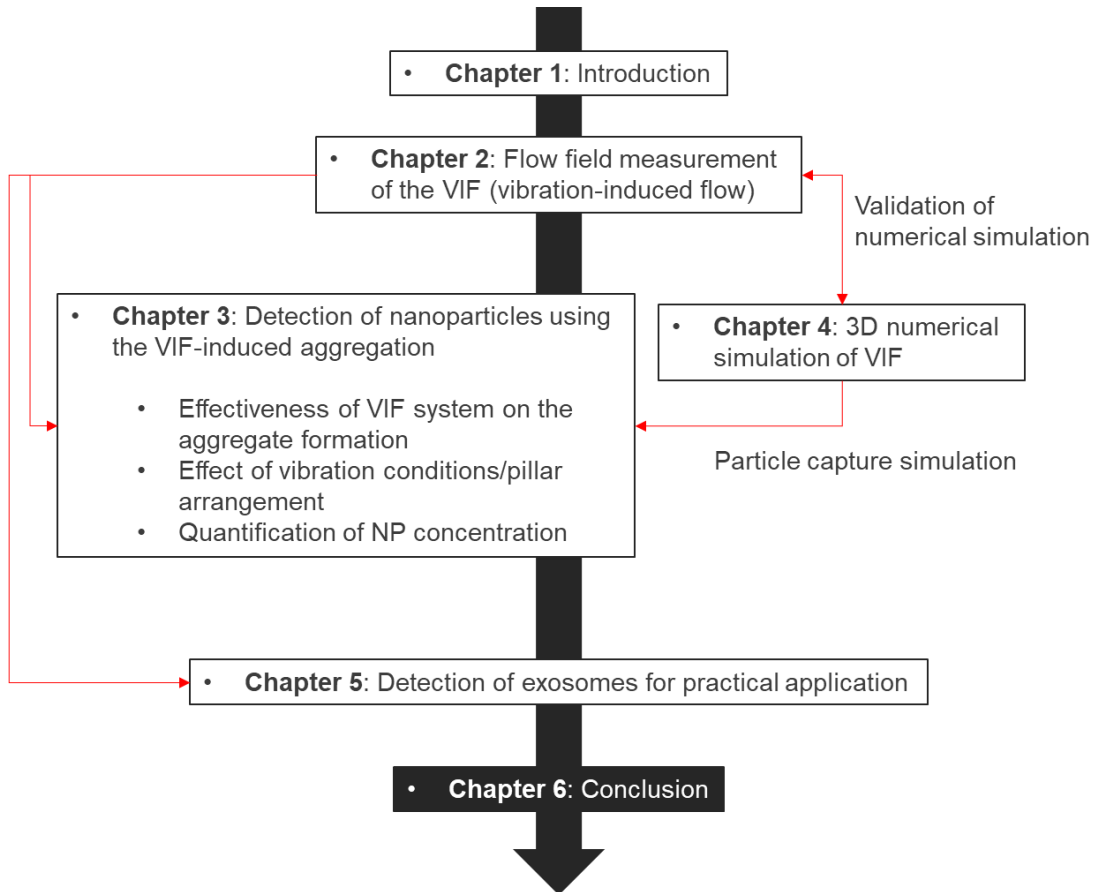
## 6.1.  Accomplishments

In this thesis, we employed the VIF to establish an immunoagglutination assay platform for NPs detection in minute samples. The fabrication of molds and PDMS micropillar substrates, utilizing the DRIE and replica molding processes, allows for the facile creation of various pillar geometric patterns. There is a scarcity of studies precisely measuring VIF flow fields under various conditions. Thus, we investigated the VIF flow fields under various conditions using the PIV technique. The results revealed substantial variations in the flow fields based on both pillar geometric conditions and vibration parameters.

Subsequently, we applied VIF to perform immunoagglutination-based NPs detection. Initially, as a proof of concept, we utilized the avidin-biotin interaction to form CPs aggregate. Efficient aggregation occurred when target NPs were present in a sample, validating the effectiveness of aggregate formation induced by VIF. While aggregates were formed through stirring in VIF, no distinct aggregates were observed using traditional mixing methods such as vortex mixing or rotational agitation, suggesting that microscale stirring facilitates a more rapid and effective particle encounter compared to diffusion or bulk agitation. We further examined the relationship between flow fields and aggregate formation, specifically investigating the impact of pillar geometric conditions and vibration conditions. We observed that employing larger pillar geometric conditions led to the formation of relatively larger and uniform aggregate. In the context of NP detection, we quantified NPs based on the aggregate area by constructing a calibration curve derived from the initial slope of a time-dependent increase in the aggregate area. Larger pillar geometric condition exhibited improved sensitivity, $R^2$, and LOD, highlighting the capability to fine-tune detection performance through physical parameters of VIF. Our system achieved an LOD of approximately $10^7$ /mL within 15 min. This LOD demonstrates improvement of detection performance 10 to 100 times compared to previous studies that determined macromolecular concentrations using aggregation-based detection systems (Han et al. 2007b; Gupta et al. 2012; Wu et al. 2015; Castro et al. 2018; Pawan et al. 2018). Additionally, our processing time is 2 to 3 times faster than the aforementioned studies.

Furthermore, toward a numerical understanding of particle behavior in the VIF system, we have constructed a numerical tool to predict the 3D flow field and particle transport. We thoroughly validated this tool by comparing various flow fields with PIV measurements conducted under identical vibration conditions. In pursuit of NPs detection using VIF-mediated aggregation, we assessed the dependence of particle capture and the characteristics of flow around the pillars through numerical simulations. When fluid particles were randomly arranged around the pillars, the capture rate was found to increase with the increase in velocity. These findings suggest the potential for accelerating

and enhancing the performance of NPs detection by optimizing fluid properties in the aggregation method using VIF.

Finally, we applied our system to detect EVs for practical application. Similar to the avidin-biotin capturing system, the formation of aggregates was observed when target EVs exited in the sample. The aggregate area varied with concentration, allowing for quantification at concentrations on the order of $10^7$ /mL. Although an investigation is needed of the relationship between the dissociation constants and aggregate formation in the avidin-biotin and EVs-Tim4 capturing systems, the high controllability of VIF has been demonstrated, enabling the detection of various targets.

In summary, our study achieved detection performance comparable to that of a commercial ELISA kit (Xu et al. 2018b) without the need for probe labeling and with significantly reduced processing time. Unlike some previous microfluidics-based systems employing RT-qPCR (Shao et al. 2015b) or aptamer-based fluorescent probes (Xu et al. 2018b) that may outperform in detection performance, our system stands out for its simplicity and cost-effectiveness (Table 6-1). It requires only a one-step procedure, no expensive reagents, a bright-field microscope with low magnification, and straightforward image processing. This system proves particularly suitable for situations demanding frequent measurements with relatively high detection performance, such as post-operative monitoring, infectious disease surveillance, and environmental monitoring. Moreover, we anticipate that the VIF-based approach will expedite and enhance the detection capabilities of other immuno-aggregation systems reported previously (Baksh et al. 2004; Han et al. 2007b; Gupta et al. 2012; Wu et al. 2015; Castro et al. 2018; Pawan et al. 2018) by introducing microscale local stirring to augment aggregate formation. Thus, the VIF system offers a potent addition to the array of NP detection methods based on affinity capture principles.

Table 6-1 Comparison of characteristics between proposed method and existing methods.

| | Time | Sensitivity (LOD) | Cost | Sample volume |
|---|---|---|---|---|
| RT-qPCR [29] | 2 h | ~$10^8$ /mL | High | 100 μL |
| Aptamer-based fluorescence probes [12, 27] | 20 min | ~$10^5$ /mL | High | 10 μL |
| Aptamer-based fluorescence probes [28] | 60 min | $4.39 \times 10^3$ /mL | High | 30 μL |
| Immunoagglutin ation [37] | 10 min | ~$10^{12}$ /mL | Low | 10 μL |
| Our method (VIF-facilitating immunoagglutin ation) | 15 min | ~$10^7$ /mL | Low | 5 μL |

## 6.2. Future work

In this study, we developed a VIF-based NP detection system using the immunoagglutination method. In a demonstration of detecting target NPs using avidin-biotin and EVs-Tim4 capturing systems, a wide range of NPs concentrations can be quantified. To further enhance the detection performance of the system, the following aspects should be addressed:

1. Improvement of detection performance

   Although the influence of physical parameters of VIF on detection performance has been demonstrated, the LOD remained at $10^7$ /mL. Microfluidic systems such as fluorescent probes and PCR, for instance, have demonstrated the ability to detect even lower concentrations of target NPs below $10^5$ /mL. Thus, LOD via our method should be further improved.

   First suggestion for improvement is adjusting the CPs concentration and size. In this study, pairs of CPs and NPs were used with concentrations of $8.2 \times 10^7$ /mL and $3.3 \times 10^7$ /mL in LOD condition. In this case, although the number of NPs adsorbed on a single CP was a few, CPs aggregates were formed larger than that in the blank condition (0 /mL NPs concentration). Here, reducing CPs concentration makes the number of NPs increase for adsorption on a single CP, potentially leading to the formation of CPs aggregates even at lower concentrations. On the other hand, if the CPs concentration is too low, the opportunity to collide decreases between particles, and aggregate does not occur. Alternatively, reducing CPs diameter to increase the surface

110

area/volume ratio may promote aggregate formation without reducing CPs concentration, contributing to further sensitivity and LOD improvement. Regarding the adjustment of CPs size, it is essential to simultaneously adjust pillar geometric conditions. As the CPs diameter decreases from 3 μm to approximately 1 μm, the size of the formed aggregates becomes smaller. In that situation, wider pillar spacings may hinder collisions between aggregates. The primary geometric design employed in this study is depicted in Fig. 6-1 (a, b). However, reducing the pillar diameter and separation, as illustrated in Fig. 6-1 (b, c) can induce even smaller local flows. This has the potential to promote aggregate formation, even with smaller CP sizes.
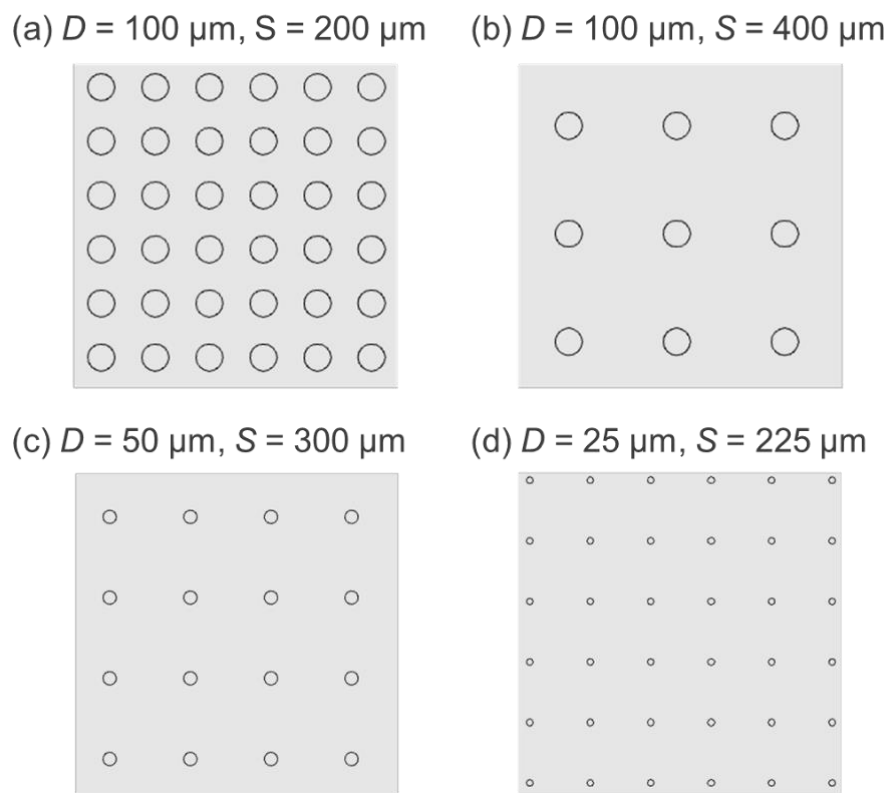


Fig. 6-1 Pillar geometric conditions: (a) $D = 100$ μm, $S = 200$ μm; (b) $D = 100$ μm, $S = 400$ μm; (c) $D = 50$ μm, $S = 300$ μm; and (d) $D = 25$ μm, $S = 225$ μm.

The second suggestion is to further investigate the parameters of vibration conditions, specifically by exploring higher frequencies. Acoustofluidics, typically driven in the range above kHz, has demonstrated that liquids can be rapidly mixed within a few seconds. In addition, particles whose size is nanometer-micrometer tend to concentrate at the center of μL droplets in this technique (Shilton et al. 2008; Gu et al. 2021; Peng et al. 2021; Wang et al. 2022). By integrating this technique with our concept of aggregate formation for NPs detection, CPs aggregates can be swiftly concentrated at the center of liquid droplets. Consequently, it is

expected that this concentration will lead to a LOD, enabling NP detection on a scale of seconds.
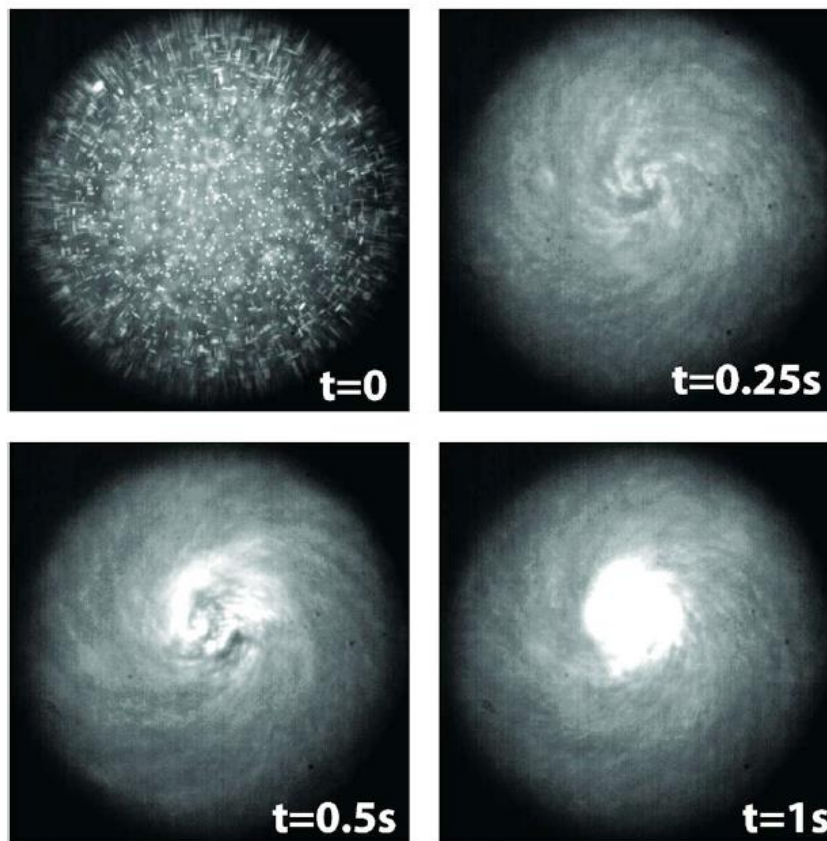


Fig. 6-2 Concentration of 0.5 μm polystyrene particles in 0.5 μL droplet driven by surface acoustic wave (Shilton et al. 2008).

Third suggestion for improvement is the suppression of nonspecific adsorption between CPs through intermolecular forces. Currently, small aggregates between CPs occur even under blank conditions, primarily due to hydrophobic interactions on CPs surfaces. Introducing surfactants to the sample is expected to suppress this adsorption and potentially improve LOD. However, the introduction of surfactants may affect the affinity-capturing system, and the optimal concentration needs careful consideration.

2. Detection of various biological substances

In this study, NPs detection was achieved through the aggregate formation based on interactions such as avidin-biotin and EV-Tim4 magnetic beads. By employing micrometer-sized particles, the detection of aggregation through microscopic observation was achieved, providing the advantage of not requiring relatively expensive equipment such as spectrophotometers. On the

other hand, a commonly employed method for the detection of biological substances such as proteins involves the latex agglutination test, which utilizes the aggregate formation of nanometer-sized latex particles. Although this technique is available as a commercial kit, spectrophotometers are still required. For this application, we anticipate that the versatile detection of biological substances through microscopic observation using microparticle aggregation can be achieved by applying microparticles coated with antibodies to adsorb target proteins, instead of using nanometer-sized latex particles.

3.  Application to practical and simple systems

    We demonstrated that the detection of NPs can be achieved using only a bright-field microscope, eliminating the need for high-sensitivity detection equipment. However, for industrial applications, challenges still exist in simplifying the system such as experimental setup to drive vibration. By employing commercially available compact motors that operate solely on DC power without the need for amplifiers, we can downsize the current bulk setup of the system. Additionally, incorporating a user-friendly, handheld imaging system, such as a smartphone, enables detection by individuals without access to a microscope. Through the integration of these components into our system, we anticipate achieving both simplification and cost reduction of the overall system.

# References

Amit R, Abadi A, Kosa G (2016) Characterization of steady streaming for a particle manipulation system. Biomed Microdevices 18:. https://doi.org/10.1007/s10544-016-0055-1

Andersson H, Van Der Wijngaart W, Enoksson P, Stemme G (2000) Micromachined flow-through filter-chamber for chemical reactions on beads. Sens Actuators B Chem 67:203–208. https://doi.org/10.1016/S0925-4005(00)00413-5

Andrews DG, Mcintyre ME (1978) An exact theory of nonlinear waves on a Lagrangian-mean flow. J Fluid Mech 89:609–646. https://doi.org/DOI: 10.1017/S0022112078002773

Baksh MM, Jaros M, Groves JT (2004) Detection of molecular interactions at membrane surfaces through colloid phase transitions. Nature 427:139–141. https://doi.org/10.1038/nature02209

Boriachek K, Islam MN, Möller A, et al (2018) Biological Functions and Current Advances in Isolation and Detection Strategies for Exosome Nanovesicles. Small 14:1–21. https://doi.org/10.1002/smll.201702153

Bu H, He D, He X, Wang K (2019) Exosomes: Isolation, Analysis, and Applications in Cancer Detection and Therapy. ChemBioChem 20:451–461. https://doi.org/10.1002/cbic.201800470

Castro D, Conchouso D, Kodzius R, et al (2018) High-throughput incubation and quantification of agglutination assays in a microfluidic system. Genes (Basel) 9:. https://doi.org/10.3390/genes9060281

Chen W, Li Z, Cheng W, et al (2021) Surface plasmon resonance biosensor for exosome detection based on reformative tyramine signal amplification activated by molecular aptamer beacon. J Nanobiotechnology 19:1–10. https://doi.org/10.1186/s12951-021-01210-x

Contreras-Naranjo JC, Wu HJ, Ugaz VM (2017) Microfluidics for exosome isolation and analysis: Enabling liquid biopsy for personalized medicine. Lab Chip 17:3558–3577. https://doi.org/10.1039/c7lc00592j

Fan S, Poetsch A (2023) Proteomic Research of Extracellular Vesicles in Clinical Biofluid. Proteomes 11:18. https://doi.org/10.3390/proteomes11020018

Fong T-T, Lipp EK (2005) Enteric Viruses of Humans and Animals in Aquatic Environments: Health Risks, Detection, and Potential Water Quality Assessment Tools. Microbiology and Molecular Biology Reviews 69:357–371. https://doi.org/10.1128/mmbr.69.2.357-371.2005

Fuchiwaki Y, Goya K, Tanaka M (2018) Practical high-performance lateral flow assay based on autonomous microfluidic replacement on a film. Analytical Sciences 34:57–63. https://doi.org/10.2116/analsci.34.57

Gu Y, Chen C, Mao Z, et al (2021) Acoustofluidic centrifuge for nanoparticle enrichment and separation

Gupta S, Kilpatrick PK, Melvin E, Velev OD (2012) On-chip latex agglutination immunoassay readout by electrochemical impedance spectroscopy. Lab Chip 12:4279–4286. https://doi.org/10.1039/c2lc40127d

Han J-H, Kim K-S, Yoon J-Y (2007a) The enhanced diffusional mixing for latex immunoagglutination assay in a microfluidic device. Anal Chim Acta 584:252–259. https://doi.org/https://doi.org/10.1016/j.aca.2006.11.044

Han J-H, Kim K-S, Yoon J-Y (2007b) The enhanced diffusional mixing for latex immunoagglutination assay in a microfluidic device. Anal Chim Acta 584:252–259. https://doi.org/https://doi.org/10.1016/j.aca.2006.11.044

Harper-Owen R, Dymock D, Booth V, et al (1999) Detection of unculturable bacteria in periodontal health and disease by PCR. J Clin Microbiol 37:1469–1473. https://doi.org/10.1128/jcm.37.5.1469-1473.1999

Hasegawa Y, Kasagi N (2011) Dissimilar control of momentum and heat transfer in a fully developed turbulent channel flow. J Fluid Mech 683:57–93. https://doi.org/10.1017/jfm.2011.248

Hayakawa T, Akita Y, Arai F (2018) Parallel trapping of single motile cells based on vibration-induced flow. Microfluid Nanofluidics 22:1–9. https://doi.org/10.1007/s10404-018-2062-4

Hayakawa T, Arai F (2017) On-chip micromanipulation method based on mode switching of vibration-induced asymmetric flow. In: Proceedings - IEEE International Conference on Robotics and Automation. Institute of Electrical and Electronics Engineers Inc., pp 6631–6636

Hayakawa T, Sakuma S, Arai F (2015) On-chip 3D rotation of oocyte based on a vibration-induced local whirling flow. Microsyst Nanoeng 1:1–9. https://doi.org/10.1038/micronano.2015.1

Hayakawa T, Sakuma S, Fukuhara T, et al (2014) A single cell extraction chip using vibration-induced whirling flow and a thermo-responsive gel pattern. Micromachines (Basel) 5:681–696. https://doi.org/10.3390/mi5030681

He M, Crow J, Roth M, et al (2014) Integrated immunoisolation and protein analysis of circulating exosomes using microfluidic technology. Lab Chip 14:3773–3780. https://doi.org/10.1039/c4lc00662c

Hoen ENMN t., van der Vlist EJ, Aalberts M, et al (2012) Quantitative and qualitative flow cytometric analysis of nanosized cell-derived membrane vesicles. Nanomedicine 8:712–720. https://doi.org/10.1016/j.nano.2011.09.006

House TA, Lieu VH, Schwartz DT (2014) A model for inertial particle trapping locations in hydrodynamic tweezers arrays. Journal of Micromechanics and Microengineering 24:. https://doi.org/10.1088/0960-1317/24/4/045019

Huang H, Fan C, Li M, et al (2020) COVID-19: A Call for Physical Scientists and Engineers. ACS Nano 14:3747–3754. https://doi.org/10.1021/acsnano.0c02618

Huang PH, Xie Y, Ahmed D, et al (2013) An acoustofluidic micromixer based on oscillating sidewall sharp-edges. Lab Chip 13:3847–3852. https://doi.org/10.1039/c3lc50568e

Huang X, Aguilar ZP, Xu H, et al (2015) Membrane-based lateral flow immunochromatographic strip with nanoparticles as reporters for detection: A review. Biosens Bioelectron 75:166–180. https://doi.org/10.1016/j.bios.2015.08.032

Ibsen S, Sonnenberg A, Schutt C, et al (2015) Recovery of Drug Delivery Nanoparticles from Human Plasma Using an Electrokinetic Platform Technology. Small 11:5088–5096. https://doi.org/10.1002/smll.201500892

Ibsen SD, Wright J, Lewis JM, et al (2017) Rapid Isolation and Detection of Exosomes and Associated Biomarkers from Plasma. ACS Nano 11:6641–6651. https://doi.org/10.1021/acsnano.7b00549

Justino C, Duarte A, Rocha-Santos T (2017) Recent Progress in Biosensors for Environmental Monitoring: A Review. Sensors 17:2918. https://doi.org/10.3390/s17122918

Kaneko K, Osawa T, Kametani Y, et al (2018) Numerical and experimental analyses of three-dimensional unsteady flow around a micro-pillar subjected to rotational vibration. Micromachines (Basel) 9:. https://doi.org/10.3390/mi9120668

Kastelowitz N, Yin H (2014) Exosomes and Microvesicles: Identification and Targeting By Particle Size and Lipid Chemical Probes. ChemBioChem 15:923–928. https://doi.org/10.1002/cbic.201400043

Kuramitz H (2009) Magnetic microbead-based electrochemical immunoassays. Anal Bioanal Chem 394:61–69. https://doi.org/10.1007/s00216-009-2650-y

Lien KY, Lee WC, Lei HY, Lee G Bin (2007) Integrated reverse transcription polymerase chain reaction systems for virus detection. Biosens Bioelectron 22:1739–1748. https://doi.org/10.1016/j.bios.2006.08.010

Lieu VH, House TA, Schwartz DT (2012) Hydrodynamic tweezers: impact of design geometry on flow and microparticle trapping. Anal Chem 84:1963–8. https://doi.org/10.1021/ac203002z

Lutz BR, Chen J, Schwartz DT (2005) Microscopic steady streaming eddies created around short cylinders in a channel: Flow visualization and Stokes layer scaling. Physics of Fluids 17:1–7. https://doi.org/10.1063/1.1824137

Lutz BR, Chen J, Schwartz DT (2006) Hydrodynamic tweezers: 1. Noncontact trapping of single cells using steady streaming microeddies. Anal Chem 78:5429–5435. https://doi.org/10.1021/ac060555y

Miyanishi M, Tada K, Koike M, et al (2007) Identification of Tim4 as a phosphatidylserine receptor. Nature 450:435–439. https://doi.org/10.1038/nature06307

Molina-Bolívar JA, Galisteo-González F (2005) Latex Immunoagglutination Assays. Journal of Macromolecular Science, Part C 45:59–98. https://doi.org/10.1081/MC-200045819

Nakai W, Yoshida T, Diez D, et al (2016) A novel affinity-based method for the isolation of highly purified extracellular vesicles. Sci Rep 6:1–11. https://doi.org/10.1038/srep33935

Nama N, Huang PH, Huang TJ, Costanzo F (2014) Investigation of acoustic streaming patterns around oscillating sharp edges. Lab Chip 14:2824–2836. https://doi.org/10.1039/c4lc00191e

Nama N, Huang PH, Huang TJ, Costanzo F (2016) Investigation of micromixing by acoustically oscillated sharp-edges. Biomicrofluidics 10:1–17. https://doi.org/10.1063/1.4946875

Nama N, Huang TJ, Costanzo F (2017) Acoustic streaming: An arbitrary Lagrangian-Eulerian perspective. J Fluid Mech 825:600–630. https://doi.org/10.1017/jfm.2017.338

Ng AHC, Uddayasankar U, Wheeler AR (2010) Immunoassays in microfluidic systems. Anal Bioanal Chem 397:991–1007. https://doi.org/10.1007/s00216-010-3678-8

Osher S, Sethian JA (1988) Fronts propagating with curvature-dependent speed: Algorithms based on Hamilton-Jacobi formulations. J Comput Phys 79:12–49

Pawan KC, Liu F, Zhe J, Zhang G (2018) Development and comparison of two immunodisaggregation based bioassays for cell secretome analysis. Theranostics 8:328–340. https://doi.org/10.7150/thno.21917

Peng T, Fan C, Zhou M, et al (2021) Rapid Enrichment of Submicron Particles within a Spinning Droplet Driven by a Unidirectional Acoustic Transducer. Anal Chem 93:13293–13301. https://doi.org/10.1021/acs.analchem.1c02914

Rallabandi B, Marin A, Rossi M, et al (2015) Three-dimensional streaming Flow in confined geometries. J Fluid Mech 777:408–429. https://doi.org/10.1017/jfm.2015.336

Rallabandi B, Wang C, Hilgenfeldt S (2017) Analysis of optimal mixing in open-flow mixers with time-modulated vortex arrays. Phys Rev Fluids 2:1–18. https://doi.org/10.1103/PhysRevFluids.2.064501

Salafi T, Zeming KK, Zhang Y (2017) Advancements in microfluidics for nanoparticle separation. Lab Chip 17:11–33. https://doi.org/10.1039/C6LC01045H

Sato K, Tokeshi M, Odake T, et al (2000) Integration of an immunosorbent assay system: Analysis of secretory human immunoglobulin A on polystyrene beads in a microchip. Anal Chem 72:1144–1147. https://doi.org/10.1021/ac991151r

Shao H, Chung J, Lee K, et al (2015a) Chip-based analysis of exosomal mRNA mediating drug resistance in glioblastoma. Nat Commun 6:1–9. https://doi.org/10.1038/ncomms7999

Shao H, Chung J, Lee K, et al (2015b) Chip-based analysis of exosomal mRNA mediating drug resistance in glioblastoma. Nat Commun 6:1–9. https://doi.org/10.1038/ncomms7999

Shen LM, Quan L, Liu J (2018) Tracking Exosomes in Vitro and in Vivo to Elucidate Their Physiological Functions: Implications for Diagnostic and Therapeutic Nanocarriers. ACS Appl Nano Mater 1:2438–2448. https://doi.org/10.1021/acsanm.8b00601

Shilton R, Tan MK, Yeo LY, Friend JR (2008) Particle concentration and mixing in microdrops driven by focused surface acoustic waves. J Appl Phys 104:. https://doi.org/10.1063/1.2951467

Suthar J, Parsons ES, Hoogenboom BW, et al (2020) Acoustic Immunosensing of Exosomes Using a Quartz Crystal Microbalance with Dissipation Monitoring. Anal Chem 92:4082–4093. https://doi.org/10.1021/acs.analchem.9b05736

Suthar J, Prieto-Simon B, Williams GR, Guldin S (2022) Dual-Mode and Label-Free Detection of Exosomes from Plasma Using an Electrochemical Quartz Crystal Microbalance with Dissipation Monitoring. Anal Chem 94:2465–2475. https://doi.org/10.1021/acs.analchem.1c04282

Suzuki H, Ho CM, Kasagi N (2004) A chaotic mixer for magnetic bead-based micro cell sorter. Journal of Microelectromechanical Systems 13:779–790. https://doi.org/10.1109/JMEMS.2004.835775

Suzuki T, Hasegawa Y (2017) Estimation of turbulent channel flow at based on the wall measurement using a simple sequential approach. J Fluid Mech 830:760–796. https://doi.org/10.1017/jfm.2017.580

Thomas NE, Coakley WT (1996) Measurement of antigen concentration by an ultrasound-enhanced latex immunoagglutination assay. Ultrasound Med Biol 22:1277–1284. https://doi.org/https://doi.org/10.1016/S0301-5629(96)00148-2

van der Vlist EJ, Nolte-'t Hoen ENM, Stoorvogel W, et al (2012) Fluorescent labeling of nano-sized vesicles released by cells and subsequent quantitative and qualitative analysis by high-resolution flow cytometry. Nat Protoc 7:1311–1326. https://doi.org/10.1038/nprot.2012.065

Volk A, Rossi M, Rallabandi B, et al (2020) Size-dependent particle migration and trapping in three-dimensional microbubble streaming flows. Phys Rev Fluids 5:114201. https://doi.org/10.1103/PhysRevFluids.5.114201

Wang CH, Lien KY, Wu JJ, Lee G Bin (2011) A magnetic bead-based assay for the rapid detection of methicillin- resistant Staphylococcus aureus by using a microfluidic system with integrated loop-mediated isothermal amplification. Lab Chip 11:1521–1531. https://doi.org/10.1039/c0lc00430h

Wang Z, Rich J, Hao N, et al (2022) Acoustofluidics for simultaneous nanoparticle-based drug loading and exosome encapsulation. Microsyst Nanoeng 8:. https://doi.org/10.1038/s41378-022-00374-2

Wiklund M, Radel S, Hawkes JJ (2013) Acoustofluidics 21: Ultrasound-enhanced immunoassays and particle sensors. Lab Chip 13:25–39. https://doi.org/10.1039/c2lc41073g

Wu H, Han Y, Yang X, et al (2015) A versatile microparticle-based immunoaggregation assay for macromolecular biomarker detection and quantification. PLoS One 10:1–10. https://doi.org/10.1371/journal.pone.0115046

Xu H, Liao C, Zuo P, et al (2018a) Magnetic-Based Microfluidic Device for On-Chip Isolation and Detection of Tumor-Derived Exosomes. Anal Chem 90:13451–13458. https://doi.org/10.1021/acs.analchem.8b03272

Xu H, Liao C, Zuo P, et al (2018b) Magnetic-Based Microfluidic Device for On-Chip Isolation and Detection of Tumor-Derived Exosomes. Anal Chem 90:13451–13458. https://doi.org/10.1021/acs.analchem.8b03272

Yoshioka Y, Kosaka N, Konishi Y, et al (2014) Ultra-sensitive liquid biopsy of circulating extracellular vesicles using ExoScreen. Nat Commun 5:3591. https://doi.org/10.1038/ncomms4591

Yu ST, Thi Bui C, Kim DTH, et al (2018) Clinical evaluation of rapid fluorescent diagnostic immunochromatographic test for influenza A virus (H1N1). Sci Rep 8:. https://doi.org/10.1038/s41598-018-31786-8

Zhang Y, Park S, Liu K, et al (2011) A surface topography assisted droplet manipulation platform for biomarker detection and pathogen identification. Lab Chip 11:398–406. https://doi.org/10.1039/c0lc00296h

Zhao Z, Yang Y, Zeng Y, He M (2016) A microfluidic ExoSearch chip for multiplexed exosome detection towards blood-based ovarian cancer diagnosis. Lab Chip 16:489–496. https://doi.org/10.1039/c5lc01117e

Zhou Y, Ma Z, Ai Y (2020a) Submicron Particle Concentration and Patterning with Ultralow Frequency Acoustic Vibration. Anal Chem 92:12795–12800. https://doi.org/10.1021/acs.analchem.0c02765

Zhou Y, Wang H, Ma Z, et al (2020b) Acoustic Vibration-Induced Actuation of Multiple Microrotors in Microfluidics. Adv Mater Technol 5:1–8. https://doi.org/10.1002/admt.202000323

Zhu H, Fohlerová Z, Pekárek J, et al (2020) Recent advances in lab-on-a-chip technologies for viral diagnosis. Biosens Bioelectron 153:112041

# Achievements

## Journals

1. <u>Kanji Kaneko</u>, Takeshi Hayakawa, Yosuke Hasegawa, and Hiroaki Suzuki, Numerical investigation of the induction of chaotic micromixing using the vibration switching, (submitted to *Journal of Applied Physics*).

2. <u>Kanji Kaneko</u>, Mamiko Tsugane, Taku Sato, Takeshi Hayakawa, Yosuke Hasegawa, Hiroaki Suzuki, Vibration Induced Flow Facilitating Affinity-Based Aggregation for Rapid Detection and Quantification of Nanoparticles", (under review at *Scientific Reports*).

3. Taku Sato*, <u>Kanji Kaneko</u>*, Takeshi Hayakawa, and Hiroaki Suzuki, Pneumatic Microballoons for Active Control of the Vibration-Induced Flow, *Micromachines*, 2023, 14(11), 2010;
   \* Authors equally contributed.

4. Joseph Rich, Brian Cole, Teng Li, Brandon Lu, Hanyu Fu, Brittany Smith, Jianping Xia, Shujie Yang, Ruoyu Zhong, James L. Doherty, <u>Kanji Kaneko</u>, Hiroaki Suzuki, Zhenhua Tian, Aaron D. Franklin, Tony Jun Huang, Aerosol jet printing of surface acoustic wave micro fluidic devices, accepted in *Microsystems & Nanoengineering*, 2023.

5. <u>Kanji KANEKO</u>, Zhitai HUANG, Taku SATO, Naoto UJIKAWA, Takeshi HAYAKAWA, Yosuke HASEGAWA, and Hiroaki SUZUKI, Investigation of the vibration-induced local flow around a micro-pillar under various vibrations, *Mechanical Engineering Journal (MEJ)*, Vol.10, No.1, Pages 22-00223, 2023

6. <u>Kanji Kaneko</u>, Takayuki Osawa, Yukinori Kametani, Takeshi Hayakawa, Yosuke Hasegawa*, and Hiroaki Suzuki*, Numerical and Experimental Analyses of Three- Dimensional Unsteady Flow around a Micro-Pillar Subjected to Rotational Vibration, *Micromachines*, 9(12), 668, 2018.
   \*corresponding authors.

## Full paper proceedings (international conference)

1. <u>Kanji Kaneko</u>, Mamiko Tsugane, Yosuke Hasegawa, Takeshi Hayakawa, and Hiroaki Suzuki, Experimental and Numerical Investigation of Particle Capture for Agglutination-Based NP detection Using the Vibration-Induced Flow, *Proc. MHS 2023 (34th Int. Symp. Micro-NanoMechatronics and Human Science)*, Nagoya, Japan (Nov. 2023).

2. Taku Sato, <u>Kanji Kaneko</u>, Takeshi Hayakawa, Hiroaki Suzuki, Active Control of Vibration-Induced Flow Using a Pneumatically Driven Microballoon device, *Proc. Transducers 2023*, Kyoto, (June, 2023).

3. <u>Kanji Kaneko</u>, Mamiko Tsugane, Taku Sato, Takeshi Hayakawa, Yosuke Hasegawa, Hiroaki Suzuki, Detection of nanoparticles in a minute sample using the vibration induced flow, *Proc. NEMS 2022*, online, (April, 2022).

4. <u>Kanji Kaneko</u>, Taiji Okano, Takeshi Hayakawa, Yosuke Hasegawa, Hiroaki Suzuki, A Pumpless Mixer for Efficient Capturing of Small Particles Utilizing Vibration-Induced Flow, *Proc. MEMS 2019*, pp. 406-408, Seoul, Korea (2019.1).

**Abstract paper proceedings (international conference)**

1. <u>K. Kaneko</u>, M. Tsugane, T. Sato, Y. Hasegawa, T. Hayakawa, H. Suzuki, "Detection and Quantification of Nanoparticles Using the Vibration-Induced Flow," Proc. *MHS 2022 (33rd Int. Symp. Micro-NanoMechatronics and Human Science)*, Nagoya, Japan (Nov. 2022).

2. <u>K. Kaneko</u>, Y. Hasegawa, T. Hayakawa, Hiroaki Suzuki, "Numerical study of the vibration-induced chaotic mixer based on vibration switching," *Proc. µTAS 2022*, Hangzhou, China, online (2022.10).

3. Z. Huang, <u>K. Kaneko</u>, Y. Asada, Y. Hasegawa, T. Hayakawa, H. Suzuki, "Numerical characterization of the vibration-induced flow in various conditions," *Proc. µTAS 2022*, Hangzhou, China, online (2022.10).

4. T. Sato, <u>K. Kaneko</u>, T. Hayakawa, H. Suzuki, "Active control of the vibration-induced flow by pneumatically actuated micropillars," *Proc. µTAS 2022*, Hangzhou, China, online (2022.10).

5. <u>K. Kaneko</u>, T. Hayakawa, Y. Hasegawa, H. Suzuki, "Numerical simulation of vibration-induced mixer using a cylindrical pillar with various vibration directions," *Proc. APCOT 2022*, online, (April, 2022).

6. T. Sato, H. Zhitai, N. Ujikawa, <u>K. Kaneko</u>, Y. Hasegawa, T. Hayakawa, H. Suzuki, "Numerical and Experimental Analysis of the Vibration-Induced Flow around Complex Pillar Shapes," *Proc. µTAS 2021*, Palm Springs, CA, USA, online (2021.10).

7. <u>K. Kaneko</u>, M. Tsugane, T. Sato, T. Hayakawa, Y. Hasegawa, H. Suzuki, "Evaluation of the Capturing Efficiency of Exosome in a Micromixer Driven by the Vibration-Induced Flow," *Proc. µTAS 2021*, Palm Springs, CA, USA, online (2021.10).

8. <u>K. Kaneko</u>, N. Ujikawa, Y. Hasegawa, T. Hayakawa, H. Suzuki, "A Numerical Simulation of Pumpless-Chaotic Micromixer Utilizing the Vibration-Induced Flow," *Proc. Acoustofluidics 2021*, online (2021.8).

9. <u>K. Kaneko</u>, T. Osawa, Y. Kametani, Y. Hasegawa, H. Suzuki, "A Numerical Model for Three-Dimensional Analysis of Vibration-Induced Flow," *Proc. µTAS 2018*, pp. 465-467, Kaohsiung, Taiwan (2018.11).

10. K. Kaneko, T. Osawa, Y. Kametani, Y. Hasegawa, H. Suzuki, "Design of pumpless chaotic mixing device driven by the vibration-induced flow," *Proc. μTAS 2017*, pp. 255-256, Savannah, GA, USA (2017.10).

## Presentation at international conferences

1. K. Kaneko, Y. Hasegawa, T. Hayakawa, H. Suzuki, "The Vibration-Induced Chaotic Mixing with Switching of Vibrations Axes," *The 27th International Conference on Miniaturized Systems for Chemistry and Life Sciences (μTAS 2023)*, Katowice, Poland (Oct. 2023).

2. K. Kaneko, M. Tsugane, Y. Hasegawa, T. Hayakawa, H. Suzuki, "Hydrodynamic Enhancement of Agglutination-based Nanoparticle Detection Driven by the Vibration-induced Flow," *The 27th International Conference on Miniaturized Systems for Chemistry and Life Sciences (μTAS 2023)*, Katowice, Poland (Oct. 2023).

3. Z. Huang, K. Kaneko, R. Yoneyama, T. Hayakawa, M. Takinoue, H. Suzuki, "Preparation of Monodisperse DNA Gels Using Vibration-Induced Flow," *The 27th International Conference on Miniaturized Systems for Chemistry and Life Sciences (μTAS 2023)*, Katowice, Poland (Oct. 2023).

4. K. Kaneko, N. Ujikawa, Y. Hasegawa, T. Hayakawa, H. Suzuki, "Numerical simulation of microfluidics-based nanoparticle capture utilizing the vibration-induced flow," *Pacifichem 2021* (online), (2021.12).

5. T. Sato, K. Kaneko, T. Okano, Y. Hasegawa, T. Hayakawa, H. Suzuki, "Evaluation of the capturing efficiency nanoparticles in the vibration-induced micromixer," *Pacifichem 2021* (online), (2021.12).

## Presentation in domestic conferences

1. 金子，津金，長谷川，早川，鈴木，「振動誘起流れによるナノ粒子検出に向けた粒子捕捉の実験的および数値的研究」，第 14 回マイクロ・ナノ工学シンポジウム，熊本，2023 年 11 月．

2. 黄，金子，米山，早川，瀧ノ上，鈴木，「振動誘起流れを用いた単分散 DNA ゲルのサイズ制御法」，第 14 回マイクロ・ナノ工学シンポジウム，熊本，2023 年 11 月．

3. 髙田，金子，縄田，佐藤，津金，R. Zhong, T. J. Huang，鈴木，「表面弾性波による膜小胞破壊の検討」，化学とマイクロ・ナノシステム学会第 48 回研究会，熊本，2023 年 11 月．

4. 服部，金子，早川，鈴木，「振動誘起流れを用いたラテックス凝集によるタンパク質検出感度の評価」，化学とマイクロ・ナノシステム学会第 48 回研究会，熊本，2023 年 11 月．

5. 金子，津金，長谷川，早川，鈴木，「振動誘起流れによるナノ粒子検出系の流体力学的評価」，化学とマイクロ・ナノシステム学会第 47 回研究会，東北大学，2023 年 5 月．

6. 浅田，金子，佐藤（拓），黄，永倉，早川，長谷川，鈴木，「振動が誘起する流れ場の 3 次元挙動の数値シミュレーション」，化学とマイクロ・ナノシステム学会　第 46 回研究会，徳島，2022 年 11 月．

7. 永倉，金子，佐藤（拓），佐藤（玲），早川，鈴木，「振動誘起流れを用いた振動方向切換えによる流体混合の効率化と評価」，化学とマイクロ・ナノシステム学会　第 46 回研究会，徳島，2022 年 11 月．

8. 金子，津金，長谷川，早川，鈴木，〇佐藤（拓）「効率的なナノ粒子検出に向けた振動誘起マイクロ混合デバイスの開発」，日本機械学会 2022 年度年次大会，富山，2022 年 9 月．（口頭発表）

9. 佐藤，金子，早川，鈴木，「振動誘起流れの制御のための空圧駆動マイクロピラーの開発」，化学とマイクロ・ナノシステム学会第 45 回研究会，中央大学 後楽園キャンパス＆オンライン（ハイブリッド），2022 年 5 月．

10. Z. Huang, K. Kaneko, Y. Hasegawa, T. Hayakawa, H. Suzuki, "NUMERICAL AND EXPERIMENTAL ANALYSIS OF THE VIBRATION-INDUCED FLOW AROUND COMPLEX PILLAR SHAPES WITH VARIOUS VIBRATIONS"，化学とマイクロ・ナノシステム学会第 45 回研究会, 中央大学 後楽園キャンパス＆オンライン（ハイブリッド），2022 年 5 月．

11. 金子，津金，長谷川，早川，鈴木，「振動誘起流れを用いた微量サンプル内ナノ粒子の検出および定量」，化学とマイクロ・ナノシステム学会第 45 回研究会，中央大学 後楽園キャンパス＆オンライン（ハイブリッド），2022 年 5 月．（優秀発表賞受賞！）

12. 佐藤（拓），金子，早川，鈴木，「空圧駆動式マイクロピラーによる振動誘起流れの生起制御」，化学とマイクロ・ナノシステム学会第 44 回研究会，オンライン，2021 年 11 月．

13. H. Zhitai1, T. Sato, K. Kaneko, Y. Hasegawa, T. Hayakawa, H. Suzuki, "Numerical and Experimental Analysis of the Vibration-Induced Flow," 化学とマイクロ・ナノシステム学会第 44 回研究会，オンライン，2021 年 11 月．

14. 金子，津金，早川，長谷川，鈴木，「細胞外小胞の効率的回収に向けた振動誘起流れを用いたポンプレスミキサの開発」，日本機械学会第 12 回マイクロ・ナノ工学シンポジウム予稿集，オンライン，2021 年 11 月．

15. 金子，津金，佐藤，早川，長谷川，鈴木，「細胞外小胞の効率的補足に向けた振動誘起流れによる混合システムの開発」，細胞を創る研究会 14.0，オンライン，2021 年 11 月．

16. 金子，氏川，長谷川，早川，鈴木，「振動誘起流れによるナノ粒子回収系に向けた数値解析ツールの開発」，化学とマイクロ・ナノシステム学会第 43 回研究会，オンライン，2021 年 5 月．

**Patent pending**

1. 鈴木宏明，金子完治，早川健，ナノ粒子検出方法，特願 2022-144134，出願，2022/9.

**Grants**

1. 「日本学術振興会 2023 年度特別研究員-DC2」
   研究課題名：振動が誘起するカオス混合を用いた高効率ナノ粒子検出デバイス
   獲得金額：200 万円
   期間：2023/04/25 – 2025/03/31
   研究代表者：金子完治
2. 「日本学術振興会 令和 4 年度(2022 年度)採用分(第 2 回)若手研究者海外挑戦プログラム」
   （補欠繰り上げ採用，都合により採用辞退）
   研究課題名：振動が誘起するカオス混合を用いた効率的なナノ粒子検出

**Awards**

1. 瀧野秀雄学術奨励賞
   「優れた研究業績と特許の内容が認められた.」(2023 年 3 月)
2. 受賞（国内学会）
   優秀発表賞「振動誘起流れを用いた微量サンプル内ナノ粒子の検出および定量」，〇金子 完治，化学とマイクロ・ナノシステム学会 第 45 回研究会（2022 年 5 月）
3. 受賞（国際学会）
   CM HO Best Paper Award in Micro/Nano Fluidics, "Detection of nanoparticles in a minute sample using a vibration induced flow", 〇Kanji Kaneko, Mamiko Tsugane, Taku Sato, Takeshi Hayakawa, Yosuke Hasegawa and Hiroaki Suzuki, The 17th International Conference on Nano/Micro Engineered and Molecular Systems (NEMS) 2022, （2022 年 4 月）
4. 受賞（国内学会）
   優秀講演論文賞「空圧駆動マイクロピラーデバイスによる振動誘起流れの生起制御」，〇佐藤 拓，金子 完治，早川 健，鈴木 宏明 日本機械学会第 13 回マイクロ・ナノ工学シンポジウム（2022 年 12 月）

**Other publications**

1. 化学とマイクロ・ナノシステム学会誌，"振動誘起流れを用いた微量サンプル内ナノ粒子の検出および定量"，〇金子完治，津金麻実子，長谷川洋介，早川健，鈴木宏明，Vol. 21, No. 2 (2022)，2022 年 10 月

2. 化学とマイクロ・ナノシステム学会誌，"化学とマイクロ・ナノシステム学会 第 44 回研究会 若手企画開催報告"，〇伊野浩介，梨本裕司，鈴木雅登，平本薫，<u>金子完治</u>，波多美咲，Vol. 21, No. 1 (2022)，2022 年 3 月

# Acknowledgments

# About the author



**Kanji Kaneko** received his B.S. degree in the Department of Precision Mechanics from Chuo University, Japan in 2017, and his M.S. degree in Precision Mechanics from Chuo University in 2019 supervised by Prof. Hiroaki Suzuki. From 2019-2021 he worked at Nissan Motor Corporation. From 2021, he is enrolled in the Ph.D. program and JSPS Research Fellow DC2 in Precision Mechanics at the Graduate School of Science and Engineering, Chuo University, Japan, under the supervision of Prof. H. Suzuki. During his Ph.D. program, he worked as a visiting scholar at Duke University for four months under the supervision of Prof. Tony Jun Huang.